**AEDC-TR-80-33**

c 4

# A Comparison of Particle Diagnostic Systems

Jay D. Hunt
ARO, Inc.

August 1981

Final Report for Period October 1977 — September 1979

**ARNOLD ENGINEERING DEVELOPMENT CENTER**
**ARNOLD AIR FORCE STATION, TENNESSEE**
**AIR FORCE SYSTEMS COMMAND**
**UNITED STATES AIR FORCE**

This report has been reviewed by the Office of Public Affairs (PA) and is releasable to the National Technical Information Service (NTIS). At NTIS, it will be available to the general public, including foreign nations.

**APPROVAL STATEMENT**

This report has been reviewed and approved.

MARSHALL K. KINGERY
Directorate of Technology
Deputy for Operations

Approved for publication:

FOR THE COMMANDER

MARION L. LASTER
Director of Technology
Deputy for Operations

| REPORT DOCUMENTATION PAGE | | READ INSTRUCTIONS BEFORE COMPLETING FORM |
|---|---|---|
| 1 REPORT NUMBER<br><br>AEDC-TR-80-33 | 2 GOVT ACCESSION NO. | 3. RECIPIENT'S CATALOG NUMBER |
| 4 TITLE (and Subtitle)<br><br>A COMPARISON OF PARTICLE DIAGNOSTIC SYSTEMS | | 5 TYPE OF REPORT & PERIOD COVERED<br>Final Report—October 1977 to September 1979 |
| | | 6. PERFORMING ORG. REPORT NUMBER |
| 7. AUTHOR(s)<br><br>Jay D. Hunt, ARO, Inc., a Sverdrup Corporation Company | | 8. CONTRACT OR GRANT NUMBER(s) |
| 9 PERFORMING ORGANIZATION NAME AND ADDRESS<br>Arnold Engineering Development Center/DOT<br>Air Force Systems Command<br>Arnold Air Force Station, Tennessee 37389 | | 10 PROGRAM ELEMENT, PROJECT, TASK AREA & WORK UNIT NUMBERS<br><br>Program Element 65807F |
| 11. CONTROLLING OFFICE NAME AND ADDRESS<br>Arnold Engineering Development Center/DOS | | 12. REPORT DATE<br>August 1981 |
| Air Force Systems Command<br>Arnold Air Force Station, Tennessee 37389 | | 13. NUMBER OF PAGES<br>84 |
| 14 MONITORING AGENCY NAME & ADDRESS(if different from Controlling Office) | | 15. SECURITY CLASS. (of this report)<br><br>UNCLASSIFIED |
| | | 15a DECLASSIFICATION/DOWNGRADING SCHEDULE<br>N/A |

16 DISTRIBUTION STATEMENT (of this Report)

Approved for public release; distribution unlimited.

17. DISTRIBUTION STATEMENT (of the abstract entered in Block 20, if different from Report)

18 SUPPLEMENTARY NOTES

Available in Defense Technical Information Center (DTIC)

19 KEY WORDS (Continue on reverse side if necessary and identify by block number)

| particle size | interferometers | clouds |
| measuring instruments | backscattering | calibration |
| fiber optics | flow field | holography |
| probes | ice | cameras |

20. ABSTRACT (Continue on reverse side if necessary and identify by block number)

An experimental investigation was conducted to examine the particle sizing characteristics of four particle diagnostic systems (PDS): a fiber-optics array probe (FOS), two separate particle-sizing interferometers (PSI), and a backscattering particle-sizing system (BPS). Simulated icing clouds, produced in an icing research test cell, were used as the particle flow field for the investigation. An in-line holocamera was selected

DD $_{1\ JAN\ 73}^{FORM}$ 1473    EDITION OF 1 NOV 65 IS OBSOLETE

20.   ABSTRACT (Continued)

as the baseline device and was, therefore, used to calibrate each
icing cloud.   Each PDS was used to obtain particle size information
for each simulated icing cloud.   Typical examples of the results
obtained with each PDS are presented as well as typical calibration
results.   The results obtained with each PDS are also compared to
the calibration results.   The comparisons show that the FOS is the
only device tested that yields results comparable to the holocamera
results.   The particle number density of a simulated icing cloud
is shown to be too large for obtaining accurate particle size data
with an on-axis forward-scattering PSI.   The data obtained with the
BPS exhibit a monodisperse distribution and are inconsistent with
the holographically obtained calibration data.

AFSC
Arnold AFS Tenn

## PREFACE

**CONTENTS**

3

# 1.0 INTRODUCTION

## 1.1 GENERAL

The formation of ice on aircraft surfaces occurs during flight through clouds of supercooled water droplets. Ice accretion on these surfaces usually results in a degradation of both aircraft performance and operational safety. Therefore, protective devices for removing accumulated ice (deicing devices) or for continuously maintaining the exposed surfaces of the aircraft free of ice (antiicing devices) are routinely used. For safety reasons, the effectiveness of the protective devices must be determined before their use; hence, each device must be tested under simulated atmospheric icing conditions.

Icing conditions are simulated by duplicating the principal factors that characterize an icing cloud: (1) air temperature, (2) droplet size distribution (including the "mean effective" droplet diameter for the droplet size distribution), and (3) cloud liquid water content (LWC). The natural icing conditions simulated during testing are well known and documented in the "Airworthiness Standards" (Ref. 1). Figure 1 summarizes the meteorological conditions used for icing tests.

During icing cloud simulation, the air temperature is measured and controlled by conventional methods (Ref. 2). However, measurement and control of the cloud droplet size distribution and LWC require specialized instrumentation systems and test techniques. To produce true icing simulation requires careful consideration of the test techniques and of certain fundamental limitations of the droplet sizing instrumentation systems.

## 1.2 BACKGROUND

The engine test cells at the Arnold Engineering Development Center (AEDC) Engine Test Facility (ETF) have been developed to provide water droplet fields that simulate cloud condensate for engine icing tests. These facilities were developed to determine the operational effectiveness of both turbojet engines and their icing protection systems under conditions that closely simulate or duplicate natural icing conditions.

Icing clouds are produced at the AEDC/ETF by injecting a continuous spray of water droplets into a cold airstream directed at the engine. Figure 2 shows that the water spray is injected by a bank of pneumatic spray nozzles located in the low-velocity region of the test cell upstream of the test cell bellmouth. The LWC and the droplet size distribution (from which the mean effective droplet diameter can be obtained) are maintained through variations in the water and air supply pressures of the pneumatic spray nozzles.

5

The icing cloud LWC and mean effective droplet diameter are specified before testing as part of the test matrix; normally, more than one icing cloud are simulated during a given test. Consequently, the spray nozzles are calibrated before testing to yield LWC and mean effective droplet size as functions of the inlet conditions to the spray nozzles. Although the spray nozzle calibration is used during testing to establish the correct icing conditions, it is desirable to determine continuously the accuracy of the cloud simulation. Therefore, the LWC and droplet size distribution are monitored throughout the actual icing tests.

To characterize the LWC and mean effective droplet size, the AEDC/ETF uses the total injected water flow rate and holograms of the droplet cloud taken at the engine inlet. The LWC is determined from the measurement of total injected water flow rate by an icing simulation computer program described in Ref. 3. The mean effective droplet size is determined from the reconstructed holograms.

It should be noted that use of the holocamera to determine droplet size distributions does not provide the desired online continuous review of droplet information because the holographic data are reduced off line. However, it is reported that several particle diagnostic systems have been developed that can size particles continuously and in nearly real time (Refs. 4 through 12).

It was decided that because of the need to monitor and set droplet size during icing simulation, in-depth evaluation of particle-sizing techniques and systems was required.

## 1.3 SCOPE OF INVESTIGATION

A research program was conducted at the AEDC/ETF to refine the measurement techniques used to characterize the injected water droplets of a simulated icing cloud. The objectives of the study were (1) to develop improved measuring techniques for defining water droplet number, size, and velocity and, (2) if possible, to use these measurement techniques to obtain a data base for an improved icing simulation computer program (Ref. 3).

To achieve the program objectives required (1) surveying available particle diagnostic systems and selecting the systems meeting the measurement requirements defined in Section 2.2, (2) experimentally evaluating these systems to determine their applicability as particle diagnostic tools for icing simulation, and (3) developing a research test cell to provide the required icing environments for the experiments. The selected particle diagnostic systems are described, and the droplet size data obtained during the experimental program are presented. The research test cell is also described and its operating characteristics summarized.

## 2.0 EXPERIMENTAL APPARATUS AND PROCEDURES

### 2.1 ICING RESEARCH TEST CELL

A research test cell has been developed for the sole purpose of studying icing environments. The research cell – a subscale version of the AEDC propulsion development test cells – can provide the meteorological icing condition described by Fig. 1 for airflows up to 30 lbm/sec. Table 1 summarizes the research test cell characteristics pertinent to the icing experiments.

The icing research test cell (Figs. 3a and b) consists of a flowmetering venturi, plenum chamber, water spray system, bellmouth, removable inlet connecting ducts, and a test chamber. A secondary air supply system also provides air to the test chamber; this secondary air encapsulates the primary air to prevent recirculation of the icing cloud water droplets through the measurement plane (Fig. 3a).

The plenum chamber rides on casters along rails. It can be moved in the axial direction; hence, the axial distance between the spray nozzle (located in the plenum chamber) and the test section can be varied without moving the test chamber. This makes it possible to study water droplet formation as a function of axial position without relocating the particle diagnostics instrumentation.

The water spray system, which provides filtered, demineralized water and atomizing air to the spray nozzle, is shown in Fig. 3c. A single Spraying System 26B spray nozzle (Fig. 3d) provides the droplet cloud. The spray nozzle is located on the centerline of the plenum chamber and is attached to a movable screw assembly. The axial position of the spray nozzle can be varied from 12 to 18 in. upstream of the bellmouth.

The test chamber (Figs. 3a and b) has six instrumentation and/or viewing ports around its circumference. The icing cloud, which issues from the connecting duct into the test chamber as a free jet, can be viewed through all of the ports. The test plane – the plane along which all droplet size measurements are made – coincides with the centerline of the ports.

### 2.2 ICING INSTRUMENTATION

For a particle diagnostics system (PDS) to meet the testing needs of the AEDC/ETF, it must be capable of determining particle diameters and number densities* in the range

---

*For a given LWC in Fig. 1, the droplet number density is determined by assuming a monodisperse distribution and utilizing Eq. (C-2) of Appendix C.

summarized in Fig. 1. Further, the PDS should provide real- or nearly real-time data acquisition and should not disturb the flow field. Hence, the PDS must provide the means to measure droplet diameters in the range from 5 to 100 $\mu$m at concentrations up to $10^3$ particles per cubic centimeter and provide continuous, online, in situ data acquisition. This set of criteria was used to evaluate prospective PDS's during the instrumentation survey portion of the research program.

Several of the PDS's surveyed (including oil slides, rotating multicylinders, cascade impactors, Coulter counters, and commercial optical counters) require samples to be removed from the flow field. Direct sampling techniques in which the particles are impacted or otherwise mechanically collected do not, however, meet the ETF criteria since, for the most part, direct-sampling techniques disturb the flow field and produce discontinuity in sampling. Consequently, the majority of the PDS's surveyed were electro-optical techniques in which direct sampling is not required.

Of the numerous electro-optical PDS's surveyed, four were selected to be evaluated further in the icing research test cell. These include a fiber-optics sizing system (FOS), two separate particle-sizing interfermometers (PSI), and a backscattering particle-sizing system (BPS). An inline holocamera was selected as the baseline device for the experimental part of the evaluation.

## 2.2.1 Holography System

The advantages of using a holocamera as a particle diagnostic tool are: (1) It provides three-dimensional viewing capability of the particle field. (2) Particle size and number density are obtained directly. (3) When double pulsed, the holocamera allows obtaining particle velocity information for velocities up to 5,900 fps (Refs. 4 through 6). Disadvantages of the holocamera system are: (1) High particle number density can limit resolution. (2) Data acquisition is neither continuous nor online. (3) The data reduction is laborious, time consuming, and subjective.

The highest particle number density required in the icing research cell is estimated to be less than $10^3$ cm$^{-3}$. Extensive applications of holography at AEDC (Refs. 4 through 7) have shown that good quality holograms, as defined by Royer and described by Belz and Menzel in Ref. 7, have been obtained for greater particle concentrations. It was deduced, therefore, that the particle number density required in the research cell would not be large enough to severely limit the resolution of the holocamera. Also, the time required to reduce the holographic data is not critical and does not severely limit the holocamera's application as a research tool; the measurements obtained in the icing research test cell will be used to

8

calibrate the particle flow field "as is," rather than to set the flow field to preselected conditions. For these reasons it was advantageous to use a holocamera as the baseline instrument for AEDC icing research.

Figure 4 is a schematic of the inline holocamera used in the icing research test cell. The camera consists of a double-pulsed Apollo ruby laser, a specially designed collimator/autocollimator optical system, a lens and filter system, and a multiple glass plate magazine (Fig. 5). In addition to the pulsed laser, a 5-mw He-Ne laser was used to align the holography system before testing. The holograms were recorded on Agfa-Gevaert 10E75 high-quality glass-backed photographic plates to minimize image distortion caused by film warpage.

The holocamera optical system is aligned to image the centerline of the icing research test cell onto the film plane of the hologram. The sample volume of the holocamera is 2 in. in diameter by 12 in. in length. Thus, the holograms contain particle size information from a 6-in. range on either side of the film plane. The holocamera system has a theoretical resolution of 7.5 $\mu$m.

Holograms are reconstructed with the system shown in Fig. 6. The collimated beam from a 15-mw He-Ne laser provides the illumination for reconstruction. The hologram is mounted on a three-axis traverse system that allows the operator to move the hologram relative to a fixed, closed-circuit television vidicon. An auxiliary lens projects an enlargement of the reconstructed image in the vidicon tube. Once an image is identified and focused on the TV monitor, the operator indicates the position of the image with a light pen, and a Millipore® model πMc image-analysis system is used to measure either the perimeter, diameter, or area of the image. The size measurement and the three-dimensional position are recorded on punched paper tape for subsequent analysis. Reference 7 presents a complete description of the holographic system, including optical alignment of the holocamera.

## 2.2.2 Fiber-Optics Particle-Sizing System (FOS)

The FOS is an imaging device that uses an expanded laser beam as a light source and an optical system to define a probe volume in the particle flow field (Fig. 7). The probe volume is focused onto a linear array of sensor modules. As a particle passes through the probe volume, its shadow occludes a number of the sensors. The number of sensor modules occluded is proportional to the particle diameter. Reference 8 gives a thorough discussion of the theory and application of the FOS.

The FOS, as used in the icing research test cell, is shown schematically in Fig. 8. The illumination for the probe volume, located on the test cell centerline, is provided by an air-

cooled 25-mw argon laser. The laser beam is spatially filtered and focused by a Spectra-Physics collimator and directed by a front surface mirror through a test cell window.

The light-collecting optics of the FOS, in conjunction with a cross-beam coincidence system, defines the optical probe volume. Both the collecting optics and the coincidence system are located outside the test cell opposite the argon laser (Fig. 8). The light-collecting optics are aligned along the laser axis, and the cross-beam coincidence system is inclined to the laser axis by 12.83 deg. The probe volume is magnified 83 times and projected by the collecting optics onto an array of 32 fiber optics, or "light pipes." The coincidence system is used to define the probe volume and eliminate the spurious effects of noise coupled with out-of-focus particle transits. The individual fiber optics, which are 264 $\mu$m in diameter, are arrayed along a straight line for a total length of 0.3325 in.; each fiber terminates at a photomultiplier (PM) tube. Each of the 32 photodetector circuits provides information to the size-determination logic of the data handling system, as described in Ref. 9. The number of events of specified size is stored and displayed periodically on both a cathode ray tube (CRT) and a digital display on the front panel of the particle data system (Fig. 9). A Berkely® EPUT meter is slaved to the memory-enable-switch of the data acquisition system so that the time over which the measurements are made can be accurately recorded.

Thirty channels of particle size data are stored by the data handling system. Data output is controlled manually. The channel number and the particle counts corresponding to that channel comprise the output data; each is printed out sequentially by a Hewlett Packard 5055A digital recorder.

A complete description of the FOS as used in the icing research test cell is given in Ref. 9.

### 2.2.3 Particle-Sizing Interferometer (PSI)

The principle of operation of the PSI is illustrated in Fig. 10. Two laser beams of equal intensity and linearly polarized in the same direction are focused and crossed to form a small ellipsoidal probe volume in space. Because of the interaction of the two beams, the probe volume is filled with parallel, equally spaced fringes. As a particle passes through the probe volume, light is scattered which produces, by means of a photomultiplier tube, a current signature characteristic. As shown in Fig. 10, the current waveform is composed of a high-frequency A-C component and a Gaussian-shaped "pedestal" component. The ratio of A-C amplitude divided by the pedestal amplitude is defined as the visibility of the waveform and, as shown in Ref. 10, the particle size is a unique factor (within limits) of the visibility.

Hence, by utilizing the signature characteristics, the size of each particle that passes through the probe volume can be determined. More detailed descriptions of interferometric particle sizing are given in Refs. 10 and 11.

The major subsystems of a PSI may be categorized as (1) a laser (which provides a coherent, highly collimated light source), (2) transmitting optics (which precondition and focus the laser light to form the probe volume), (3) receiving optics (which collect and focus the light scattered by particles moving through the probe volume), and (4) signal conditioning electronics (which amplify the scattered radiation and process the signal to obtain visibility). The specification and arrangement of these subsystems' components are dictated by the intended application of the PSI.

Two PSI systems were selected for evaluation in the icing research test cell. One system is a PSI developed at AEDC and the other is a commercially available system. Although the operating principle is the same for both systems, the differences existing between them are great enough that experimental evaluation of each was required. A description of each PSI as tested in the icing research test cell is given below.

### 2.2.3.1 AEDC-Developed PSI

The optical system is shown schematically in Fig. 11 (Fig. 11 and much of the following descriptions were taken from Ref. 12). The light source is a 15-Mw helium-neon laser operating in the TEMoo mode at a wavelength of 0.6328 $\mu$m. The transmitting optics consist of a Bragg cell beamsplitter driven at 15 MHz and a system of lenses which brings the two beams to simultaneous cross focus; the crosspoint is found 39.4 in. in front of the final transmitting lens. Use of a Bragg cell as a beamsplitter produces a set of moving fringes in the probe volume, and the Bragg cell is driven in a manner to move the fringes in the direction opposite the direction of the droplet flow. A fringe spacing of 19 $\mu$m was used; however, other fringe spaces can be selected by changing the transmitting lenses. The beamwaist diameter is 150 $\mu$m. A set of 5.9-in.-diam, f/5 lenses is used to collect and focus the scattered light. A special mask that admits light through two 60-deg wedge-shaped openings is used on the collection lens (see Fig. 11). A 200-$\mu$m pinhole in front of the PM tube blocks light originating at points other than the probe volume. The current waveforms are produced with an RCA® 8644 PM tube.

The electronics used to measure the visibility are shown as a block diagram in Fig. 12. The photodetector signal is amplified and sent simultaneously to a bandpass filter and to a low-pass filter for separation of the A-C component from the pedestal. Then, the pedestal and A-C magnitude are peak detected. The peak pedestal signal is fed to the denominator input of analog divider while the peak of the A-C signal fed to the divider is numerator input of the divider. (The output signal from the divider is ratio of peak A-C magnitude to peak pedestal.)

The data handling system consists of a microcomputer that stores the data in histogram form and a Tektronix Model 4051 table-top computer that controls data acquisition. It has

11

been noted (Ref. 12) that the particle size data from the PSI should be corrected to compensate for the size of the sample volume, which varies with particle size, and also to account for variations of the bin width of the histograms, which vary with visibility. Consequently, the 4051 is also used to correct the raw data from these variations so that the bar heights of the histograms are output as number of particles per cubic centimeter per micrometer. The output data are comprised of histogram bar heights as a function of particle diameter, with a maximum resolution of 32 bins per histogram.

## 2.2.3.2 Commercial-PSI

The commercially available PSI was built to AEDC specifications by Spectron Development Laboratories, Inc. The optical system is shown in Fig. 13. The light source is a 15-mw He-Ne laser operating in the TEMoo mode at a wavelength of 0.6328 $\mu$m. The transmitting optics consist of a glass block beamsplitter and a lens system that cross and focus the beams at the same location. The crosspoint of the beams is 41 in. in front of the lens. A fringe spacing of 50 $\mu$m was used during the experimental investigation. The beam-waist diameter is 500 $\mu$m. The collection optics consist of a set of 5-in.-diam, f/5 lenses; a 90-deg mask (Fig. 13) is used on the collection lens. An EMI9781R side window PM tube is used as the light detector.

The PSI electronics consist of a preamplifier contained with the photomultiplier, a Krohn-Hite model 3202 variable filter, and a PMAP 550 visibility/velocity processor (VVP) (Ref. 13). The electronics are shown in block diagram form in Fig. 14. Signals from the PMT are divided into two portions, the first of which is sent to an integrator and integrated directly. The integral – called the pedestal integral – yields a number which is directly proportional to the mean value of the amplitude since the sinusoidal component of the signal will average to zero. The value of the integral is then fed to the denominator input of an analog divider. The second portion of the signal is bandpass filtered to remove the pedestal and the filtered output is full wave rectified then integrated. The integrated value of the A-C signal is fed into the numerator input of the divider. The output from the divider is sent to an analog-to-digital converter.

The data handling system is comprised of a microprocessor, high-resolution CRT monitor, and a printer with both alphanumerics and graphics capabilities. The system displays the particle size data in histogram form at a maximum resolution of 64 bins per histogram. The particle size data are reduced to prescribed units before printout; for the present investigation, the output was presented in number of particles as a function of particle diameter.

## 2.2.4 Backscattering Particle-Sizing System (BPS)

When a particle is illuminated, it interacts with the electromagnetic radiation and scatters light in all directions. The intensity of the scattered light is directly related to the intensity of the original illumination, the effective size of the particle, and the surface characteristics of the particle. Several instruments have been built which rely on the principle of light scattering to size particles one at a time. Such a device is shown in Fig. 15. A particle in the sampling volume scatters light which is collected, detected, and converted into a voltage. The voltage, above a residual background value, is related through a calibration to the size of the particle. Size distribution is determined by counting the number of pulses of given magnitudes. If the pulse rate and the particle field velocity are known, then the particle concentration can be determined.

The light scattering device selected for evaluation in the icing research test cell was built by Environmental Systems Corporation. The device uses backscattered light to size particles; that is, in Fig. 15 the angle $\theta$ between the laser beam and the light collection optics is 180 deg. The beam forming and light collecting optics are arranged co-axially, and are located in a 3-1/2-in.-diam tube. The tube protrudes into and disturbs the flow field (Fig. 16). Since it disturbs the flow field, the BPS does not meet all of the requirements of the ETF (see Section 2.2.0). However, it was felt that experimental evaluation would provide valuable insight into the particle-sizing capabilities of such a device.

The optical system is shown in Fig. 17. The light source is a Ga-As PN-junction laser that emits a 200-nsec-wide light pulse at $10^3$ pulses/sec. The wavelength of the laser light is 0.904 $\mu$m. The emitted light is focused by a three-lens system to form the sampling volume. The sample volume is 0.5 mm$^3$ and is located 6 in. in front of the lens system. The light scattered by particles in the sample volume is collected by a pair of 1-1/2-in.-diam f/6 lenses. The scattered light is divided into equal parts by a mirror-type beamsplitter and then focused onto two separate detector-preamplifier assemblies. The two detectors along with proper apertures provide a particle rejection system that ensures that a particle passes through the calibration portion of the sample volume.

The signals from the detectors are amplified, digitized, and processed in a microprocessor. The signals from the two detectors are first compared to ensure that they originate from a particle inside the specified portion of the sample volume. Qualified signals are then classified according to magnitude and counted in eight preset particle size bins. Data output is manually controlled. The channel number and the particle counts corresponding to that channel comprise the output data. The particle count is manually recorded from the LED display located on the control panel (Fig. 16).

13

## 2.3 SUPPORTING INSTRUMENTATION

Conventional instrumentation was required to determine test conditions during the experimental program. The instrumentation stations are indicated in Fig. 3. Total temperatures were measured with single-shielded, self-aspirating, copper-constantan thermocouple probes with an ambient reference junction. Pressures were measured with strain-gage-type absolute pressure transducers referenced to atmospheric pressure.

A combination total/static pressure probe (Fig. 3a, detail A) was installed in the test section. Radial surveys of total/static pressure were made across the test section with the probe. The probe positions were determined with an absolute BCD encoder connected to the probe.

A turbine-type flowmeter, installed in the water line to the spray nozzle, was used to determine the water content of the icing cloud. This flowmeter measured all water flowing into the test cell through the spray nozzle and provided primary water content data. The turbine meter has a dynamic range of from 2.5 to 21 gallons per hour.

A rotameter, used to determine the airflow rate to the spray nozzle, was installed in the atomizing air line to the spray nozzle. The rotameter is rated at 300 psi and has a dynamic range for airflows of from 0.5 to 10 standard cubic feet per min.

## 2.4 TEST PROCEDURES

All instrumentation parameters of the support instrument were calibrated before each test. The calibrations were conducted in place with ambient pressure in the test cell. The calibrations included millivolt calibration of all temperature parameters and resistance calibration of all pressure parameters. All calibrations were reviewed and any discrepancies were corrected before the test.

After calibrations were performed, the test cell pressure was reduced to the desired pressure altitude. Cell conditions were allowed to stabilize for approximately five minutes, and a data point was obtained for final instrumentation check. During cell stabilization, a final alignment check was made on the particle diagnostic system to be tested.

After the final instrumentation check, both primary and secondary inlet air was admitted to the test cell at the required pressure and temperature. Airflow through the spray nozzle was also started and was maintained throughout the test to prevent freezing of the spray nozzles. Once the test cell flow conditions had stabilized to steady state, the air purge

through the water outlet of the spray nozzle was stopped, and the desired water and air flows through the spray nozzle were set. The spray water flow rates were selected so that for a given bulk velocity, the resulting liquid water content (LWC) varied with the meterorological conditions of Fig. 1 (i.e., LWC varied from 0.2 to 3 gm/m³). Droplet size information was then obtained with use of the PDS, and at least two holograms or histograms were taken for each spray nozzle test condition. A high-speed minicomputer was used to record the test cell data reported concurrently with the hologram/histogram data. When the test sequence ended, the PDS was reset, the next spray nozzle condition established, and the data acquisition process repeated.

The matrix of test conditions utilized in the experimental program is presented in Table 2. The matrix was chosen to provide the largest range of particle sizes over which the PDS must operate during icing simulation.

The test procedure was utilized throughout the experimental program to evaluate each PDS. The holocamera was first used to determine the water droplet size distribution for each test condition summarized in Table 2. Each of the remaining PDS's was then tested to obtain water droplet size distributions for each test condition of the experimental program.

## 2.5 PRECISION OF MEASUREMENTS

Uncertainties (bands which include 95 percent of the calibration data) of the basic experimental parameters were estimated from repeat calibrations of the instrumentation systems. These uncertainties were estimated against secondary standards whose precisions were traceable to the NBS. The uncertainties were combined by means of the Taylor series method of error propagation (Ref. 14) to determine the precision of the experimental parameters presented in Table 3.

## 3.0 RESULTS AND DISCUSSION

## 3.1 HOLOGRAPHIC DATA

### 3.1.1 Holographic System Calibration

Calibrations of the holographic system (i.e., the holocamera and reconstruction system) were conducted periodically throughout the test program. The purposes of the calibrations were to determine the diameter of the smallest droplet resolvable with the holographic system and to establish a set of calibration factors for the system. Repeat calibrations of the

15

system were necessary throughout the program to ensure that the correct calibration factors were used to reduce the holographic data.

An Ealing resolution chart was used to accomplish the calibration. The resolution chart is a dot and line comparison reticle that is made up of two rows of dots and lines of equal width; the sizes vary from 3 $\mu$m to 100 $\mu$m. The resolution chart was placed at various radial locations in the test plane of the research test cell. Radial locations of 1, 6, 7.5, 14.5, and 17.5 cm on either side of the test cell centerline were chosen to ensure that calibrations were obtained for the entire droplet flow field. Two holograms were taken of the resolution chart at each radial location for a total of 10 holograms per calibration. Each hologram was reconstructed to obtain the diameter size of each of the removable dots.

By plotting the actual dot diameters as functions of the measured dot diameters, the systems calibration function was obtained; this is illustrated in Fig. 18. Each value of measured diameter shown in the figure represents an average of 10 diameters. The error bars shown in Fig. 18 represent the highest and lowest values of measured diameter taken from the 10 sets of data.

Figure 18 shows that the smallest droplet resolvable with the holographic system is 10 $\mu$m. Also, the calibration function, represented by the straight line fit to the calibration data, apparently changed during the experimental program.

The calibration functions were determined from a linear regression curve fit to the calibration data. In all three cases, the coefficient of determination, $r^2$, indicates that the quality of fit achieved by the regression was 0.997 or better. (Note that a value close to 1.00 indicates a better fit than values close to zero.) The equations used to calculate the regression coefficients and the coefficient of determination are given in Appendix B.

The largest shift in calibration occurred during the first portion of the experimental program, between the pretest calibration and the calibration during testing. A comparison of these calibrations revealed that the absolute error in droplet diameter as a result of change in calibrations varied from 1.83 $\mu$m at the smallest (10 $\mu$m) droplet diameter to 5.26 $\mu$m at the largest (100 $\mu$m) diameter. Hence, use of the incorrect calibration function to reduce the holographic data during this portion of the experimental program would increase the value of the smallest resolvable droplet diameter from 10 $\mu$m to 11.83 $\mu$m, and in a like manner the value of the largest droplet diameter would be increased from 100 $\mu$m to 105.26 $\mu$m. Care was therefore taken throughout the experimental program to ensure that the correct calibration was used to reduce the holographic data.

### 3.1.2 Research Cell Calibration

The icing research test cell was calibrated with the holographic system. With the research test cell in the basic configuration (16 ft axial distance between the bellmouth entrance and the test plane) (Fig. 3A), holograms were taken at each of the spray nozzle conditions listed in Table 2. From the 28 holograms taken of the 14 spray nozzle conditions, 7,250 droplet diameters were measured. From 200 to 300 droplets were measured from each hologram. It was assumed that 400 droplet counts were sufficient for statistical analysis of each spray nozzle condition.

The droplet size information obtained from the hologram was used to construct histograms of droplet size distribution. The histograms are plots of the frequency of occurrence as a function of the droplet size range. The histograms shown in Figs. 19, 20, and 21 typify the calibration data.

The calibration data were also used to construct accumulative distributions of the percent of droplets greater than a given droplet size; the data were plotted against droplet size on log-probability paper. The log-probability plots obtained for the histograms of Figs. 19 through 21 are shown in Figs. 22 through 24, respectively. Examination of Figs. 22 through 24 reveals that the plotted data lie on an essentially straight line. This indicates that the calibration data are logarithmically distributed (Ref. 14). Therefore, a normal probability equation with a logarithmic variate can be applied to the droplet size distributions of the calibration data. The frequency with which a droplet of a given diameter occurs is

$$f_i = \frac{1}{\sqrt{2\pi}\, \ell n\, S_g}\, \exp\left\{-\frac{1}{2}\left[\frac{\ell n\, d_i/M}{\ell n\, S_g}\right]^2\right\} \tag{1}$$

The frequency distribution is a unique function of the geometric mean size, M, and the geometric standard deviation, $S_g$; once they have been specified, only one distribution is possible. To compare the droplet distribution obtained from calibration with those droplet distributions obtained from calibration with those droplet distributions obtained by other particle-diagnostic systems, only the values of M and $S_g$ for both distributions need be compared. The geometric mean size is given by

$$\ell og\, M = \sum_{i=1}^{n} \frac{(n_i\, \ell og\, d_i)}{\sum_{i=1}^{n} n_i} \tag{2}$$

17

and the geometric standard deviation by

$$\log S_g = \sqrt{\sum_{i=1}^{n} \frac{n_i(\log d_i - \log M)}{\sum_{i=1}^{n} n_i}} \tag{3}$$

Although the values of M and $S_g$ can be calculated directly from the histogram data with Eqs. (2) and (3), these measures can easily be obtained graphically from the cumulative probability plots. When droplet diameters are log-normally distributed, the median droplet size is equal to the geometric mean droplet size (Ref. 14). The value of M is, for a given distribution, the droplet diameter corresponding to the median (50-percent value) of the probability coordinate of the cumulative probability plots. Further, it can be shown (Ref. 14), that the geometric standard deviation can be obtained from the plots as the ratio of the size at 15.87-percent probability to that at 50 percent, or the ratio at 50-percent probability to that at 84.13 percent. Both the analytical method utilizing Eqs. (2) and (3) and the graphical method just described were used to obtain values of the geometric mean diameter and geometric standard deviation. Table 4 presents, for comparison, values of M and $S_g$ determined by both methods. The geometric mean size defined by Eq. (2) or as determined with the graphical method is based on the count frequency of the given diameter. Historically the mass median diameter ($d_{gm}$) is the central tendency specified as the "mean effective" droplet diameter of an icing cloud (Refs. 15 and 16). This diameter is a mass-weighted average and is defined as the diameter of those droplets for which one-half of the entire liquid water content of the icing cloud is contained in droplets whose diameters are less than $d_{gm}$. Conversion of the geometric mean diameter, M, into the mass median diameter, $d_{gm}$, is accomplished by the transformation

$$\ln d_{gm} = \ln M + 3(\ln S_g)^2 \tag{4}$$

Use of Eq. (4) is appropriate only if a log-normal distribution exists (Ref. 14). Since it had been shown that all of the calibration data are indeed log-normally distributed, then Eq. (4) was used to determine the mass median diameters reported in Table 4. The standard deviations in Table 4 are the geometric standard deviations. As pointed out in Ref. 14, one favorable aspect of the log-normal distribution is that regardless of the basis used for its determination, the geometric standard deviation is the same. Consequently, the results listed in Table 4 completely define the holographic calibration of the spray nozzle conditions of Table 2, for comparison either on a number basis or on a mass basis.

The mass median diameters listed in Table 4 were used in constructing a calibration curve for the spray nozzle. The calibration curve (Fig. 25) is a plot of mass median diameter as a function of the spray nozzle mass flow ratio. (The mass flow ratio is defined as the mass flow rate of spray nozzle atomizing air divided by the mass flow rate of spray nozzle water.) A power curve of the form $y = ax^k$ was fitted to the holographic data and is shown as the solid line in Fig. 25. The regression coefficients for the curve fit were determined by the least-squares method. (The equations used are given in Appendix B.) The curve-fit equation is

$$d_{gm} = 17.87 (\dot{w}_a / \dot{w}_w)^{-0.318} \tag{5}$$

The coefficient of determination for the fit is 0.983, which indicates an excellent fit to the data. The dashed lines of Fig. 25 serve to illustrate that all of the calibration data fall within $\pm 2 \ \mu m$ of the curve.

The spray nozzle operating characteristics (Fig. 25) are fairly "flat" in the 15- to 25-$\mu m$ range; large changes in the mass flow ratio are required to produce small changes in the mass median droplet diameters. Hence, in this range the measured flow rates of spray nozzle atomizing air and water can be used with a high level of confidence to determine the mass median diameter of the icing clouds.

This is not the case, however, for droplet diameters larger than approximately 30 $\mu m$, for in this region of the curve, small changes in the mass flow ratio produce large changes in the mass median diameter. Hence, when the spray nozzle is used to produce a mass median droplet diameter larger than 30 $\mu m$, the calibration curve shown in Fig. 25 cannot be used; rather an independent droplet measurement system, such as a holocamera or one of the other PDS's described in Section 2.0, is required to ensure accurate control of $d_{gm}$.

The holographic calibration data were also used to determine the LWC at the test section of the research test cell. The LWC was calculated by dividing the weight of all droplets counted by the volume of the test section scanned during data reduction; the equation is given in Appendix A. In Fig. 26 the LWC values measured at the spray nozzle are compared with the values calculated from the holographic data. The data clearly demonstrate that the calculated LWC is biased toward higher values. Two conditions that contribute to the biasing are (1) improper droplet focus recognition during hologram reconstruction and (2) large snow or ice crystals in the flow field. Since LWC depends on $d_i^3$, the error in the calculated LWC will be about three times larger than the corresponding error made during measurement of the droplet diameter; hence, failure to correctly size droplets causes serious errors in the subsequent LWC calculations.

Droplet focus recognition is based upon the rate of change of light intensity near the droplet edges (Fig. 27). If the edges are not in focus, the droplet will appear larger than it should, biasing the droplet sizes toward higher values. When snow and/or ice crystals are present in the flow field, the density of water is used to calculate the droplet weight rather than the snow/ice density, and the assumption of spherical droplets inherent to the LWC calculations may be violated, similarly biasing the LWC toward higher values. Determining LWC from holographic data is not, at this time, a viable means of obtaining an accurate measure.

## 3.2 PARTICLE DIAGNOSTIC SYSTEM DATA

Droplet size measurements are presented for each PDS tested. Data were obtained for each PDS at the test conditions listed in Table 2. The research test cell was used in the basic configuration, that is, with a 16-ft axial distance from the bellmouth entrance to the measurement plane of the PDS. At least two droplet size data sets were obtained with each PDS for each test condition (Table 2), and at least 1,000 droplets were sized per data set. In several cases, multiple data sets were made at given spray nozzle test conditions to verify repeatability of the results or to correct experimental deficiencies.

### 3.2.1 FOS Results

Figure 28 is a typical histogram constructed from the droplet size data obtained with the FOS. The first two bins, centered at droplet diameter 3.065 $\mu$m and 6.13 $\mu$m, respectively, are empty. The data channels corresponding to these two bins were extremely noisy, and spurious counts were recorded in these bins during data acquisition. The noise was determined to be electro-optically induced (i.e., caused by weak or out-of-focus droplet images). Since attempts to eliminate the noise in channels 1 and 2 were unsuccessful, these two channels were "amputated" from the histograms. Hence, the smallest droplet resolvable with the FOS, as used in this research, is approximately 7.5 $\mu$m—the smallest droplet diameter corresponding to the third bin.

Figure 29 is a log-probability plot of the histogram data shown in Fig. 28. The data lie along a straight line, indicating that the droplet diameters are log-normally distributed. This was the case for all droplet size data taken with the FOS.

The distribution of the mass median droplet diameters obtained from the FOS data is shown in Fig. 30 as a function of the spray nozzle mass ratio. The results are compared to the empirical distribution for the mass median diameters obtained from the holographic data [Eq. (5), Section 3.12]. This expression provides a reasonable fit to the data; most of

the FOS results lie within the error band of the holographic data, the dashed lines of Fig. 30. This error band is plus and minus two standard deviations ($\pm 2\,S_g$) of the variation between the holocamera data and the empirical distribution of Eq. (5). (See Appendix B for the determination of $S_g$.)

To determine the accuracy with which Eq. (5) predicts the FOS data, the deviations between the measured droplet diameters and the predicted diameters from Eq. (5) are plotted as a function of droplet diameter (Fig. 31). In Fig. 31 the deviations have been fitted with a linear regression least-squares fit. The least-squares line deviates slightly from the line of zero error. However, over the region of interest ($d_{gm} = 15$ $\mu$m to $d_{gm} = 25$ $\mu$m) the deviation is less than one micrometer, which is well within the data scatter of the holocamera. Therefore, the FOS can size icing cloud droplets as accurately as the holocamera.

### 3.2.2 AEDC-PSI Results

A typical histogram of the droplet size information obtained with the AEDC-PSI is shown in Fig. 32. This histogram differs in shape from the histograms obtained with the holocamers data (Figs. 19 through 21) in that at least two maxima or modes of the frequency, $f_i$, are exhibited. Two modes correspond to droplet diameters of 12.5 $\mu$m and 22 $\mu$m. Figure 33 is a log probability plot of this typical histogram. The data do not plot as a straight line; hence, unlike the holocamera data, the droplet size distributions obtained with the AEDC-PSI are not log-normal.

Irani and Callis (Ref. 17) note that the distribution shown in Fig. 33 indicates a log-normal distribution from which particles have been removed. To determine whether the apparent loss in droplets was caused by changes in the research test cell operating characteristic or whether the AEDC-PSI incorrectly sized the droplets, PSI data taken on different days for the same spray nozzle test conditions were compared. Figure 34 is a typical log probability plot showing the comparison. As seen in Fig. 34, the results obtained with the PSI correlate well for the two test dates and are self consistent.

Nine of the data points reported for the holocamera in Sec. 3.1 and all of the FOS data reported in Sec. 3.2.1 were taken in the interval between the PSI test dates, and all of the distributions obtained with both devices were found to be log-normal. Because of the excellent correlation between the holocamera data and FOS data, it was concluded that the droplet clouds produced in the research test cell are log-normally distributed. Further, because the data obtained with the AEDC-PSI were found to exhibit abnormal log-normal yet self-consistent distributions, it was concluded that the apparent loss of droplets indicated by the log-probability plots was attributable to measurement inaccuracies of the AEDC-PSI.

21

The inaccuracies in the droplet size data produced by the AEDC-PSI apparently result from the relatively high number density that exists in a simulated icing cloud. The existence of many droplets in the measurement plane increases the probability that multi-droplets are present in the sample volume during data acquisition. Also, the background noise which is produced by droplets that cross the laser beams outside of the crossover region is increased. Either condition or both would result in biased droplet size data (Ref. 18).

In the case of the AEDC-PSI, the data bias produced by large number densities is toward large droplet diameters. This is illustrated in Fig. 35, which is a plot of the geometric mass mean droplet diameters as a function of the spray nozzle mass ratio. Equation (5) is also plotted in Fig. 35 for comparison. As seen in Fig. 35 the $d_{gm}$ values for the AEDC-PSI data are insensitive to variation in spray nozzle mass ratio; also, in the range of interest (15 $\mu$m to 25 $\mu$m), they exceed the $d_{gm}$ predicted by the holocamera data. It is concluded, therefore, that the AEDC-PSI cannot be used, as presently designed, to size droplets in a simulated icing cloud.

### 3.2.3 Commercial-PSI Results

Figure 36 is a typical histogram of the droplet size data obtained with the commercial-PSI. Compared to the holocamera results shown in Fig. 19, the histogram of Fig. 36 is shifted or biased toward large droplet diameters. The data biasing is also shown by the log-probability plot of the histogram data (Fig. 37). Figure 37 reveals that a simple log-normal distribution (a straight line) does not fit the data. As in the case of the AEDC-PSI data (Section 3.2.2), the log-probability profile looks like a log-normal distribution from which droplets have been removed (Ref. 17).

Throughout the entire experimental program, biasing showed up in the data obtained with the commercial-PSI. Changes in test conditions did not alter the bias; the output of the PSI was insensitive to changes in the spray nozzle mass ratio. This is illustrated in Fig. 38, a comparison between the geometric mean droplet diameters obtained from the PSI data and these derived with Eq. (5). From the results of Fig. 38, and the experience gained with the AEDC-PSI (Section 3.2.2), it was deduced that the data biasing occurred because the number density of droplets in the simulated icing cloud was too large for satisfactory operation of the PSI.

A 90-deg mask was added to the collection lens of the PSI (Fig. 13) to reduce the background noise resulting from the large number of droplets that cross the lasers outside the crossover region. Also, the pinhole in the photomultiplier (PM) tube (Fig. 12) was made smaller to reduce the effective size of the sample volume viewed by the PSI. Neither

changing the pinhole size nor adding the mask reduced the data bias of the PSI data. Consequently, it was concluded that the commercially developed PSI cannot be used in the present configuration to size droplets of a simulated icing cloud.

### 3.2.4 BPS Results

Figure 39 is a typical histogram of the droplet size data taken with the BPS. A comparison between the data of Fig. 39 and the holocamera results of Fig. 19 shows that the BPS data are biased toward the smaller droplets. In fact, it is strikingly apparent that the droplet size distribution displayed in Fig. 39 is monodisperse (i.e., 95 percent of the droplets sized are contained in a single bin — the bin corresponding to a droplet diameter of 8.5 $\mu$m).

Since the accuracy of the holocamera is questionable for droplet diameters smaller than 10 $\mu$m, it is reasonable to ask whether the distribution of Fig. 39 is not more representative of the conditions existing in the simulated icing cloud than is that of Fig. 19. If the droplet size distribution of the cloud is monodisperse, as shown in Fig. 39, then the data rate of the BPS would be approximately 500 droplets/sec (see Appendix C). However, during data acquisition the average data rate obtained with the BPS was approximately 10 droplets/sec.

Although a discrepancy in data rate hardly answers the question of correctness of the histograms, it does point out that the BPS was not functioning as expected. A monodisperse particle generator (Ref. 18) was used to check the calibration of the BPS. This was done by producing a stream of monodisperse water droplets of known size (Ref. 18), using the BPS to obtain a measure of the droplet diameters of the stream, and comparing the actual diameter sizes to the measured sizes. The results are shown in Fig. 40, in which the "line of perfect agreement" is a step function because the BPS data are classified into bins. Hence, a droplet whose actual size falls within a given bin width should be sized by the BPS as the diameter corresponding to the line of perfect agreement. Figure 40 shows that the BPS did not size the 14 $\mu$m and 20 $\mu$m droplets correctly. Each droplet was sized as having an 8.5-$\mu$m diameter. These results showed that the BPS indeed inaccurately sized the droplet diameters. It was therefore concluded that the BPS could not be used as a droplet sizer during icing tests.

### 4.0 SUMMARY AND CONCLUDING REMARKS

A series of experiments was conducted in the icing research test cell to investigate the particle-sizing capabilities of selected particle diagnostic systems. The selected systems include a fiber-optics system, two types of particle-sizing interferometers, and a backscattering particle-sizing system. A holocamera was the baseline device that provided particle size data for comparison.

From calibration of the holographic system it was concluded that the smallest particle resolvable with the present holocamera is 10 $\mu$m. It was also determined that the calibration functions for the holographic system change with time. Therefore, to ensure that the correct calibration functions are used, repeated calibrations are required during data reduction.

Calibration of the icing research cell with the holocamera revealed that the diameters of the droplets varied from 10 to 90 $\mu$m and that the distributions of the droplet diameters are expressible as logarithmic normal functions. Utilizing the log-normal characteristics of the distributions, a central tendency and a measure of the dispersion of the droplet diameters about the central tendency were found for each calibration condition. The mass median diameter was the measure of central tendency used, and the geometric-standard deviation was used as the measure of dispersion.

A correlation between the mass median diameter and the spray nozzle mass ratio is presented, and a power law was dervived to describe the correlation. The mass median diameter decreases with an increase in spray nozzle mass ratio; this dependence can be used as a spray nozzle calibration. Thus, in the applicable range of the calibration curve, which for the mass median diameter is from 15 to 25 $\mu$m, only one droplet diameter need be reported for each calibration condition.

Data obtained with the fiber-optics system were also log-normally distributed. The power law used that described the calibration data also correlated the mass median diameters obtained from the fiber-optics data and the spray nozzle mass ratio. Although a small negative bias exists when the mass median diameters are determined with the fiber-optics system, the bias is within the error limits of the holocamera. It is concluded, therefore, that the fiber-optics systems can be used in a simulated icing cloud environment to determine the droplet size distribution and the effective mean droplet diameter.

Since the data obtained with both types of particle-sizing interferometers were biased toward large droplet diameters, it was concluded that neither the AEDC-developed PSI nor the commercially developed PSI can be used, as presently designed, to size droplets in a simulated icing cloud. The accuracy of the results is dependent on factors related to the high number density of water droplets rather than on the inherent accuracies of the instruments. It was inferred that the presence of large numbers of droplets within the measurement plane increases the probability of multiparticle sampling and also severely increases the background noise. These effects can be minimized or eliminated with the use of off-axis scatter detection (Ref. 19). As pointed out by Bachalo et al. (Ref. 19), the use of off-axis scatter detection extends, by an order of magnitude, the range of particle number density in which an interferometer can operate. With such an increase in the range of operation, the

interferometer could become a viable means of sizing droplets in a simulated icing cloud. It is suggested that the off-axis interferometer be evaluated to determine its effectiveness in a simulated icing cloud.

The data obtained with the backscattering particle-sizing system were monodisperse and inaccurate. Thus, the backscattering particle-sizing system could not be used to measure droplet size during icing tests.

## REFERENCES

1. Federal Aviation Administration, "Airworthiness Standards: Transport Category Airplanes, Appendix C." *Federal Aviation Regulations*, Part 25.

2. Gall, E. S. and Floyd, F. X. "Icing Test Capability of the Engine Test Facility Propulsion Development Test Cell (J-1)." AEDC-TR-71-94 (AD729205), August 1971.

3. Willbanks, C. E. and Schulz, R. J. "Analytical Study of Icing Simulation for Turbine Engines in Altitude Test Cells." AEDC-TR-73-144 (AD77069), November 1973.

4. Farmer, W. M., Burgess, K. S., and Trolinger, J. D. "Holocamera for Examination of Water Droplets in a Large High Altitude Test Cell." AEDC-TR-70-181 (AD715916), December 1970.

5. Belz, R. A. "Resolution Limits of Fraunhoffer Holography." AEDC-TR-70-32 (AD706403), May 1970.

6. Trolinger, J. D. "Laser Instrumentation of Instrumentation for Flow Field Diagnostics." AGARD-AG-186, March 1974.

7. Belz, R. A. and Menzel, R. W. "Particle Field Holography at Arnold Engineering Development Center." *Optical Engineering*, Vol. 18, No. 3, May-June 1979, pp. 256-265.

8. Knollenburg, R. G. "The Optical Array: An Alternative to Scattering or Extinction for Airborne Particle Size Determination." *Journal of Applied Meteorology*, Vol. 9, No. 1, February 1970.

9. Bentley, H. T. "Fiber Optics Particle-Sizing System." AEDC-TR-73-111 (AD766647), September 1973.

10. Farmer, W. M. "Measurement of Particle Size, Number Density, and Velocity Using a Laser Interferometer." *Applied Optics*, Vol. 11, No. 11, November 1972, pp. 2603-2616.

11. Roberds, D. W., Bomar, B. W., and Menzel, R. W. "Interferometric Particle Sizing." AEDC-TR-77-116 (AD-A053729), April 1978.

12. Roberds, D. W., Brasier, C. W., and Bomar, B. W. "Use of a Particle Sizing Interferometer to Study Water Droplet Size Distribution." *Optical Engineering*, Vol. 18, No. 3, May — June 1979, pp. 236-242.

13. *User's Manual — PMAP550 Visibility/Velocity Processor*. Spectron Development Laboratories, Inc., SDL 78-6279, 27 December 1979.

14. Cadle, R. D. *The Measurement of Airborne Particles*. John Wiley and Son, Inc., New York, 1975.

15. Langmuir, I. and Blodgett, K. "Mathematical Investigation of Water Droplet Trajectories." Air Material Command Technical Report No. 5418, Army Air Force, February 1946.

17. Irani, R. R. and Callis, C. F. *Particle Size: Measurement, Interpretation, and Application*. John Wiley and Sons, Inc., New York, 1963.

18. Berglund, R. N. and Lui, B. Y. H. "Generation of Monodisperse Aerobol Standards." *Environmental Science and Technology*, Vol. 7, February 1973, pp. 147-153.

19. Bachalo, W. D., Hess, C. F., and Hartwell, C. A. "An Instrument for Spray Droplet Size and Velocity Measurements." ASME Publication No. 79-WA/GT-13. Presented at the annual meeting, New York, December 2 — 7, 1979.

26

Altitude: Sea Level to 22,000 ft
Maximum Vertical Extent: 6,500 ft
Horizontal Extent: 20 miles
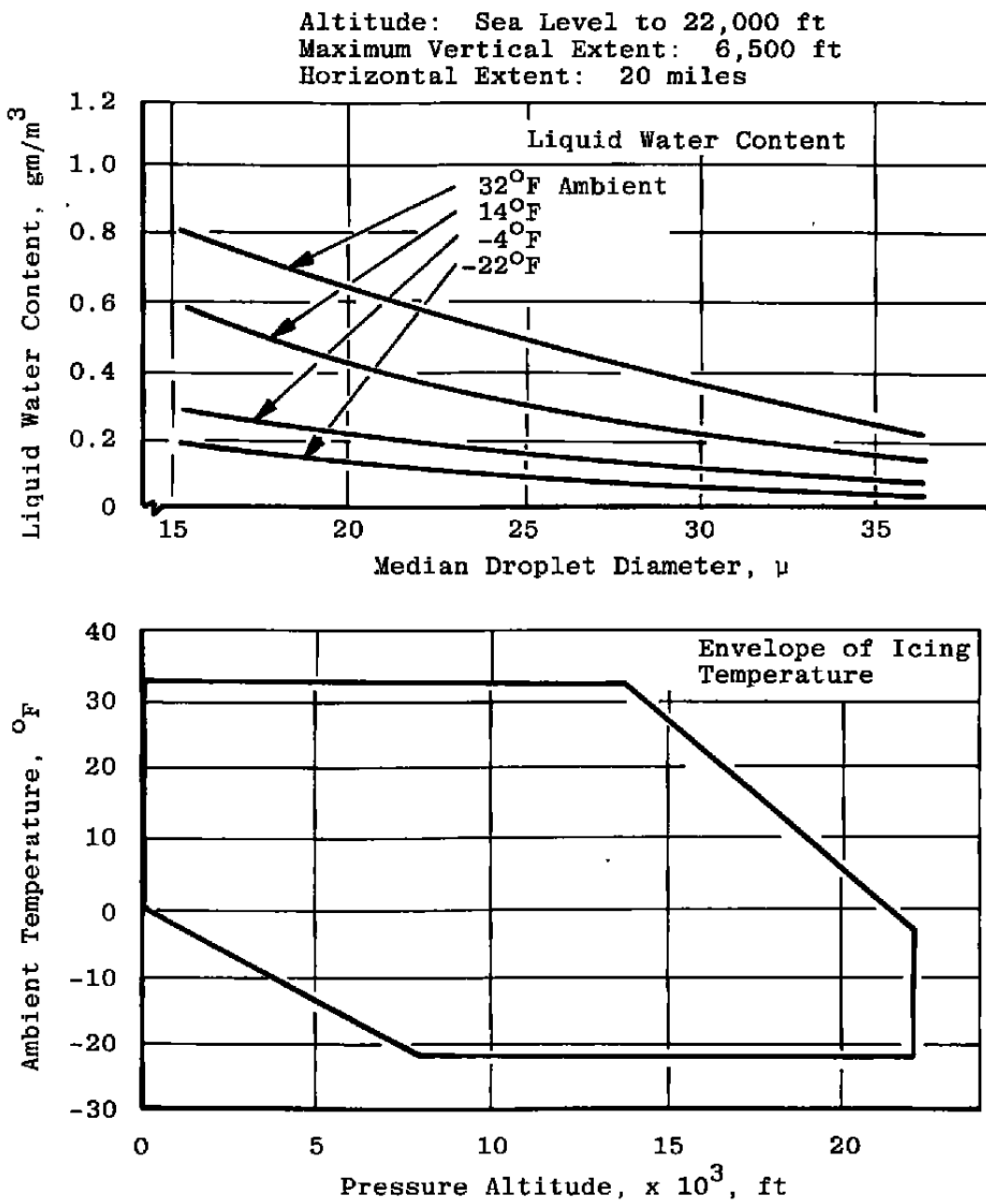


a. Continuous maximum (stratiform clouds)
Figure 1. Cloud icing condition.

Altitude: 4,000 to 22,000 ft
Horizontal Extent: 3 miles
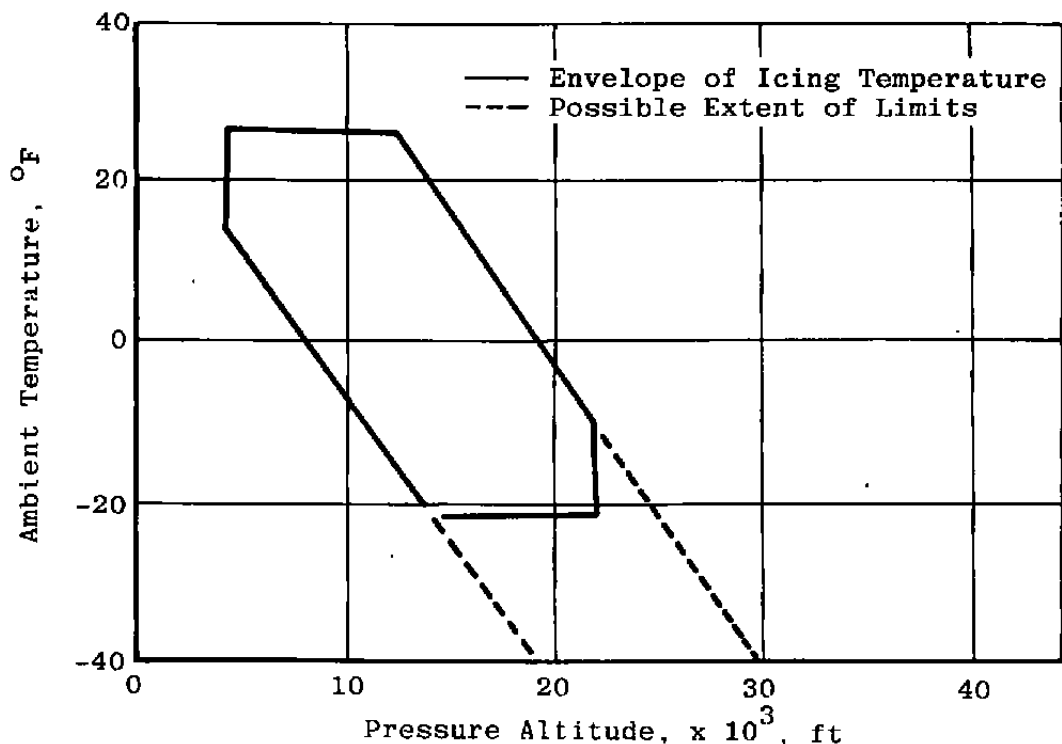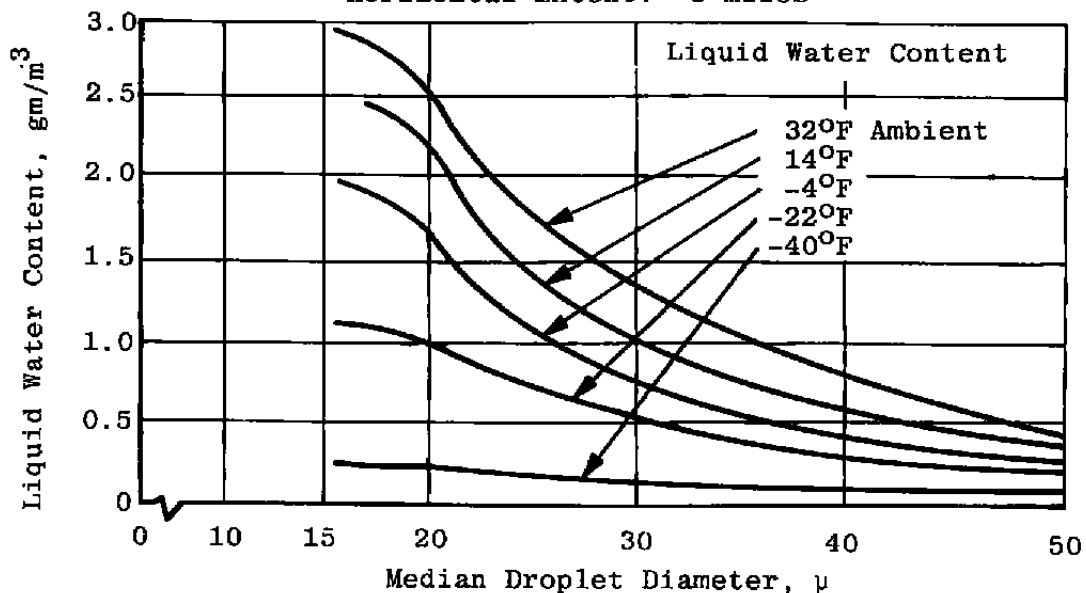


b. Intermittent maximum (cumuliform clouds)
Figure 1. Concluded.

Bellmouth

Thrust Stand

Airflow
Entering Plenum

To Facility
Exhausters

Labyrinth Seal

Turbine Engine
Installation

Plenum Grid

Air Duct

Test Cell Wall

Spray Manifold System for Creation of an
Icing Spray Cloud of Droplets

Spraybars with Atomizing Nozzles
for Water Injection into Airflow

View A-A
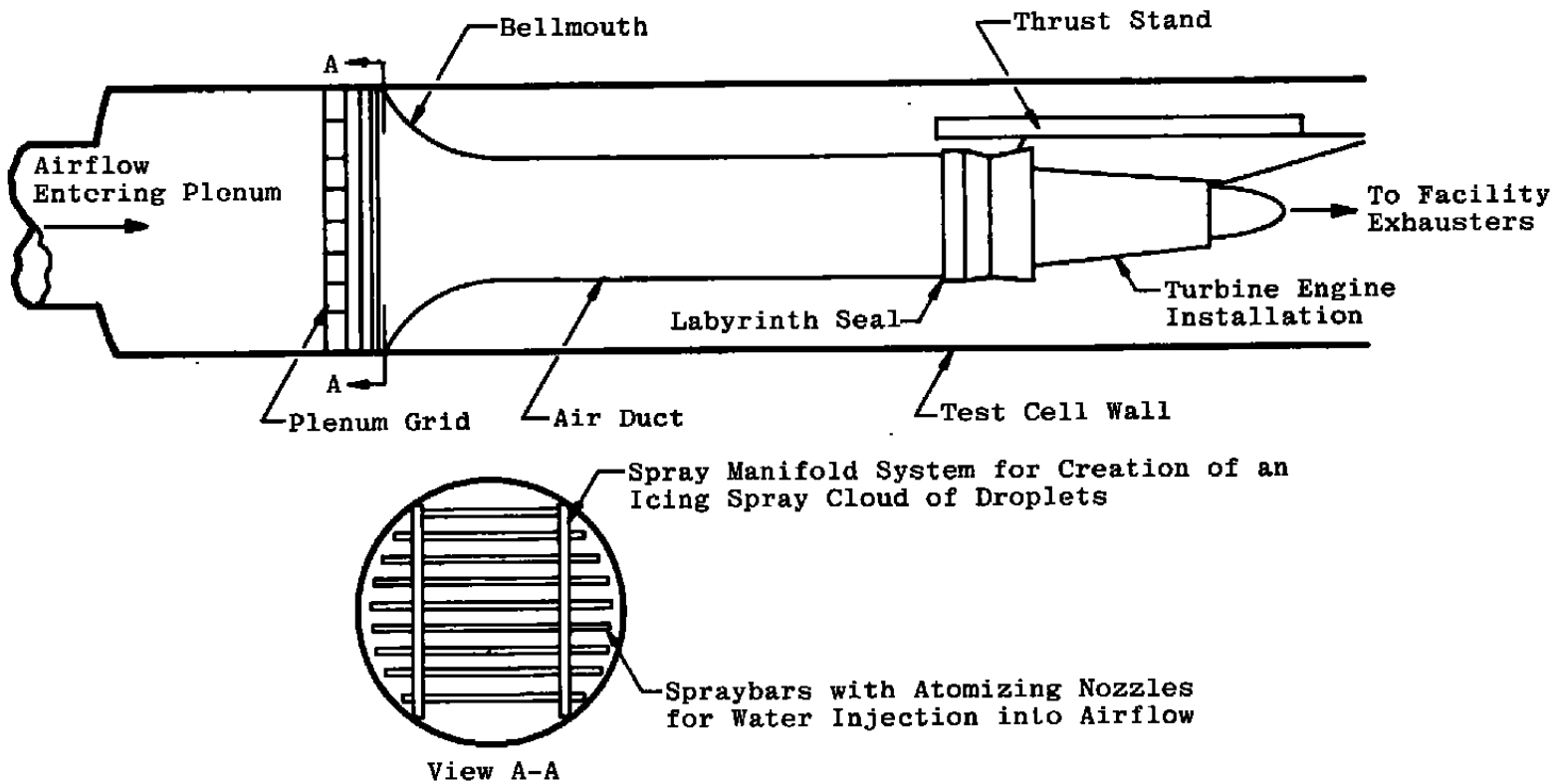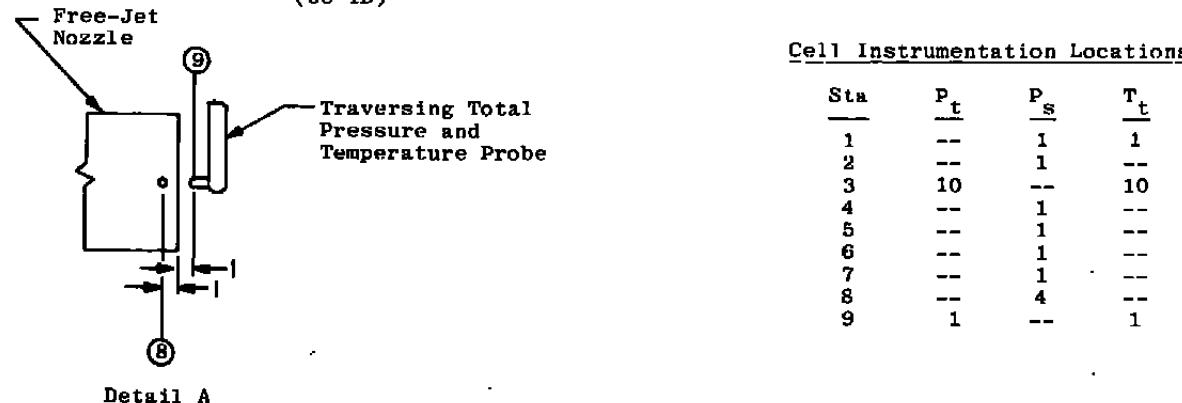
a. Direct connect

Figure 2. Propulsion engine altitude icing test cell configuration.

Air Atomizing Water
Spray Nozzle (Typ 15 Places)⌐

Hologram System
for Water
Droplet Size
Determination⌐

⌐Air Induction System Inlet

⌐BHC Model 214A
Helicopter Test ⌐Test Cell
Rig with Engine⌡

⌐Inlet Duct

Flow

Flow⟶ To Facility
Exhausters

└Inlet Duct

└Free-Jet Nozzle Exit

└Free-Jet Nozzle Insert
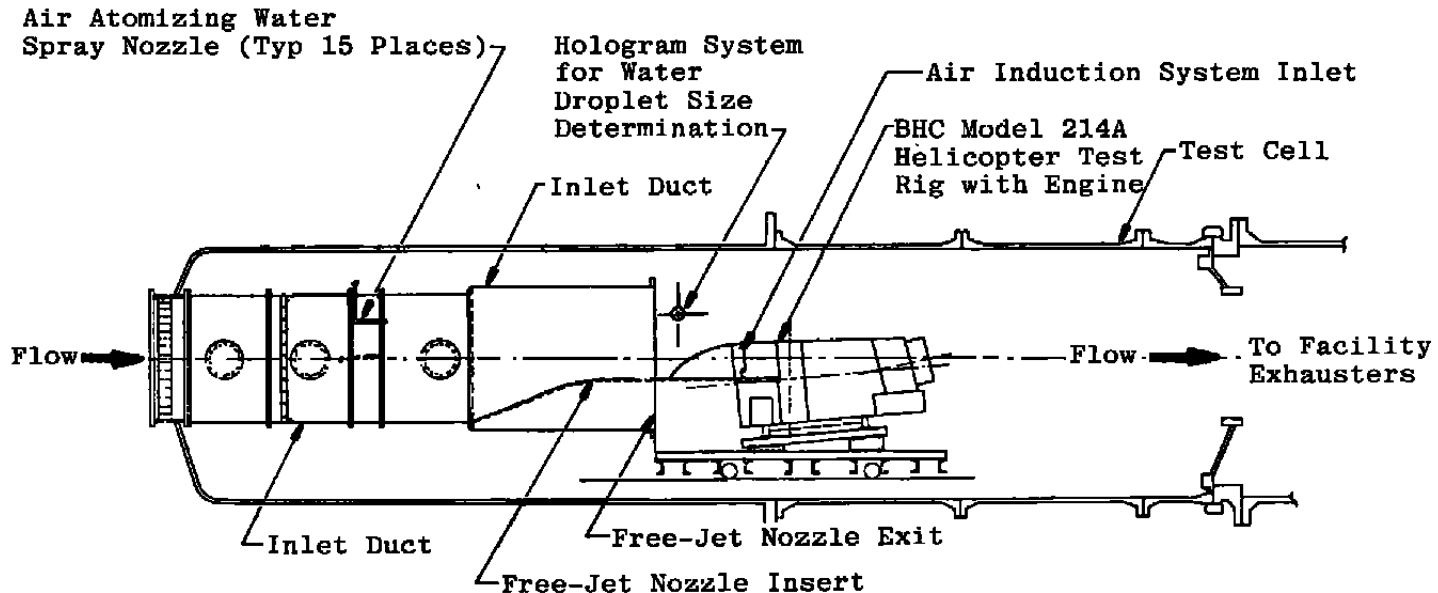
b.  Free jet
Figure 2.  Concluded.

Flow Distributor (Perforated
Plate, 60-percent Solidity)

Flow Smoothing Screen
(3.5 Mesh, 0.063 Wire Diam)

Secondary
Air Supply

④⑤

Supply Line
(12 ID)

Instrumentation
Port (6.0-Diam
Window)

② ③ Bellmouth

① Connecting ⑥ ⑦
Duct (12 ID)

Primary
Air Supply

To ETF Exhausters

←10

34

x = 2, 4, 8, 12, 16 ft→ Detail A

Venturi (6.75
Throat Diam)

⑧

Water Spray Nozzle

Plenum Chamber
(36 ID)

All Dimensions in Inches
Unless Noted

Free-Jet
Nozzle

⑨

Traversing Total
Pressure and
Temperature Probe

Cell Instrumentation Locations

| Sta | $P_t$ | $P_s$ | $T_t$ |
|-----|-------|-------|-------|
| 1 | -- | 1 | 1 |
| 2 | -- | 1 | -- |
| 3 | 10 | -- | 10 |
| 4 | -- | 1 | -- |
| 5 | -- | 1 | -- |
| 6 | -- | 1 | -- |
| 7 | -- | 1 | -- |
| 8 | -- | 4 | -- |
| 9 | 1 | -- | 1 |

⑧

Detail A

a. Schematic of general layout
Figure 3. Icing research test cell.

Viewing Ports

Instrumentation Port

Connecting Ducts

Plenum Chamber

Test Section

AEDC 76-770
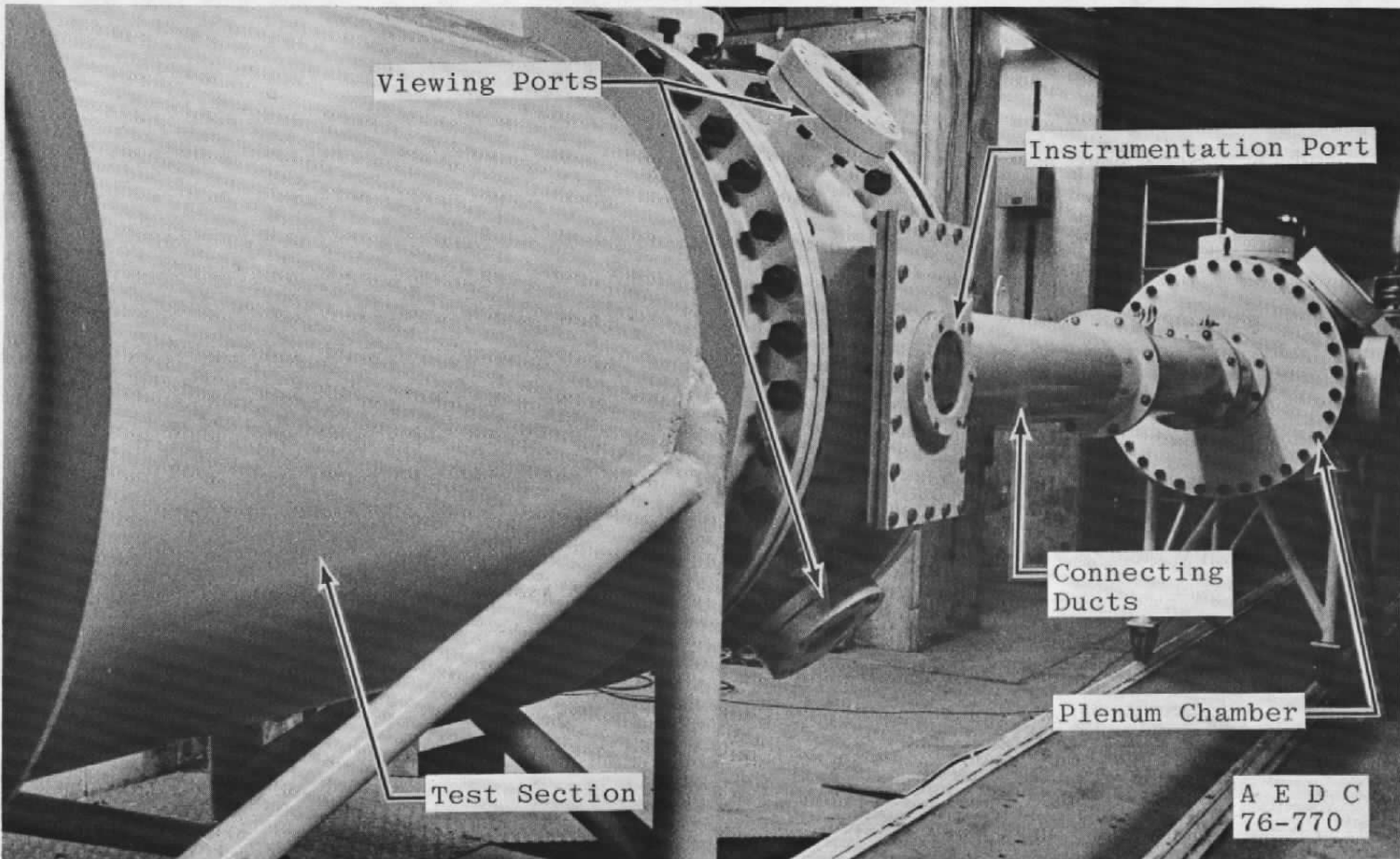
b. Icing research test cell looking upstream
Figure 3. Continued.

Sym
| | |
|---|---|
| A | Actuator |
| Γ | Exhaust |
| FM | Flowmeter |
| HR | Rotameter |
| PT | Pressure Transducer |
| T/C | Thermocouple |

Sym
| | |
|---|---|
| HR | Hand Regulator |
| P | Pressure Transducer |
| RR | Remote Regulator |
| FCV | Flow Control Valve |
| V | Vent |
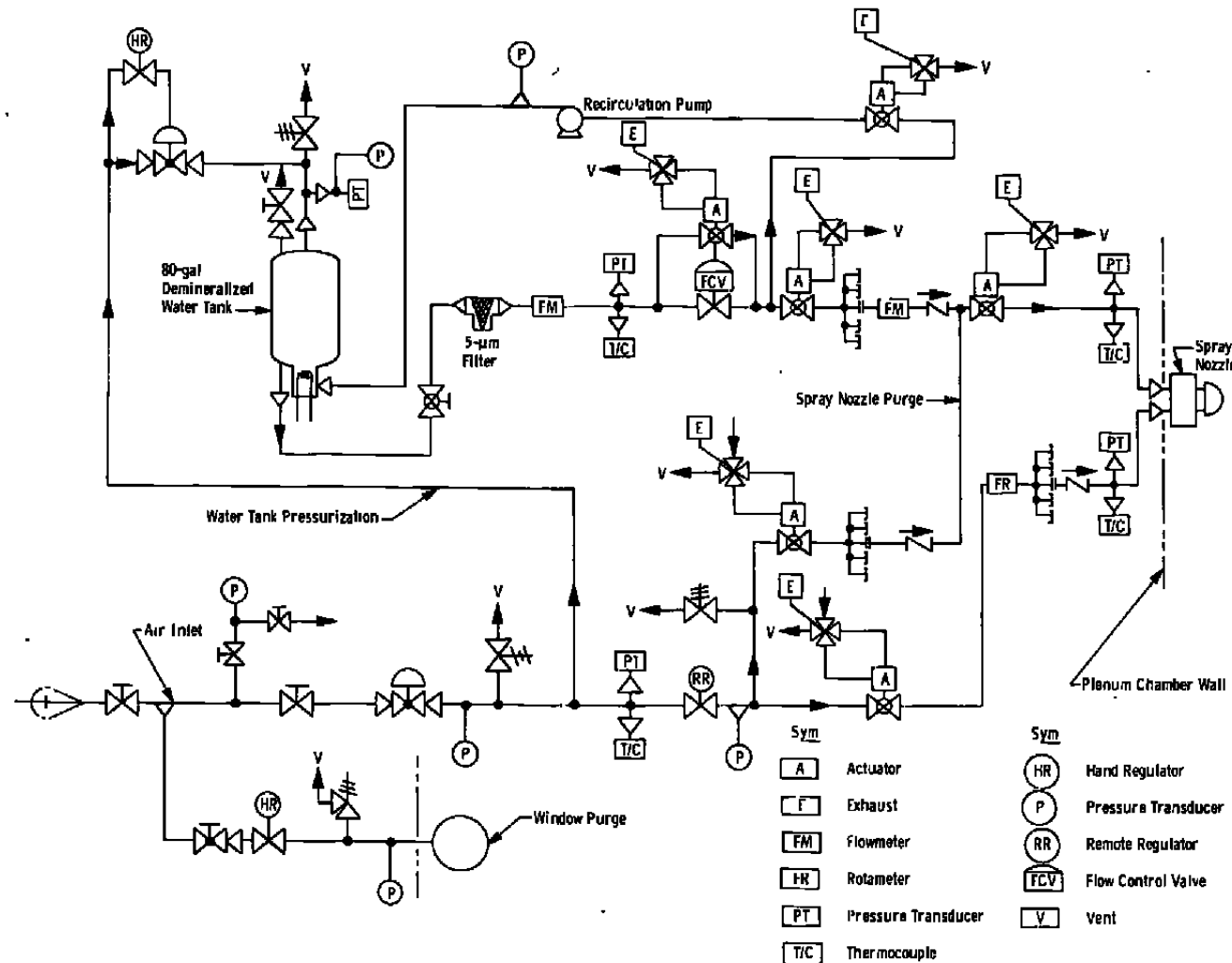
c. Schematic icing spray system details

Figure 3. Continued.

Spraying Systems
Company No. 26B
Atomizing Nozzles

Air Cap
No. 140-6-37-70°

Fluid Cap
No. 40100

Rear View

Side View

No. 63 Drill (6)

No. 44 Drill (3)

No. 59 Drill (1)

Front View

A E D C
2245-75

Lock Nut

Air Cap

Fluid Cap
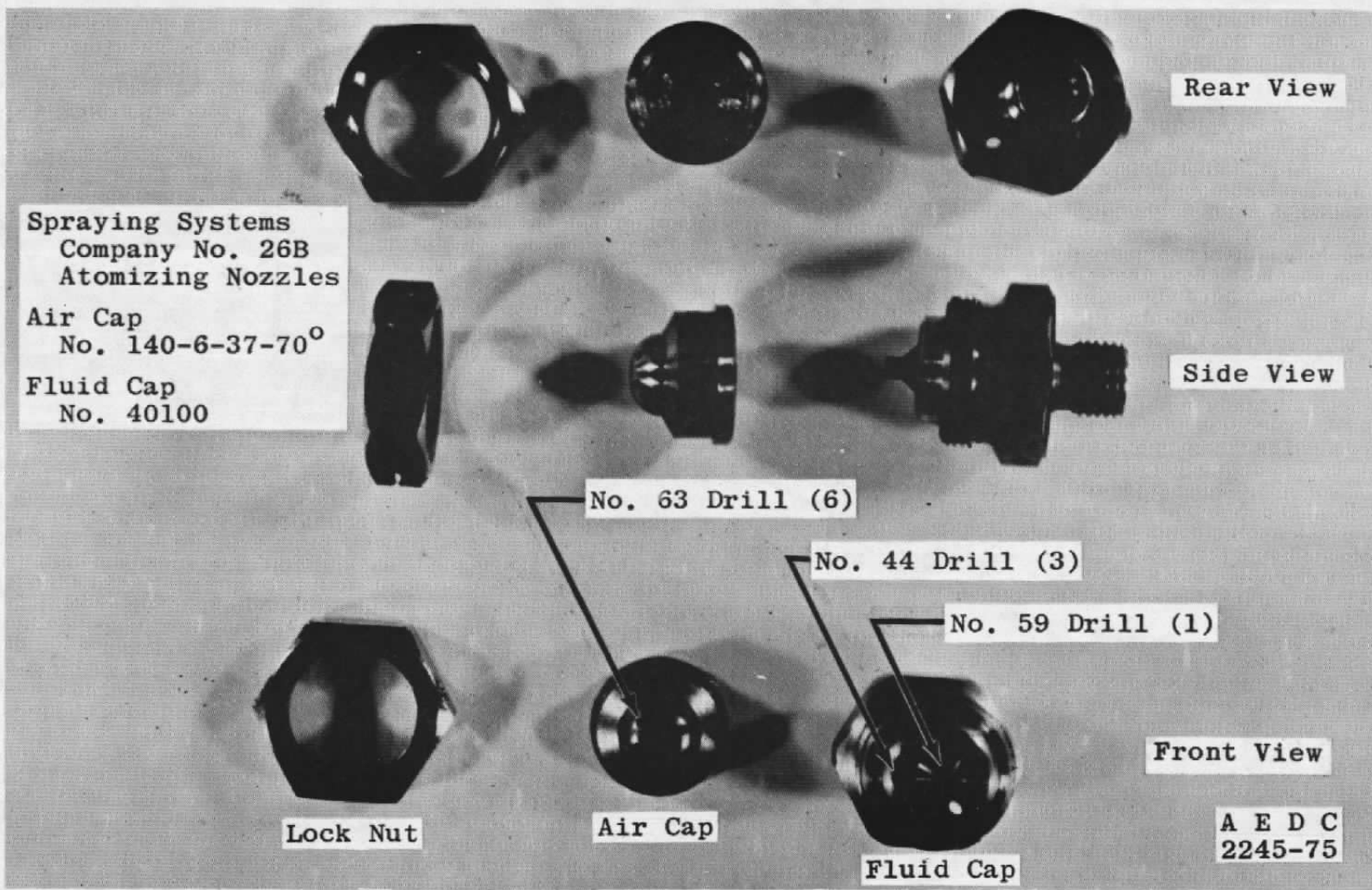
d. Water spray nozzles
Figure 3. Concluded.
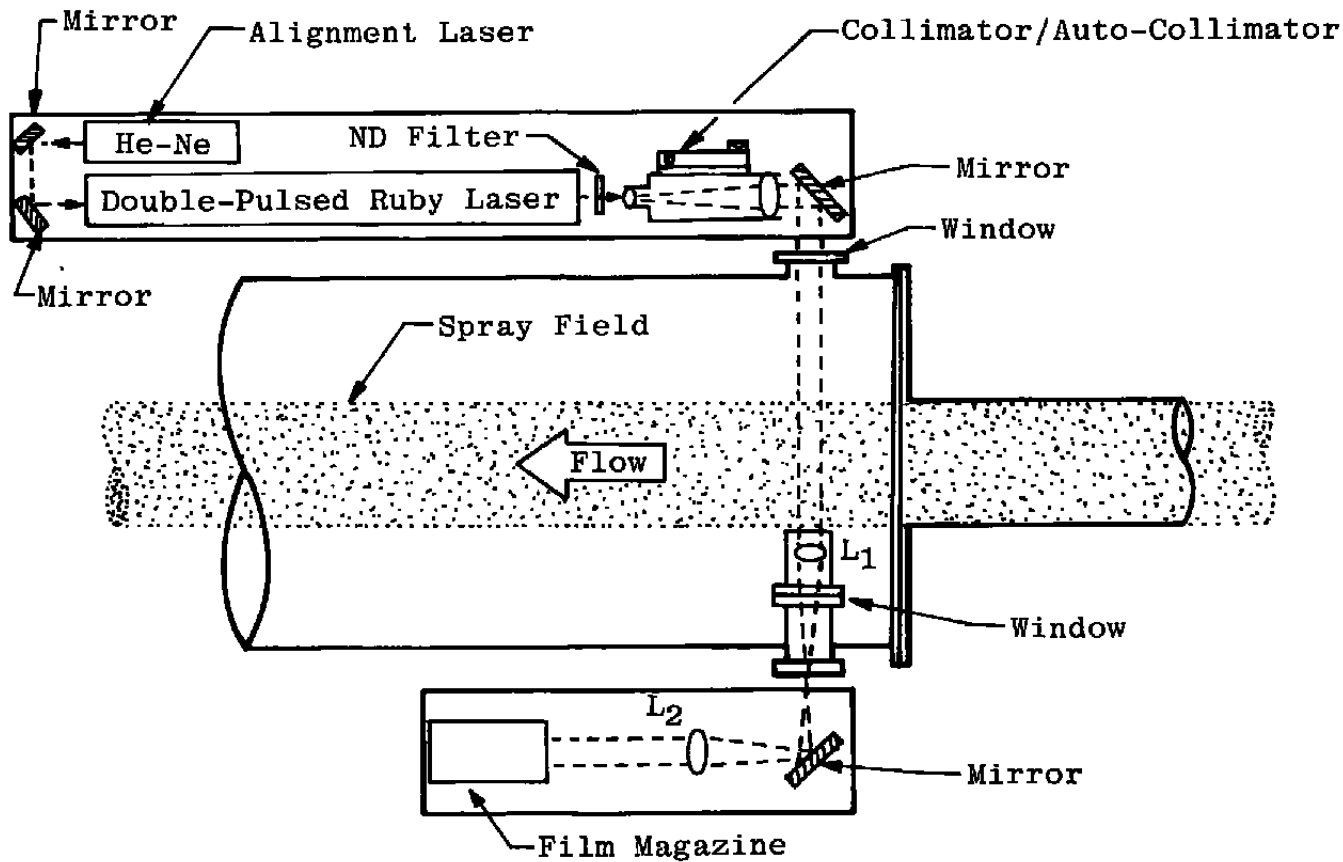
Figure 4. Research icing facility holocamera.

Cover

Pinwheel

Plate Holders

Top Door

13.25 in.

Shutter

Index Tab

LED

Plate Lift
Plunger

Actuation Cylinder

17.10 in.
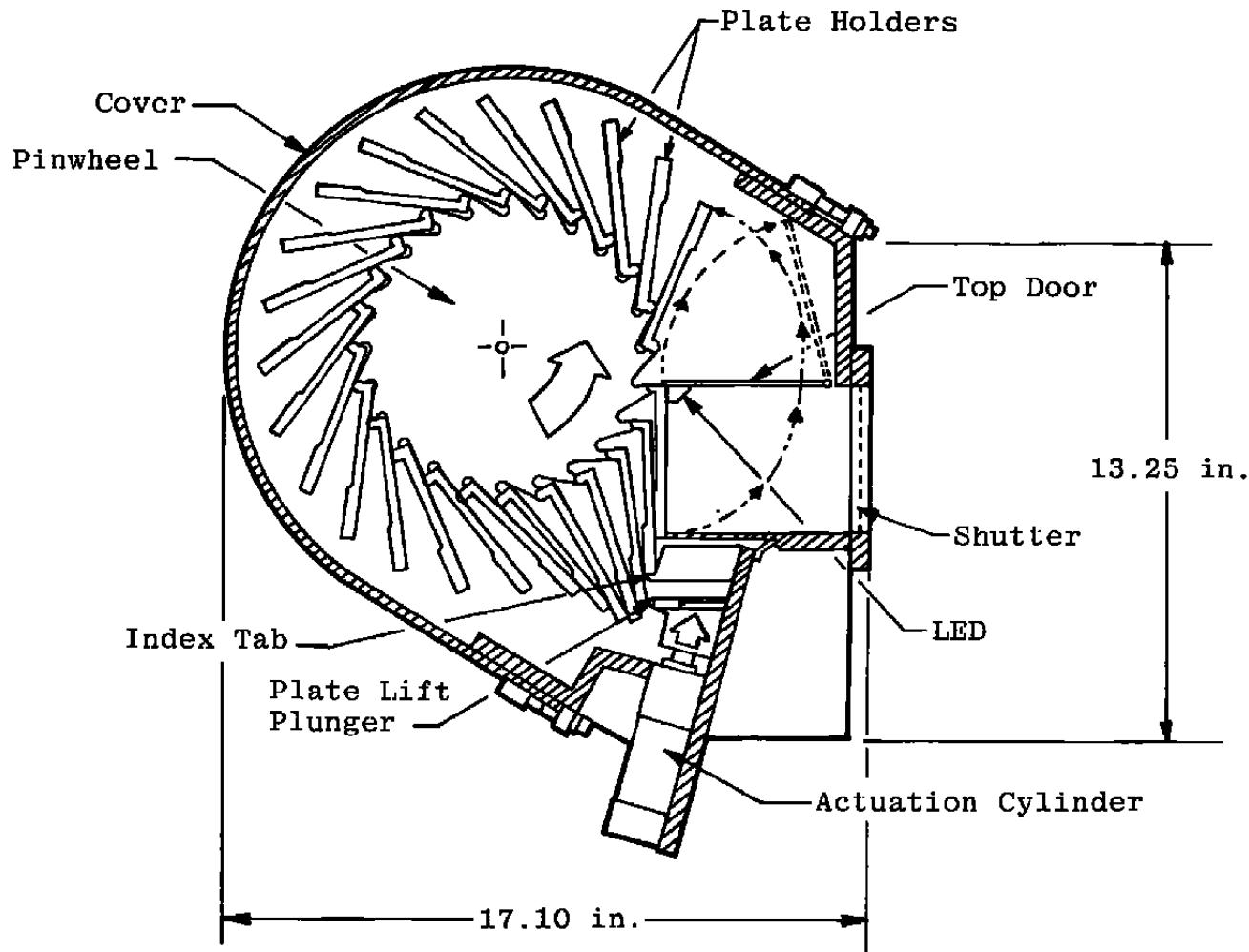
Figure 5.  Multiple glass plate magazine.
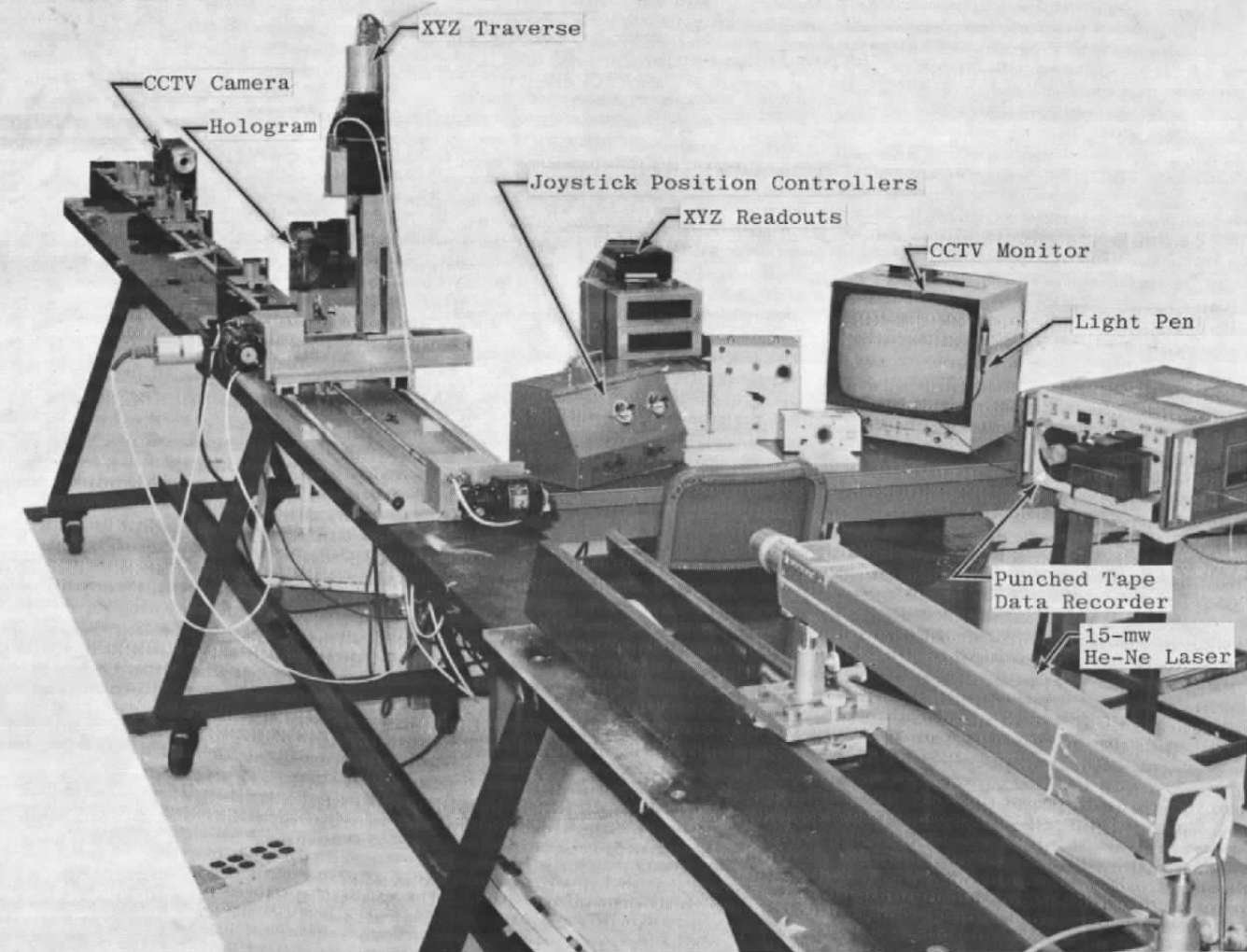
Figure 6. AEDC semi-automated hologram reconstruction system.
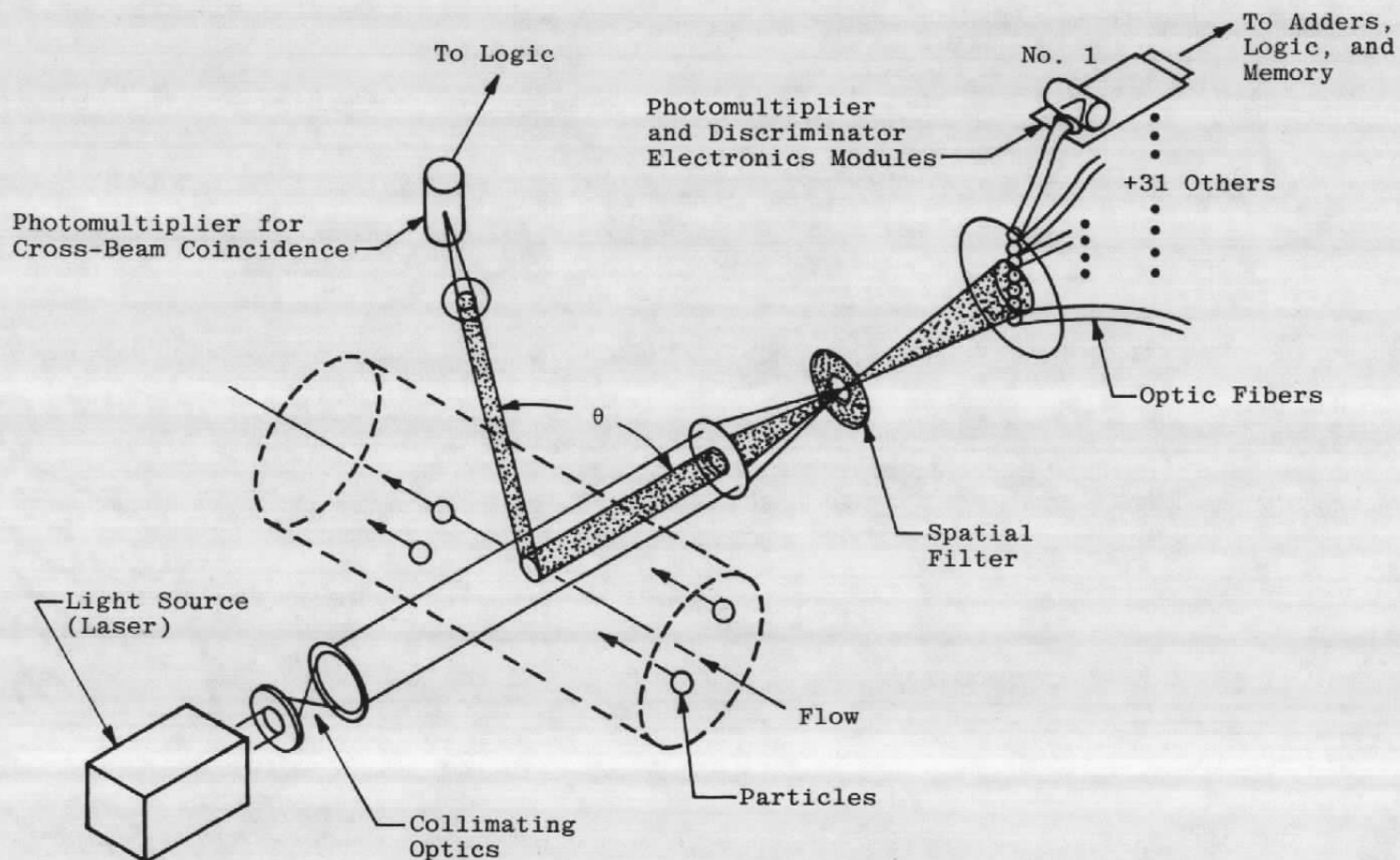
Figure 7. Fiber-optics particle-sizing system.
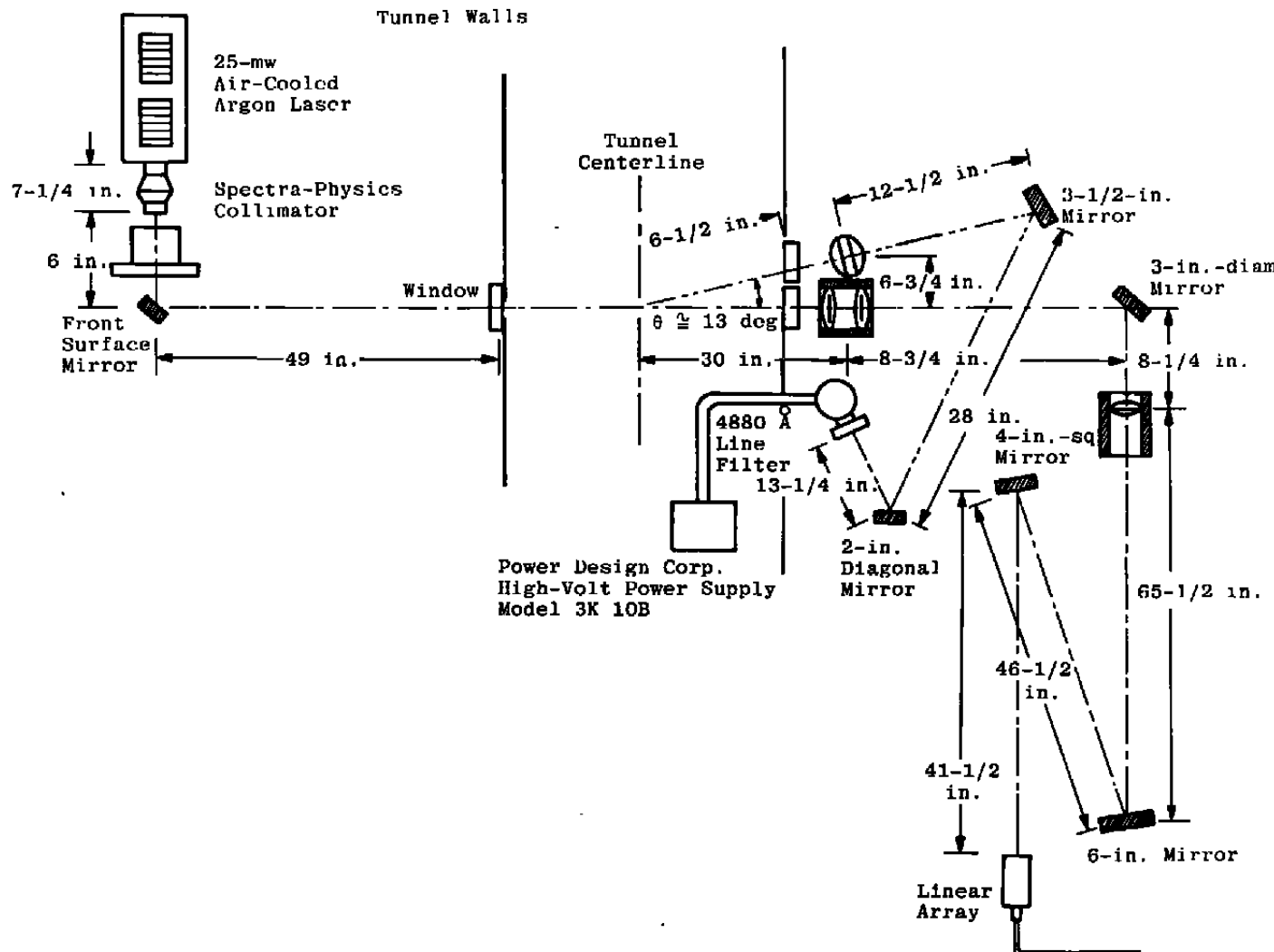
Figure 8.  FOS optical arrangement.
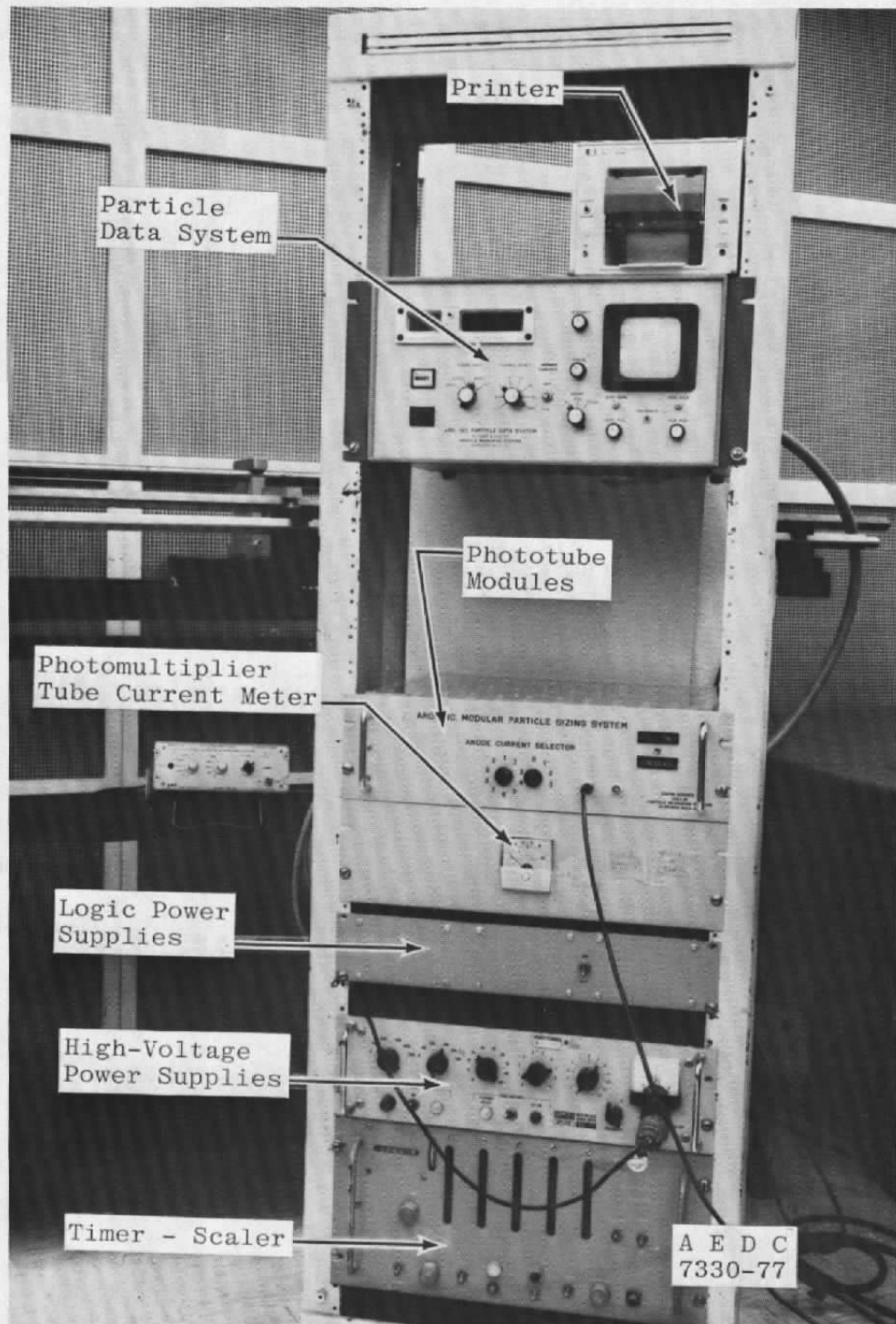
Figure 9. FOS data handling system.
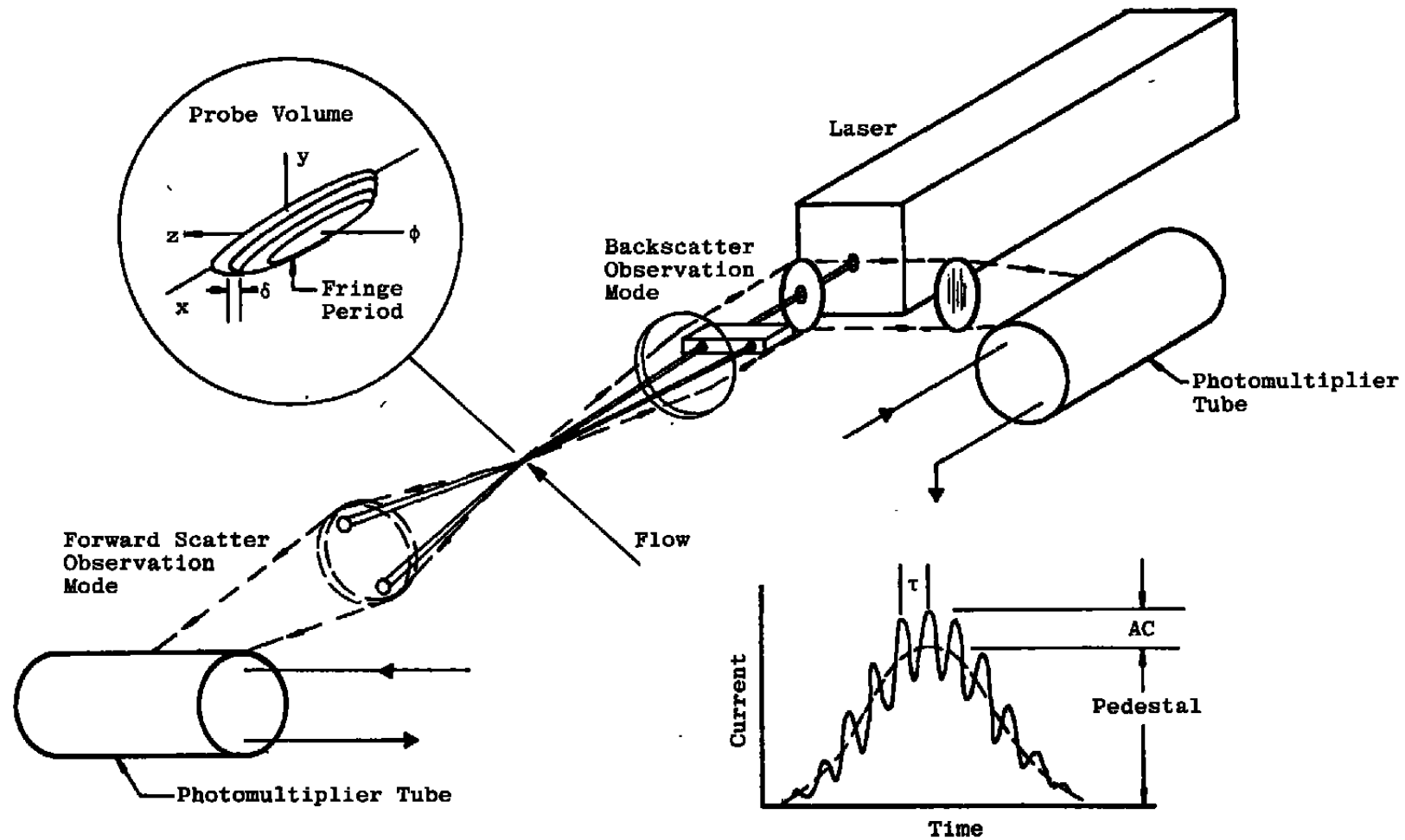
Figure 10.  Particle-sizing interferometer.
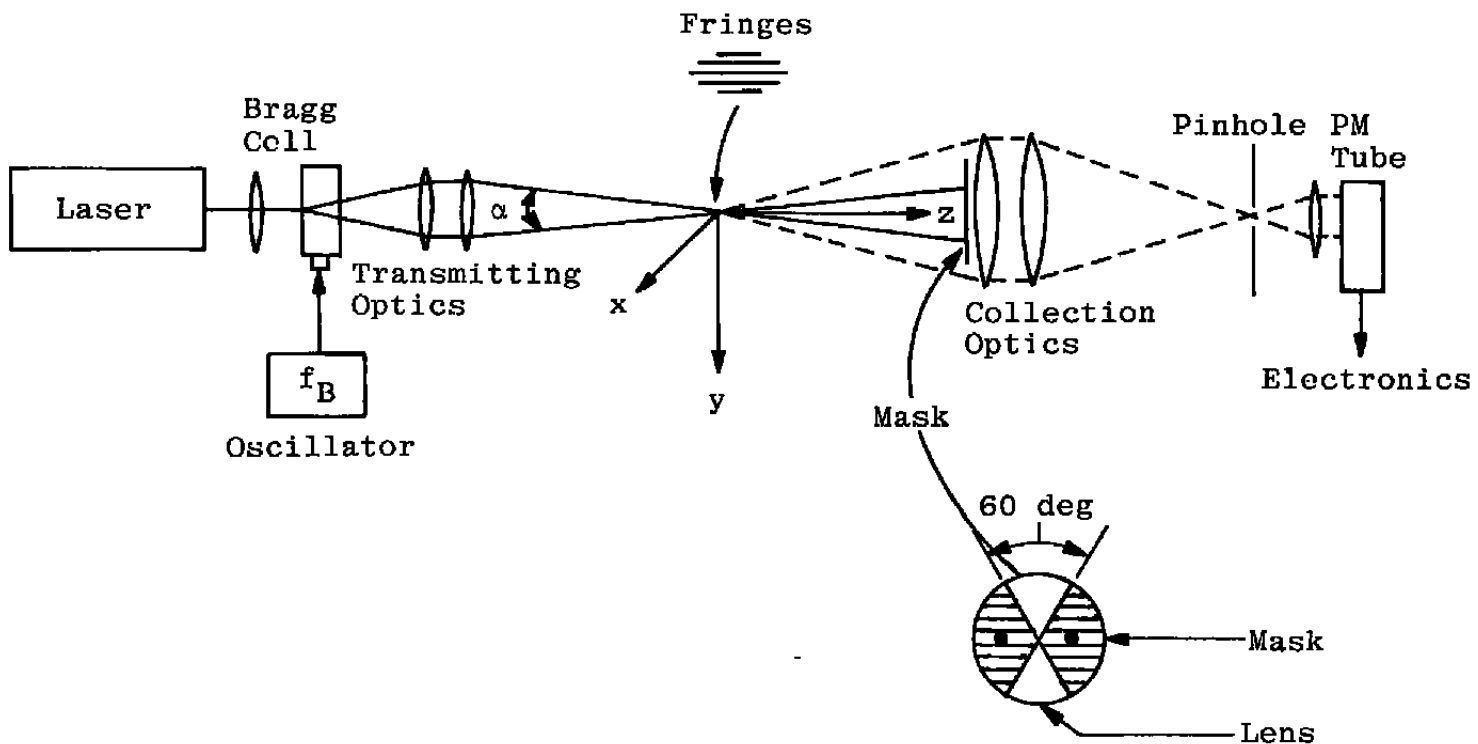
Figure 11.  AEDC-developed PSI  optical system.

High during Signal Passage,
Falling Edge Initiates
Analog-to-Digital Conversion

Comparator

A-C Magnitude

$V_{Ref}$ (Selected
Minimum
Signal Level)

| Amplifier | Bandpass Filter | Envelope Detector | Peak Detector |

PM Tube

Peak Visibility, Digital Output

| Analog Divider | Analog-to-Digital Converter |

| Amplifier | Low-Pass Filter | Peak Detector |

Pedestal
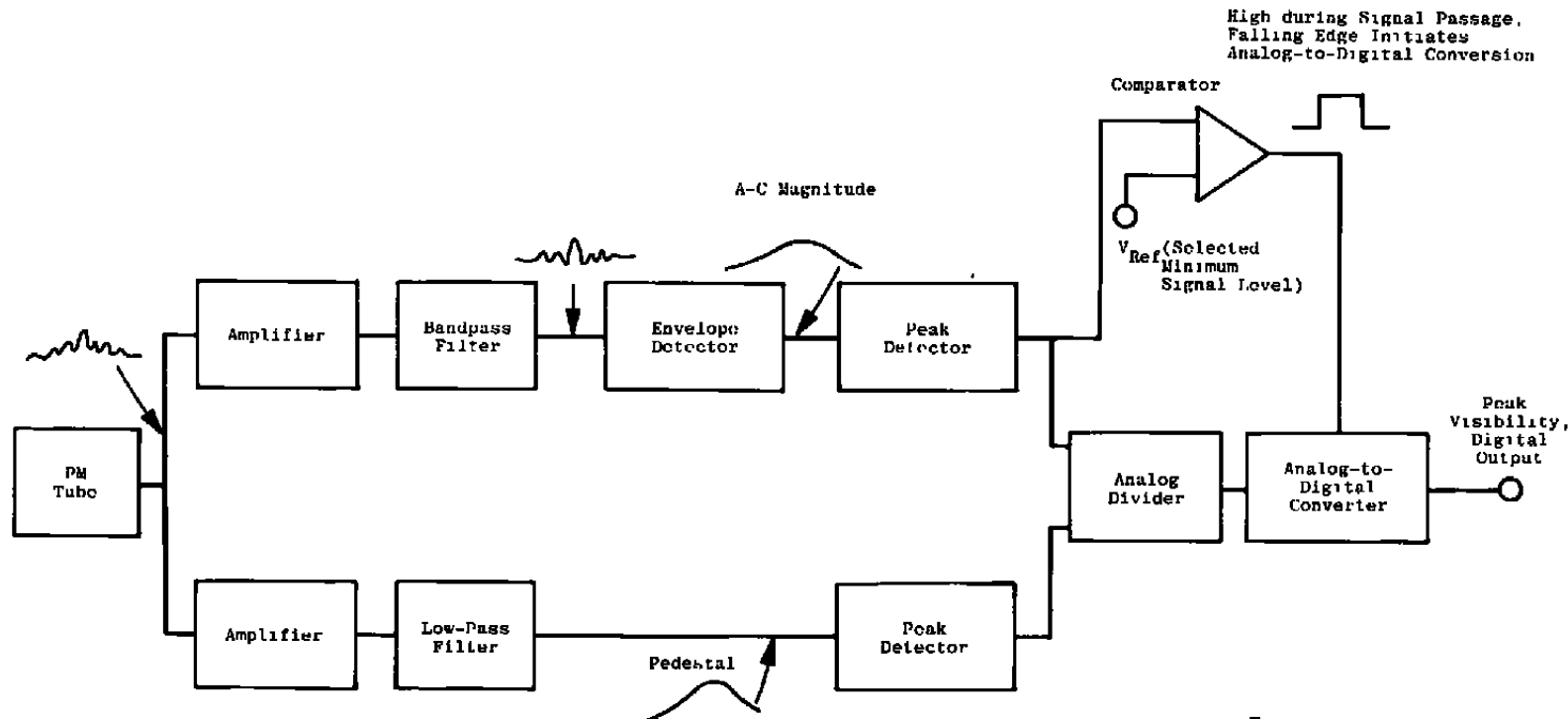
Figure 12. Electronics for AEDC-developed PSI.
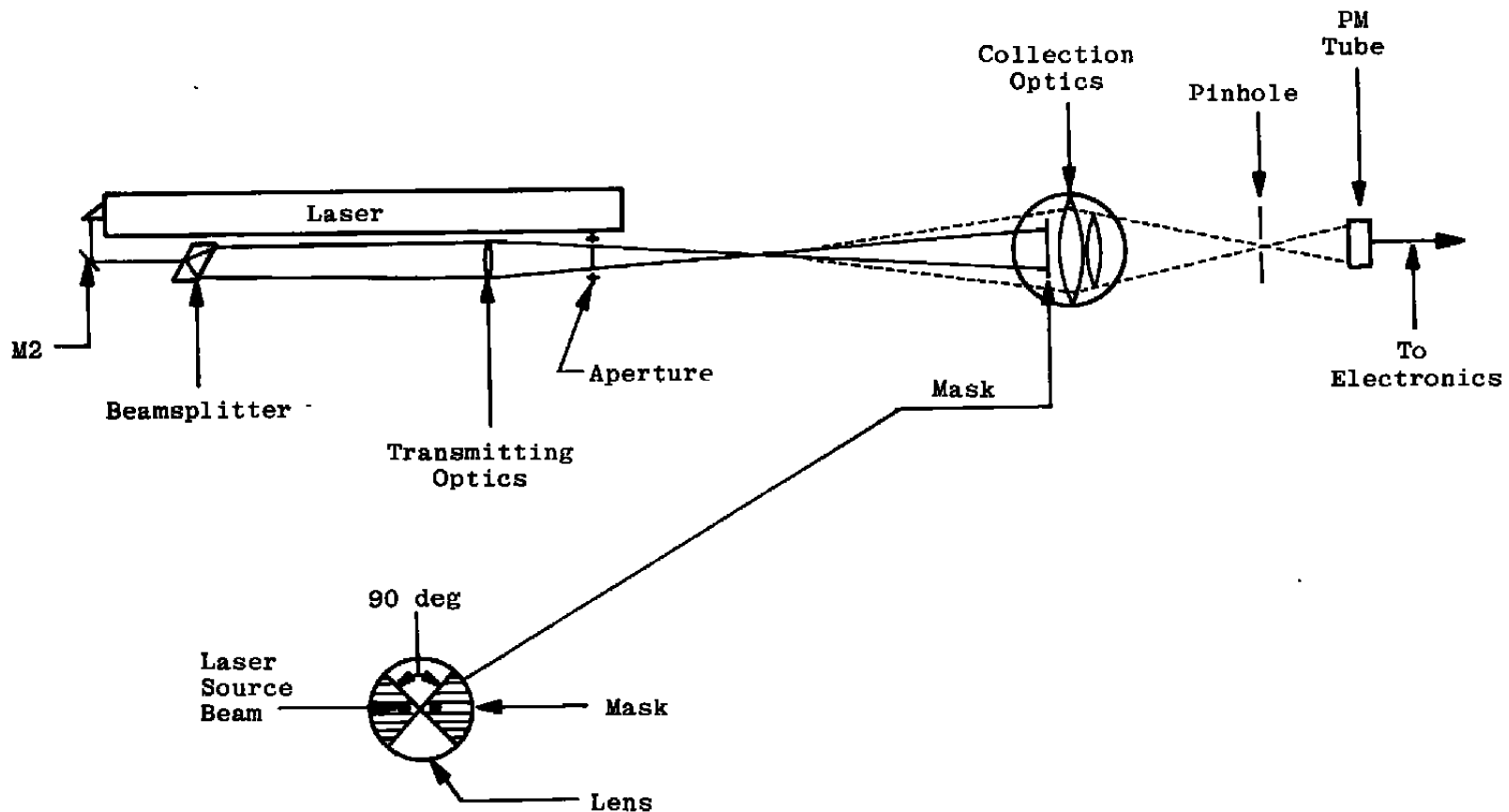
Figure 13. Commercial-PSI optical system.
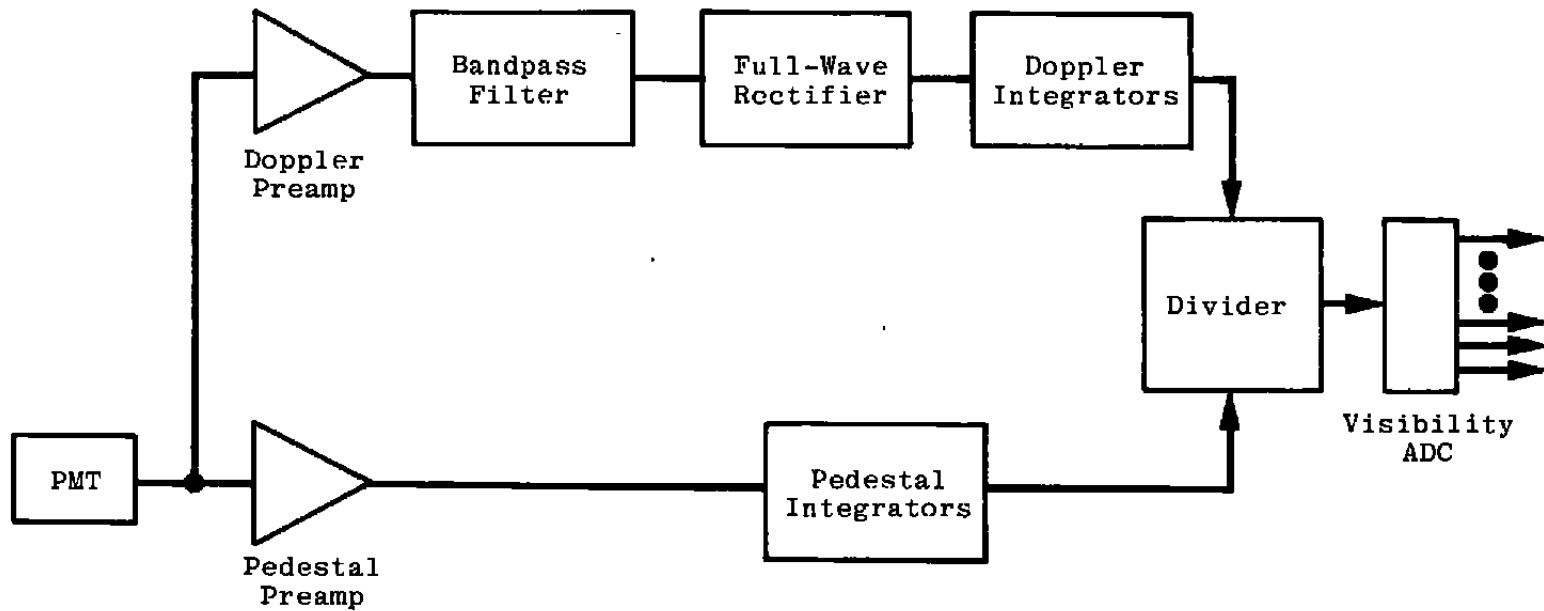
Figure 14. Electronics for commercial-PSI.

Light Collection Optics

Signal-Conditioning Electronics

Scattered Light

Λθ, Λφ

θ, φ

Scattering Particles

To Readout

Detector

Sampling Volume

Beam-Forming Optics
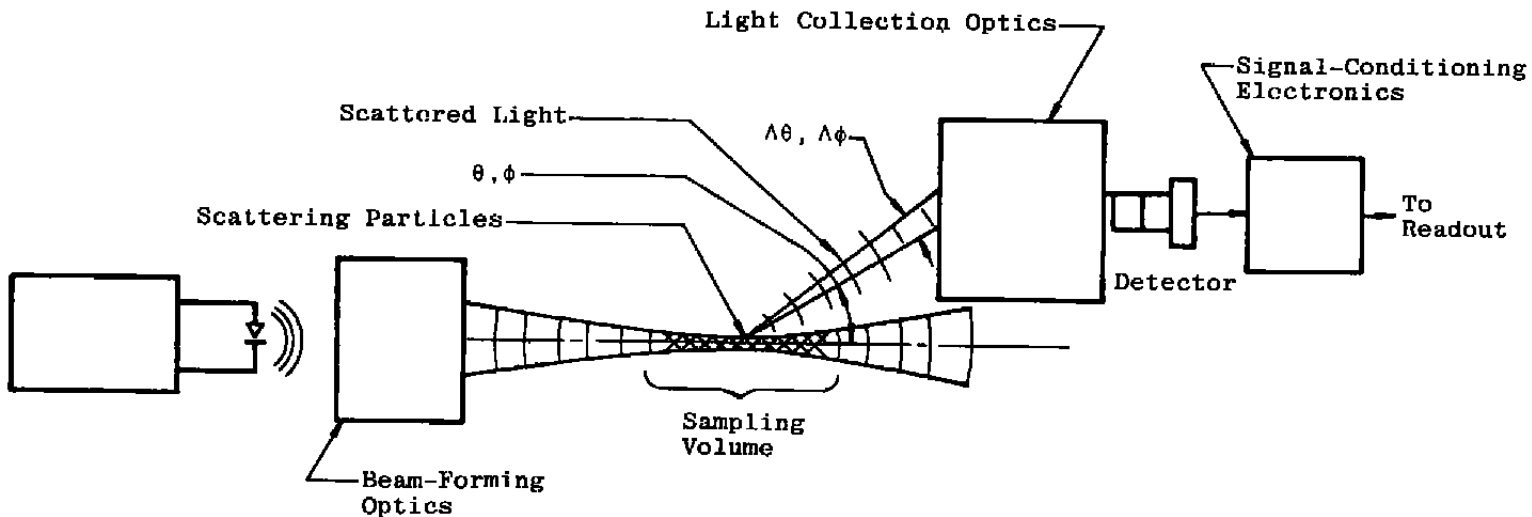
**Figure 15. Backscattering particle-sizing system.**
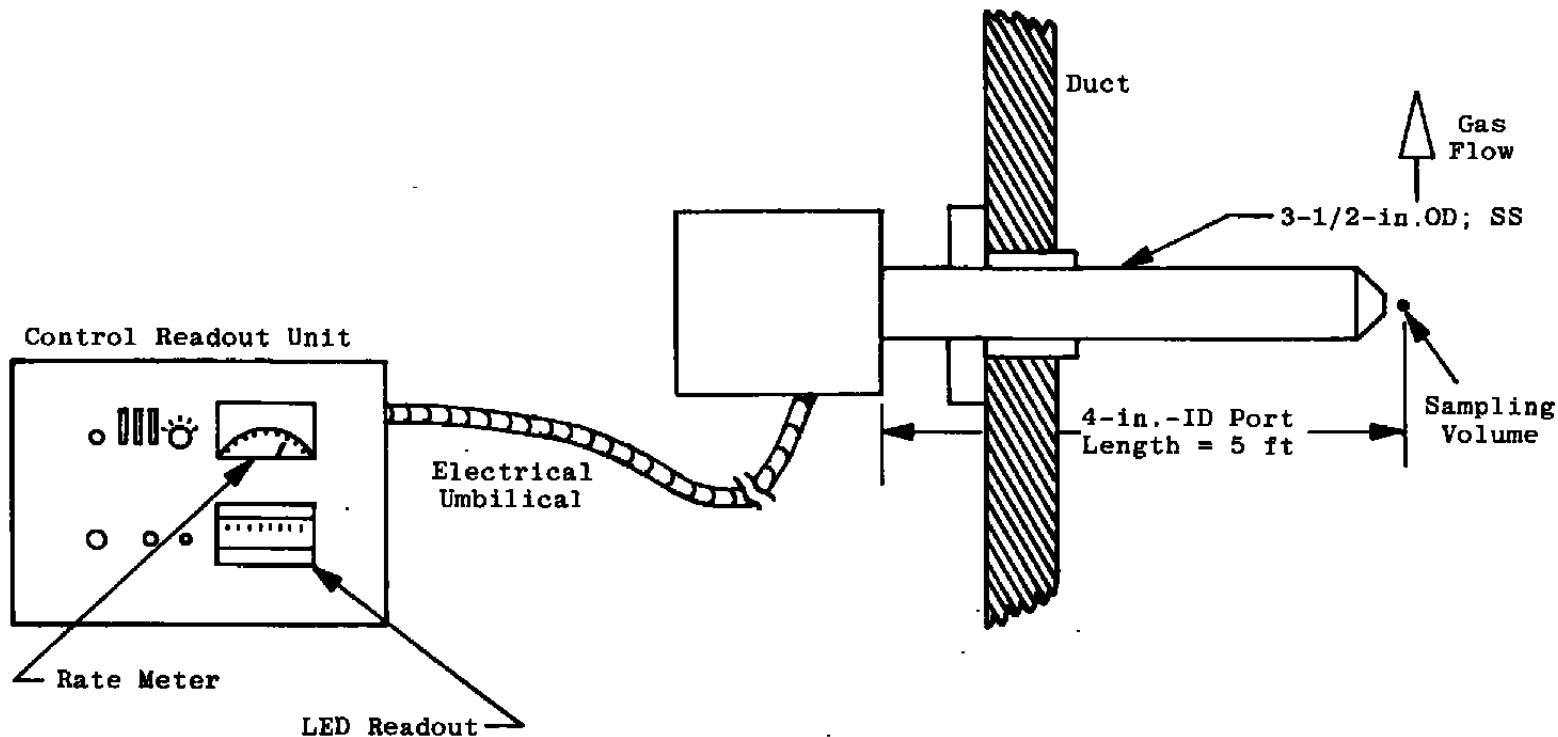
Figure 16. Typical installation of backscattering particle-sizing system.

Laser

Aperture

| Amplifier

A

Beamsplitter

Detector

B

Apertures

Laser
Pulser
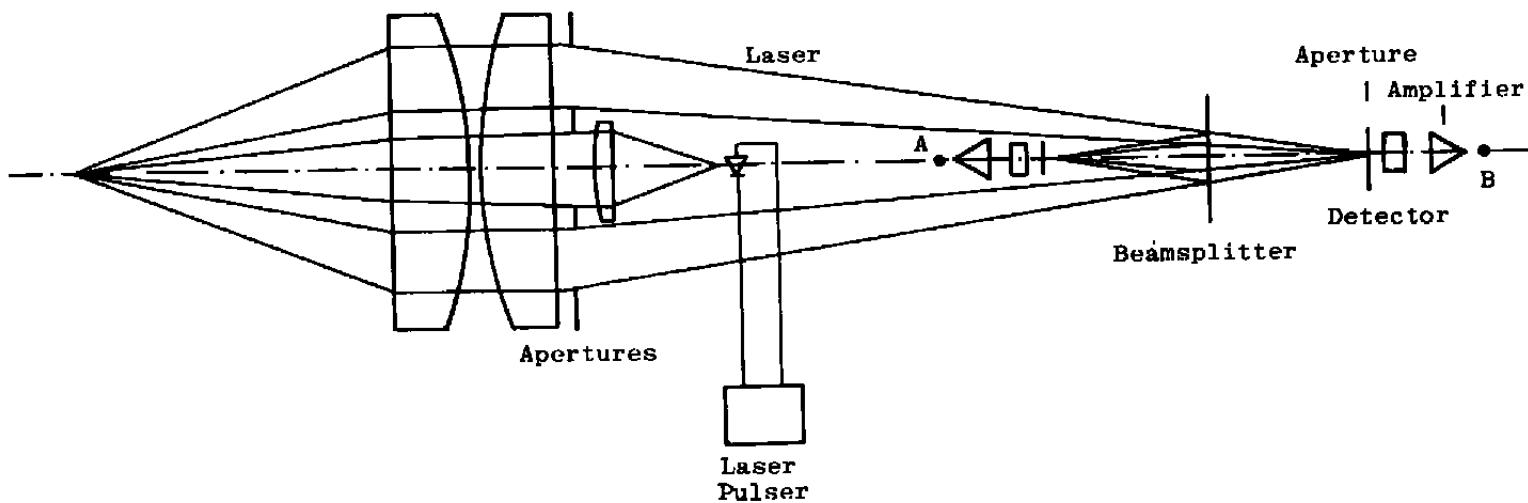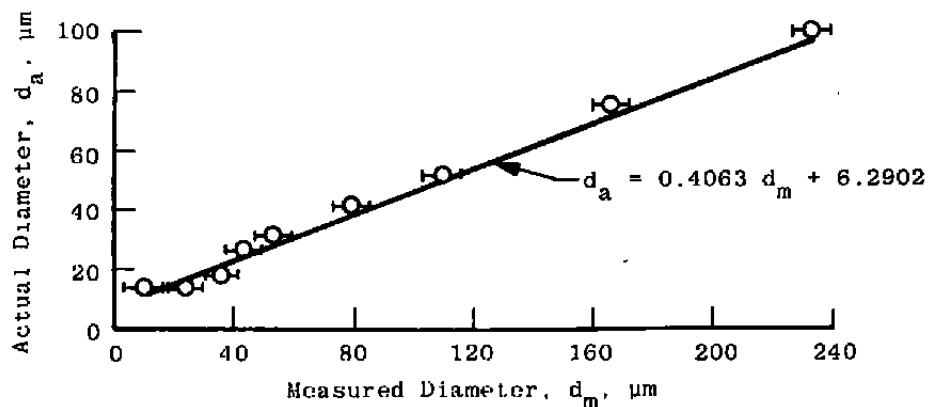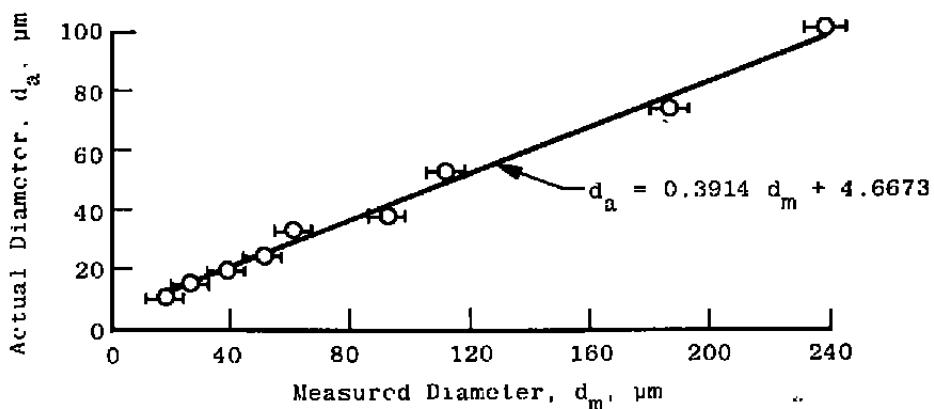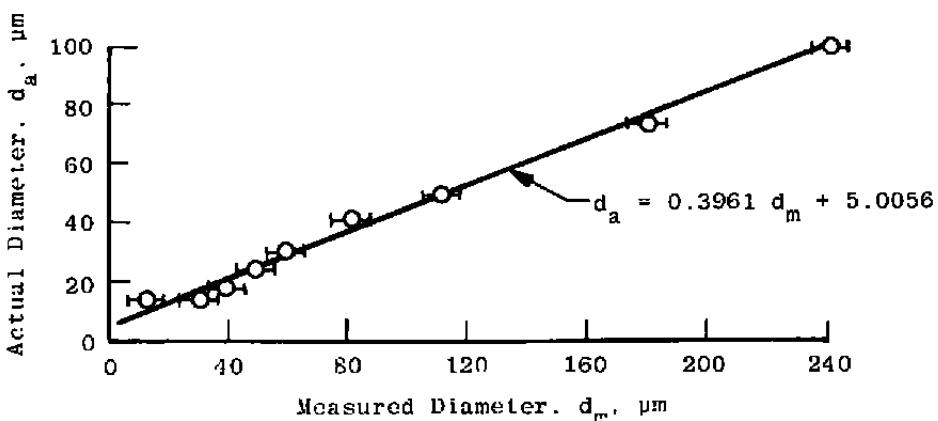
Figure 17.  Optical arrangement of backscattering
particle-sizing system.

a. Pretest calibration of holographic system.

$$d_a = 0.4063 \, d_m + 6.2902$$

b. Holographic calibration during testing.

$$d_a = 0.3914 \, d_m + 4.6673$$

c. Posttest calibration of holographic system
Figure 18. Holographic system calibration.

$$d_a = 0.3961 \, d_m + 5.0056$$
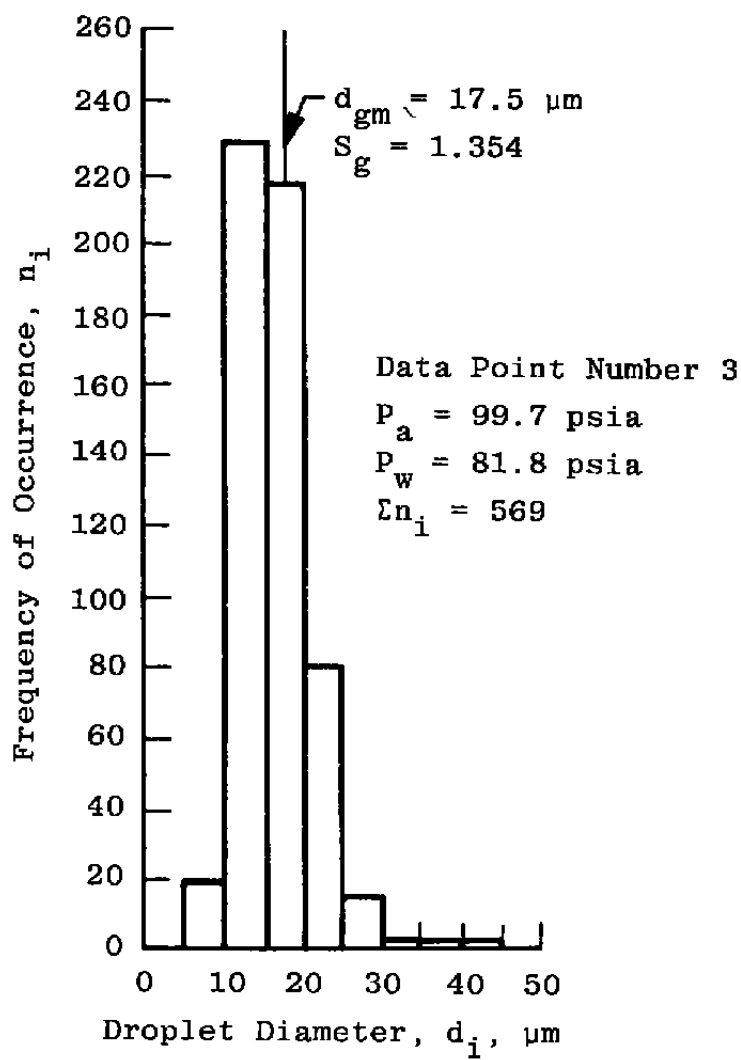
**Figure 19.** Typical histogram for research cell calibration (data point No. 3).
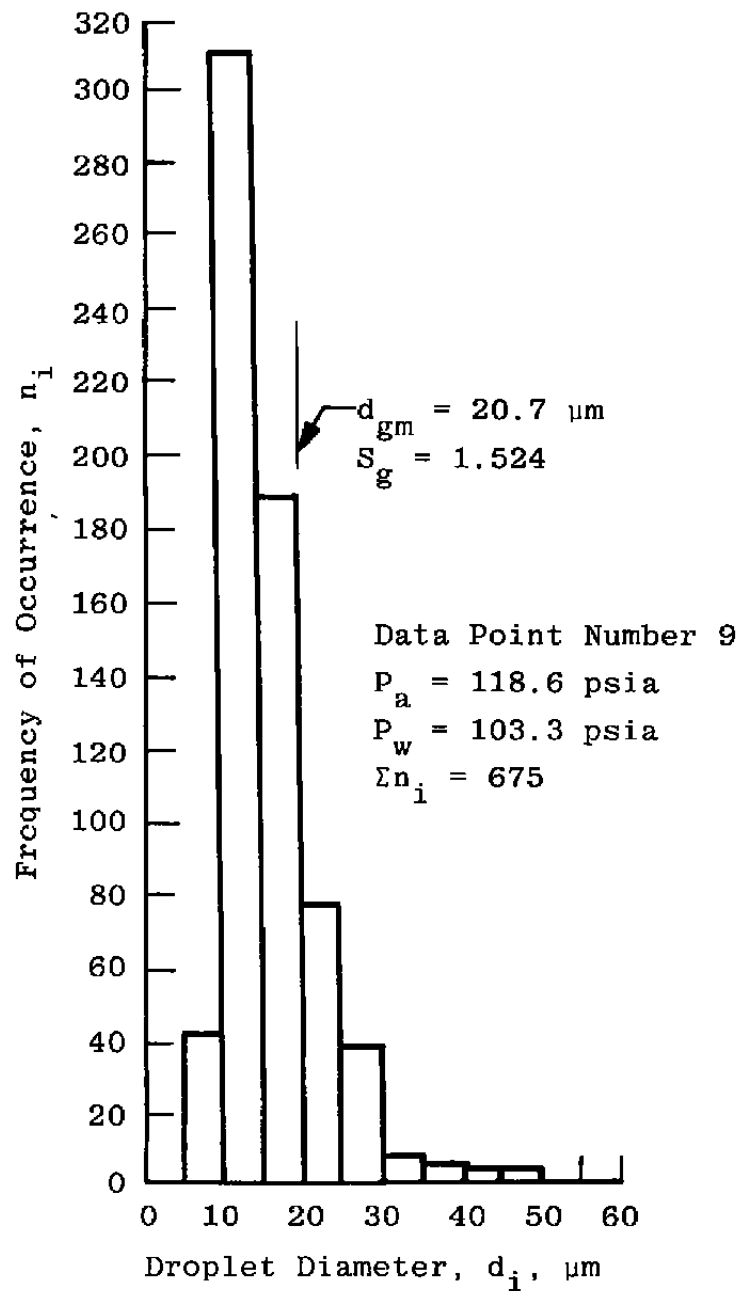
Figure 20.  Typical histogram for research cell calibration
(data point No. 9).
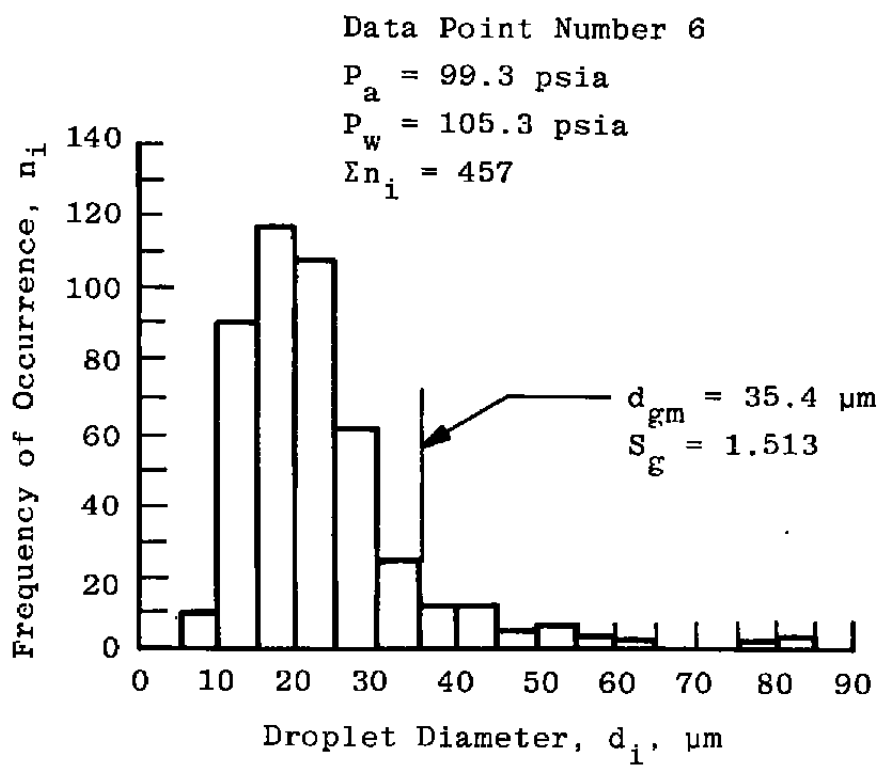
Figure 21. Typical histogram for research cell calibration (data point No. 6).
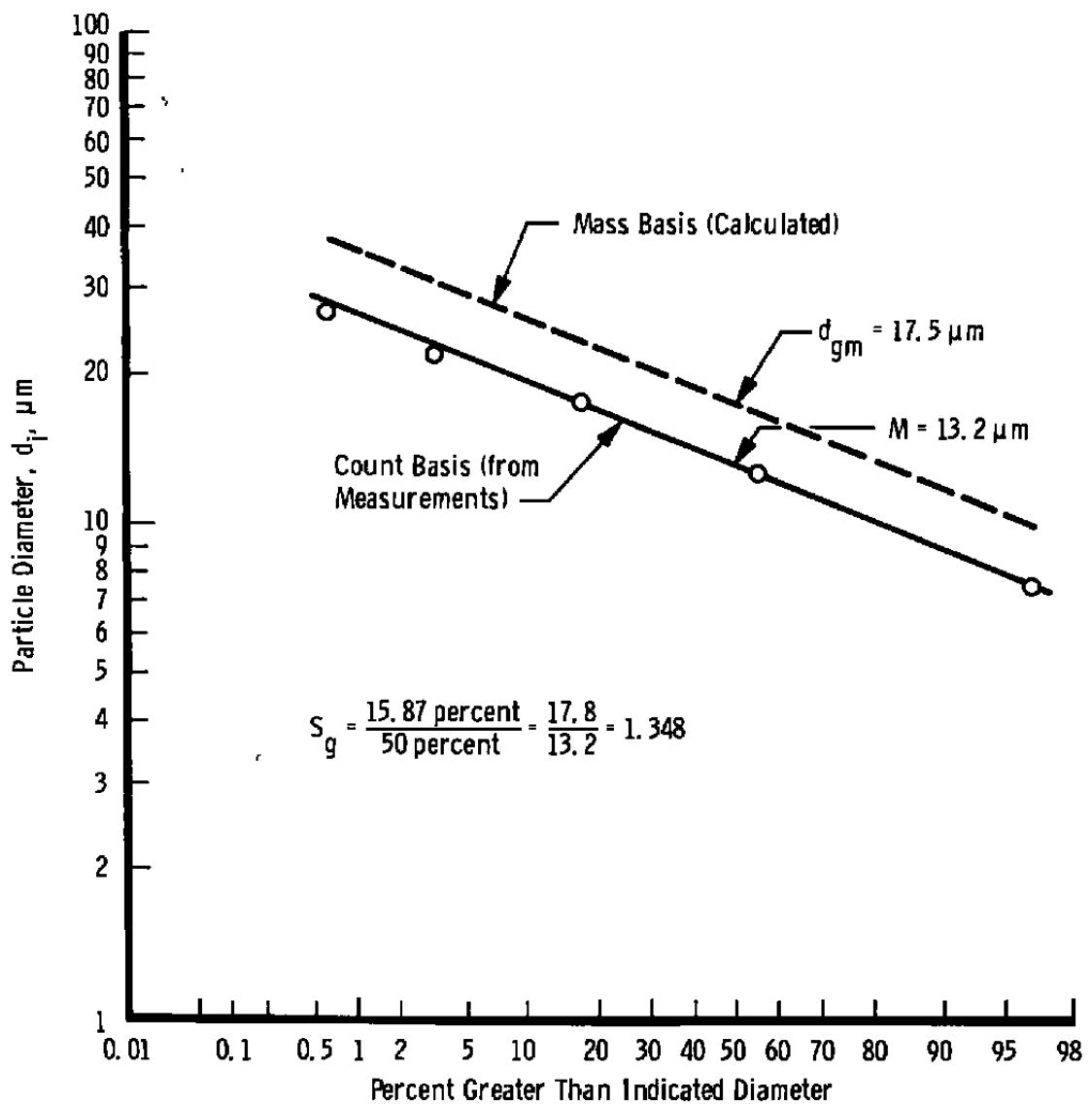
Figure 22. Log-probability plot of holographic data point No. 3.
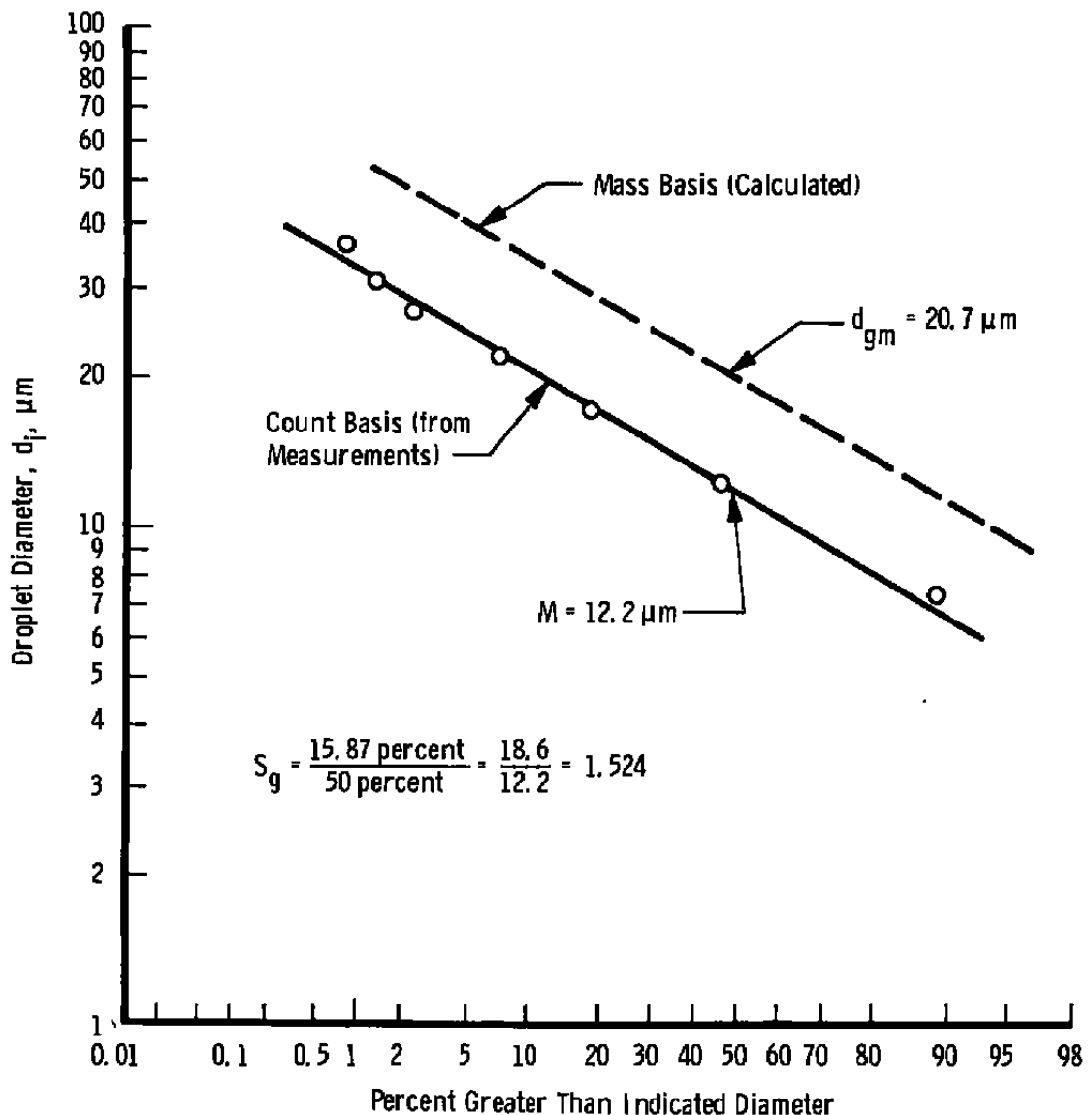
**Figure 23. Log-probability plot of holographic data point No. 9.**
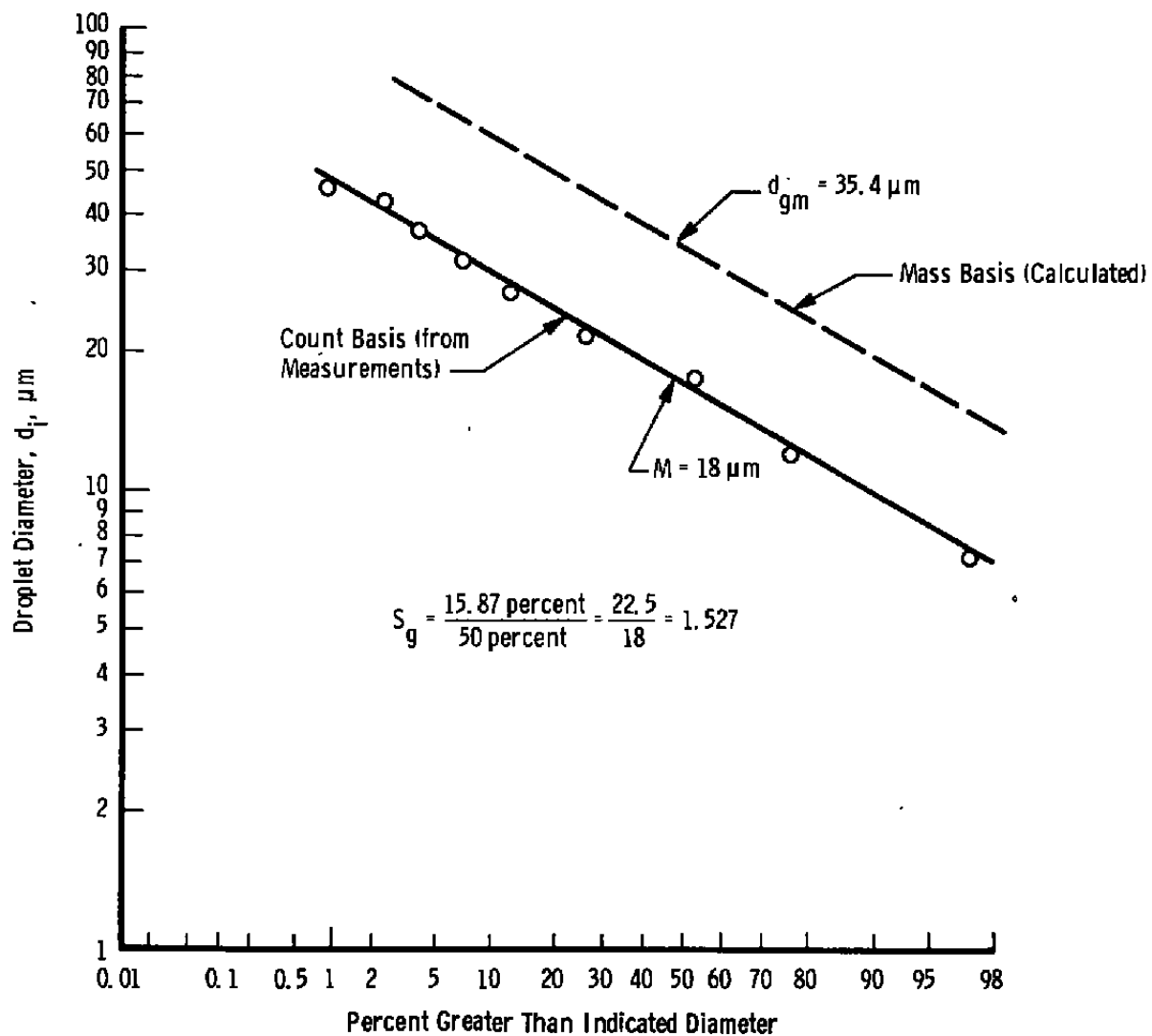
**Figure 24. Log-probability plot of holographic data point No. 6.**
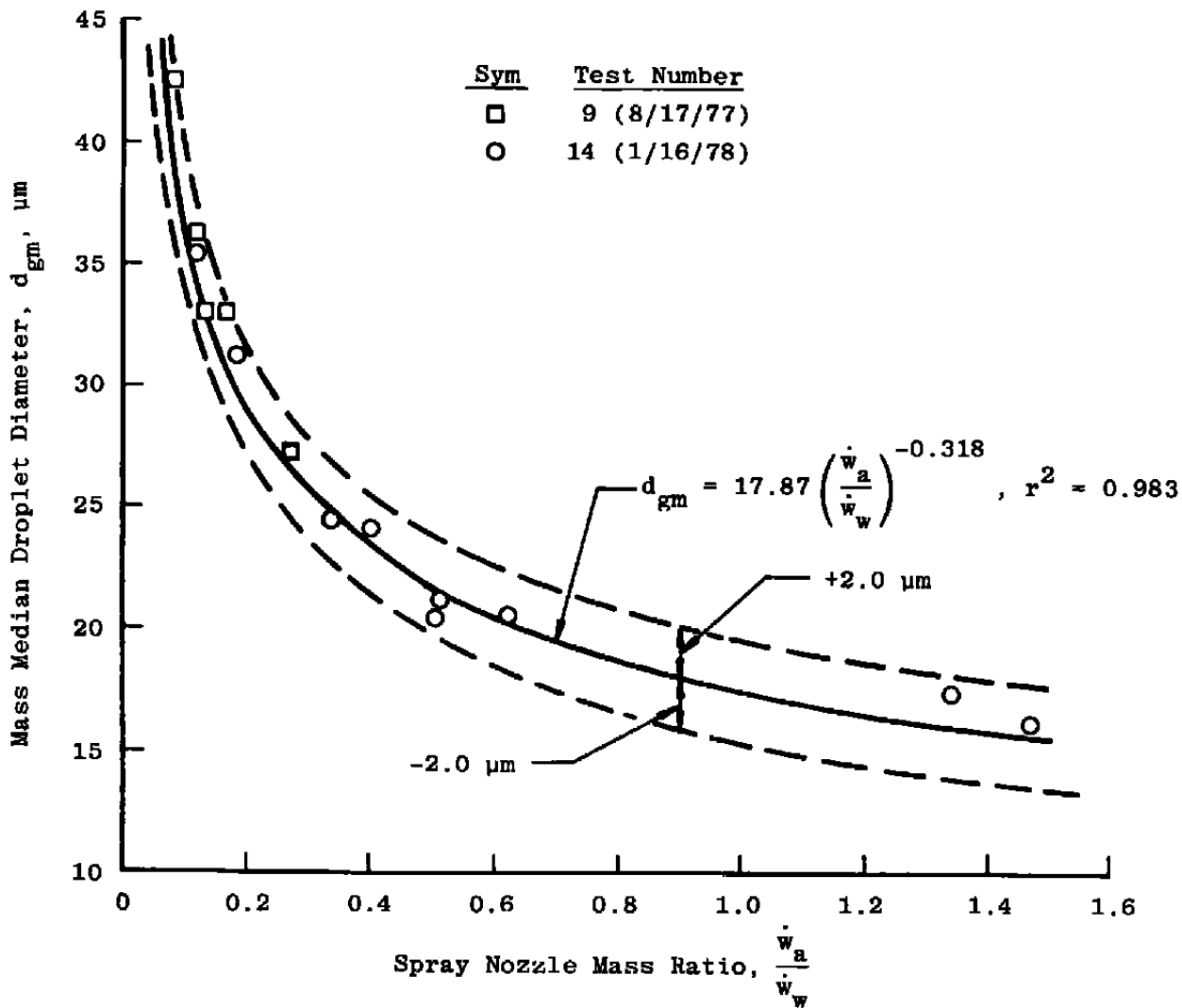
Figure 25. Spray nozzle calibration.
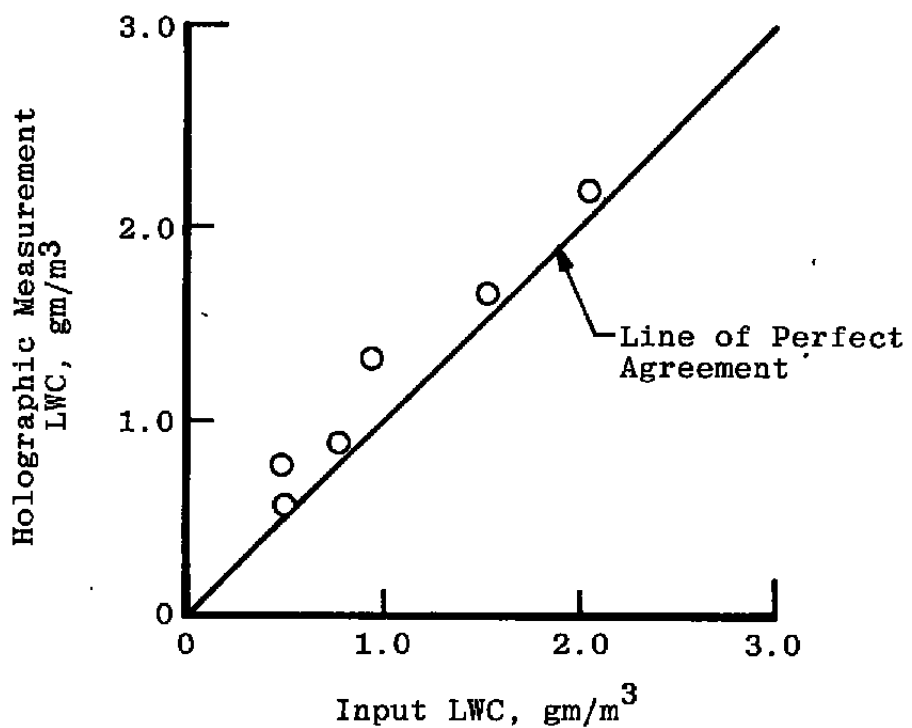
Figure 26. Calculated LWC vs input LWC.

a. Hologram number 4, 5.34 cm from film plane
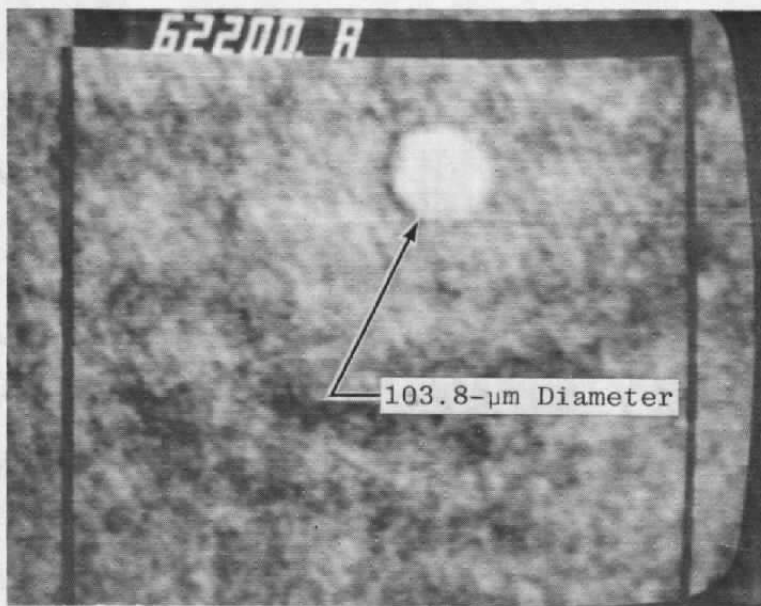


b. Hologram Number 18, 5.66 cm from film plane
Figure 27. Reconstructed holograms.

58
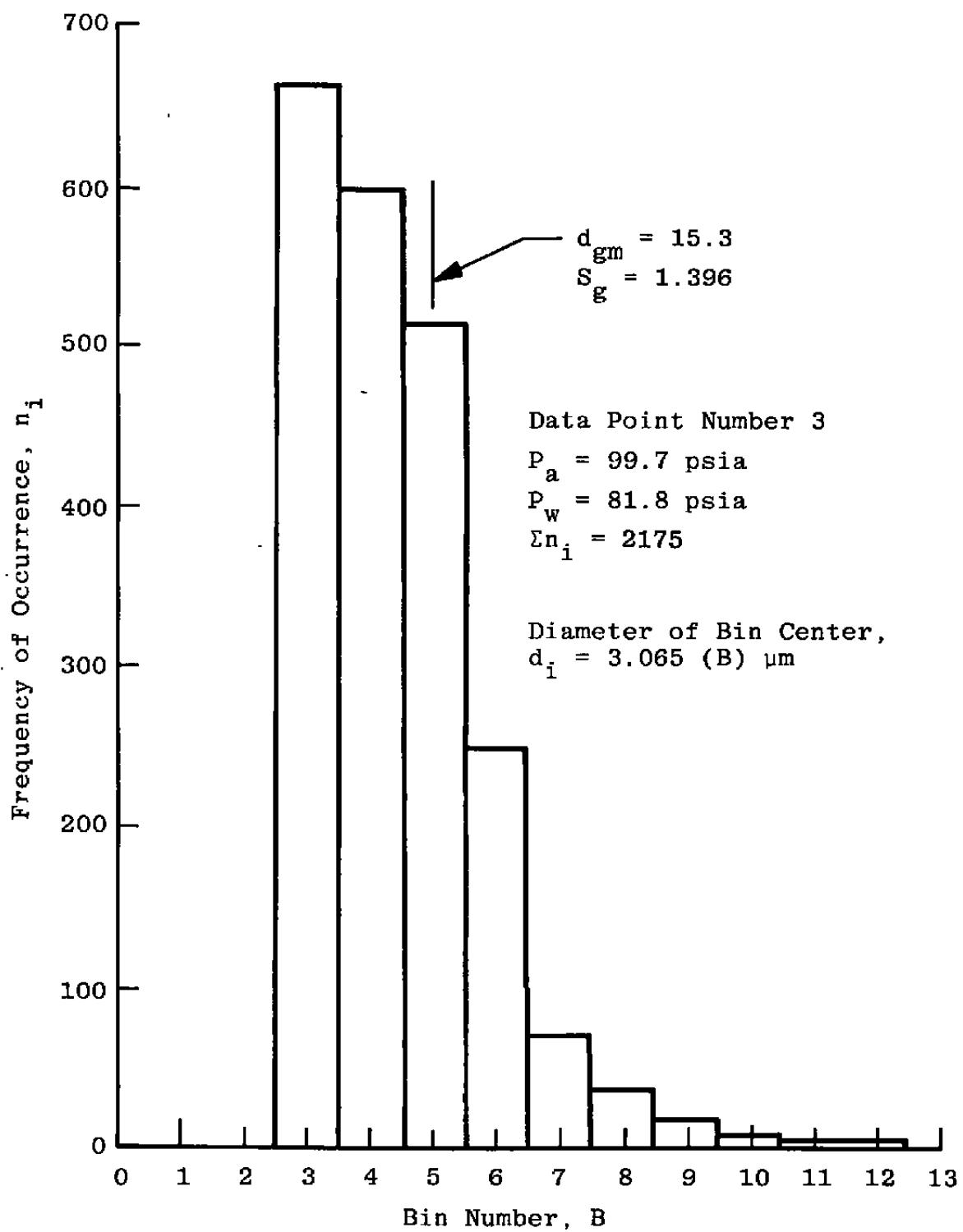
Figure 28. Typical FOS histogram (data point No. 3).
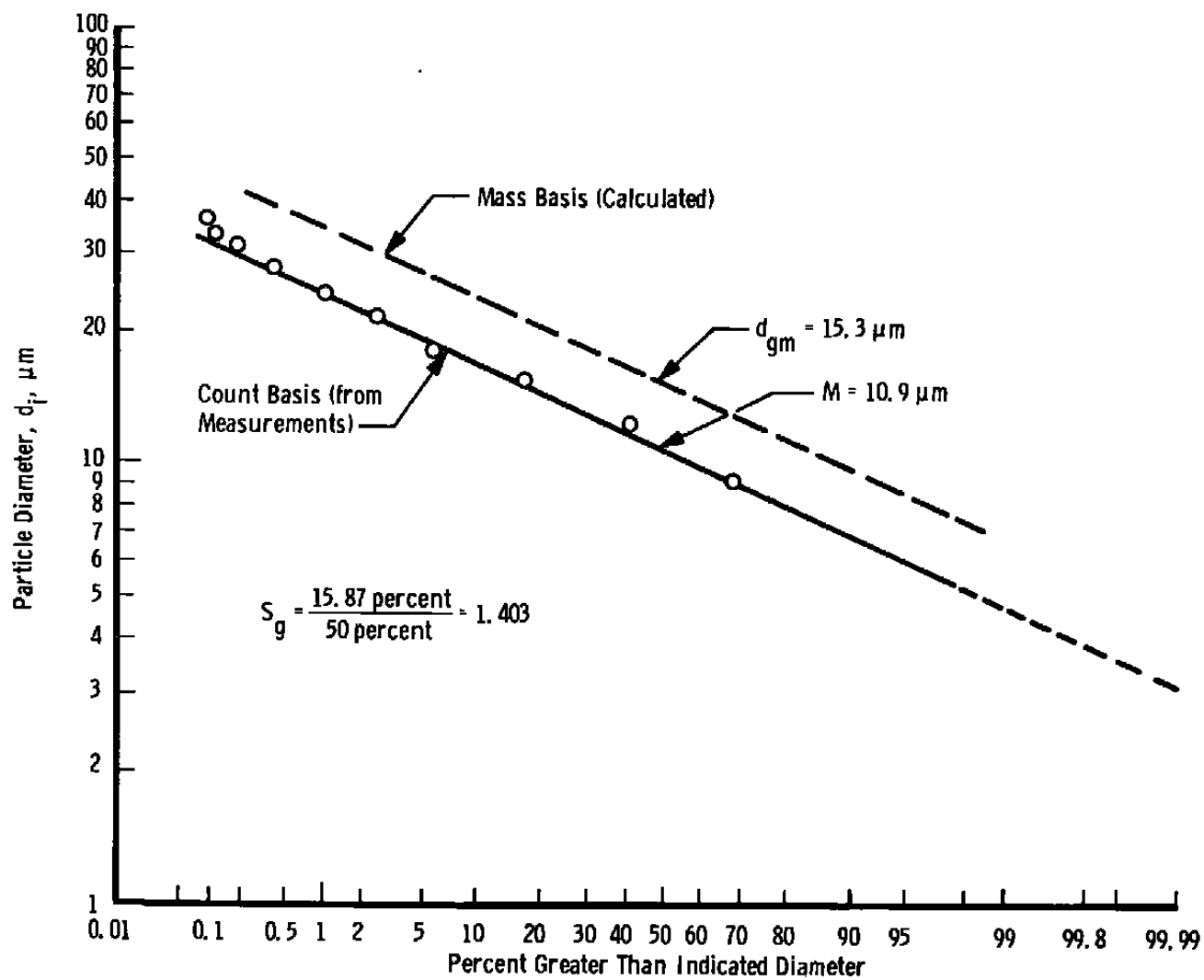
Figure 29.  Log-probability plot of FOS data point No. 3.
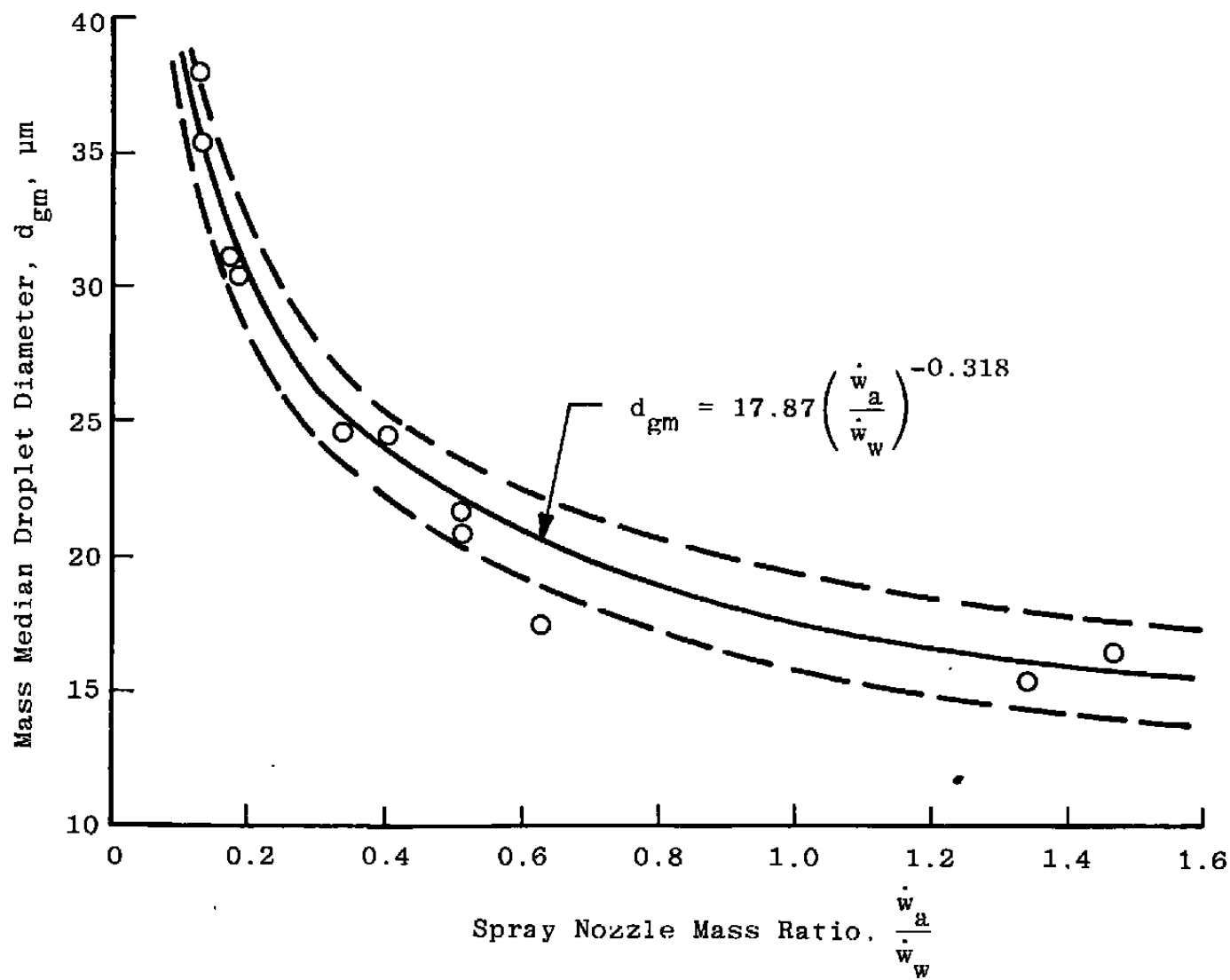
Figure 30. Comparison of FOS data with spray nozzle calibration.
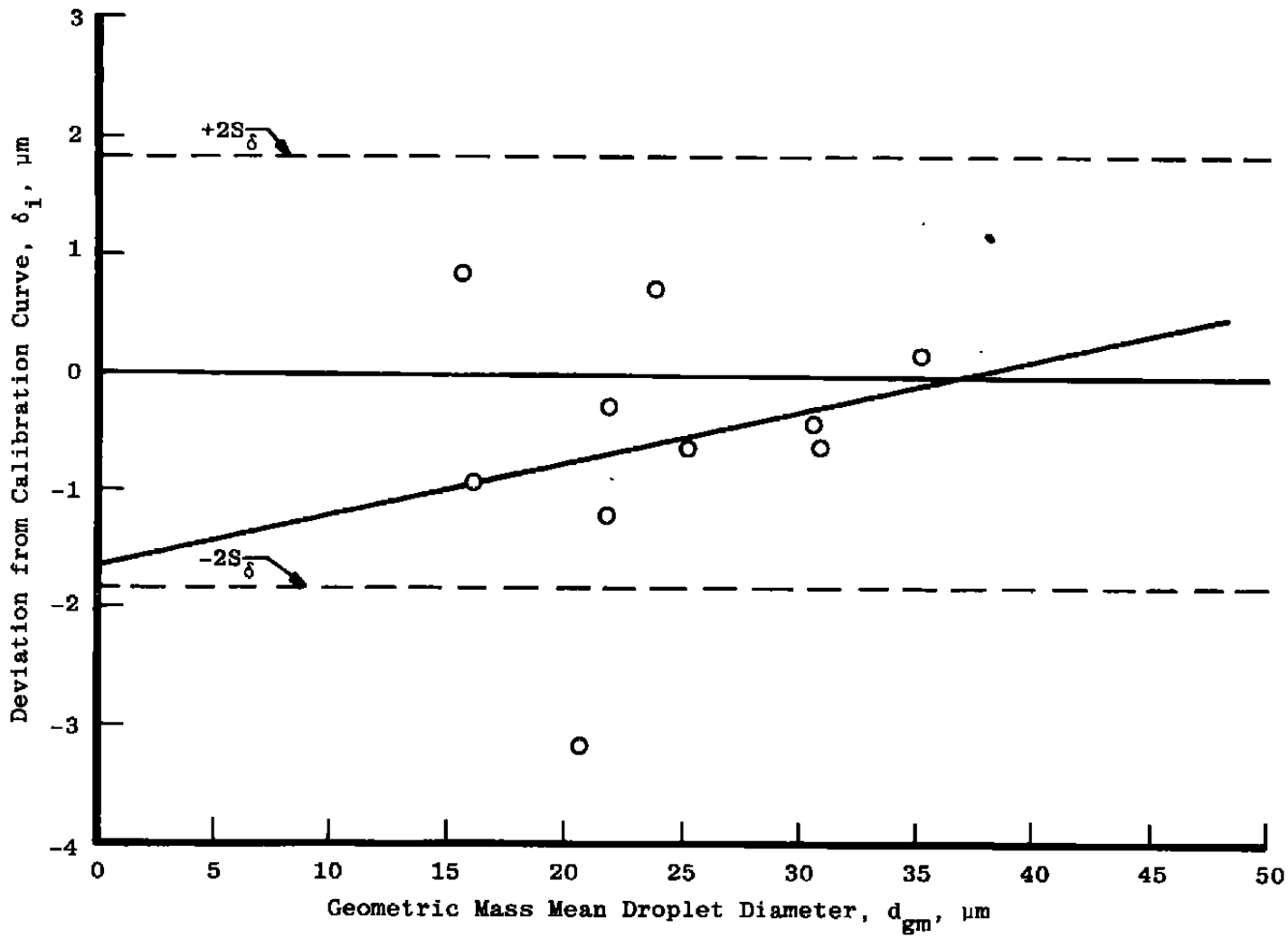
Figure 31.  Deviation of FOS data from holographic calibration data.

Data Point Number 3 (2/29/79)

$P_a$ = 99.7 psia

$P_w$ = 81.8 psia

$\Sigma f_i$ = 35.2 Particles/cc/µm

$d_{gm}$ = 27.5 µm

$S_\delta$ = 1.326

Frequency, $f_i$, Particles/cc/µm

Particle Diameter, µm
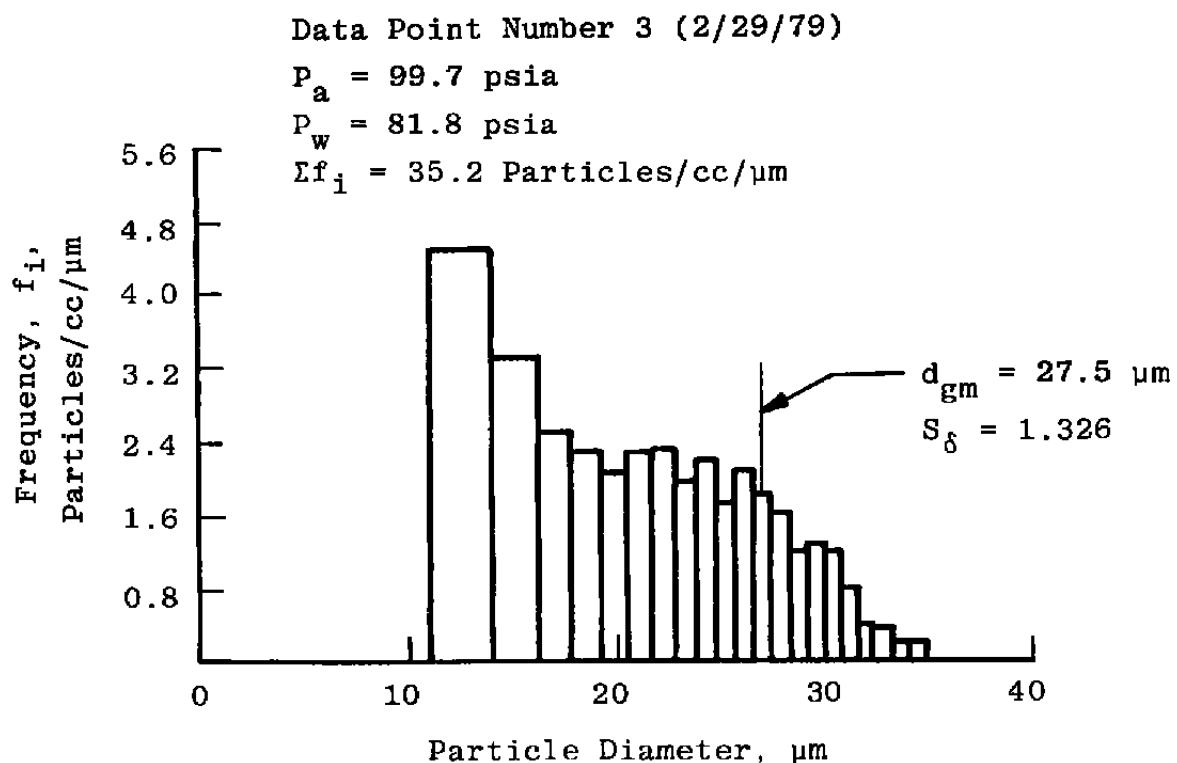
Figure 32. Typical histogram for AEDC-developed PSI.
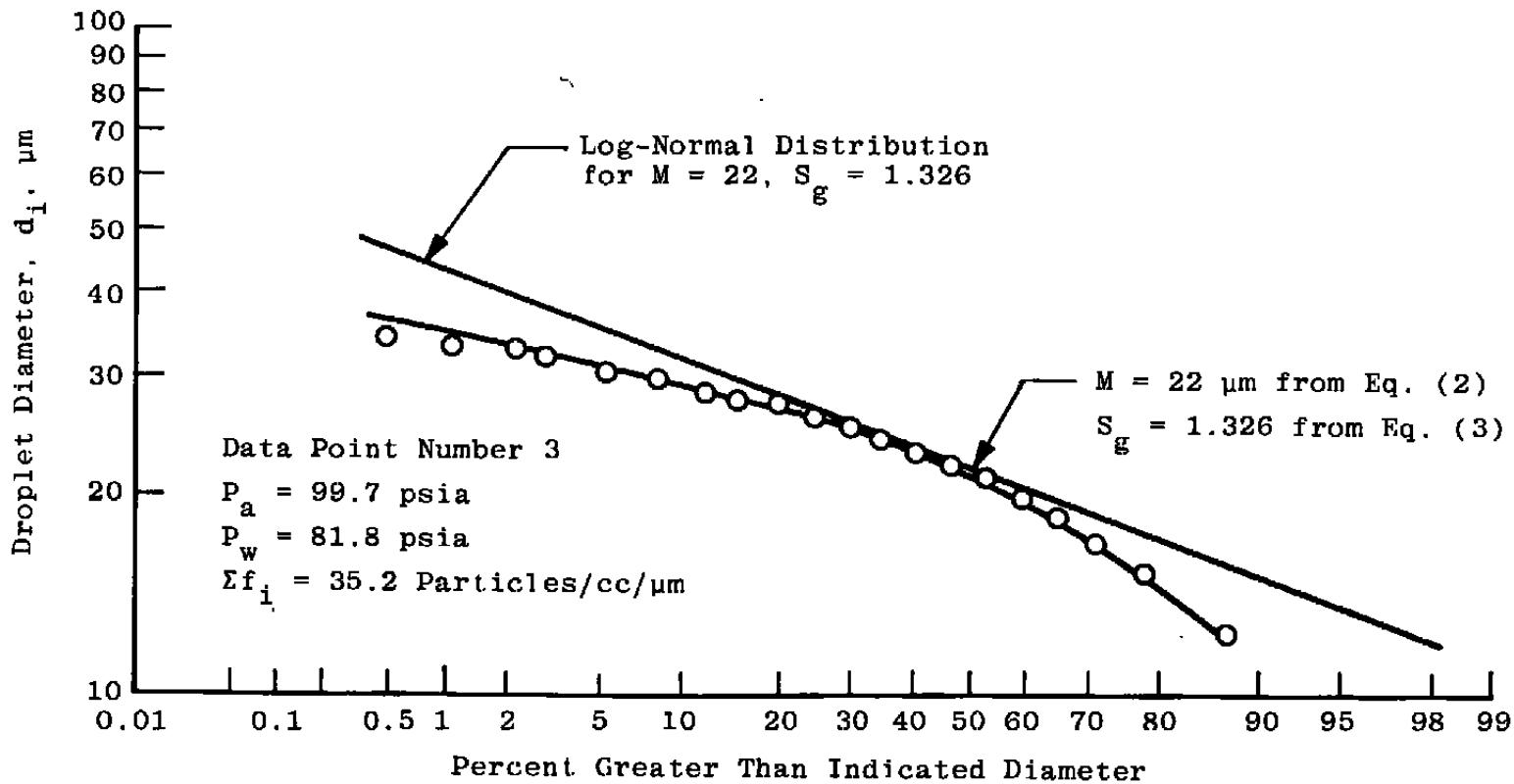
**Figure 33. Typical log-probability plot for AEDC-PSI.**
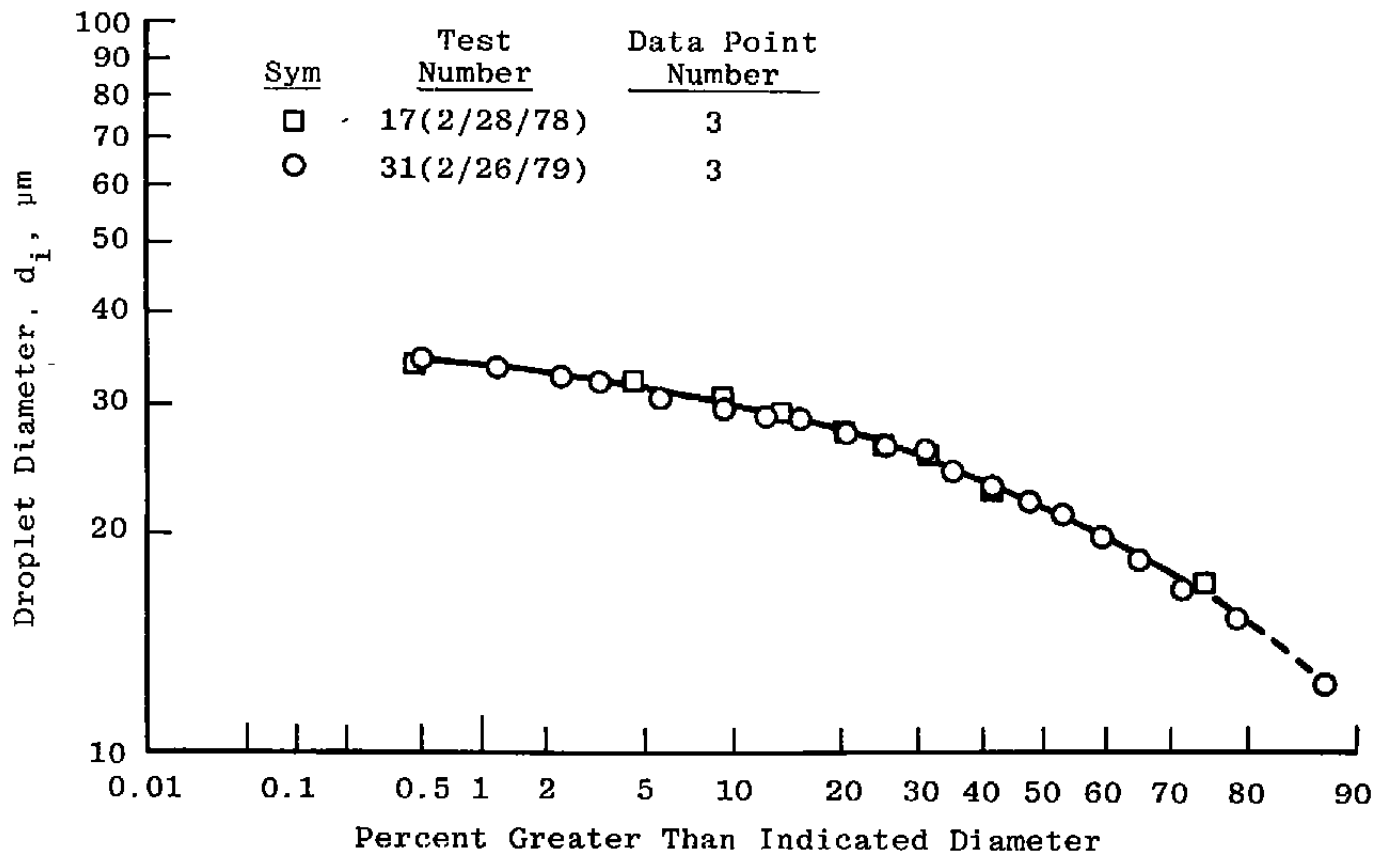
Figure 34. Comparison of log-probability plots.
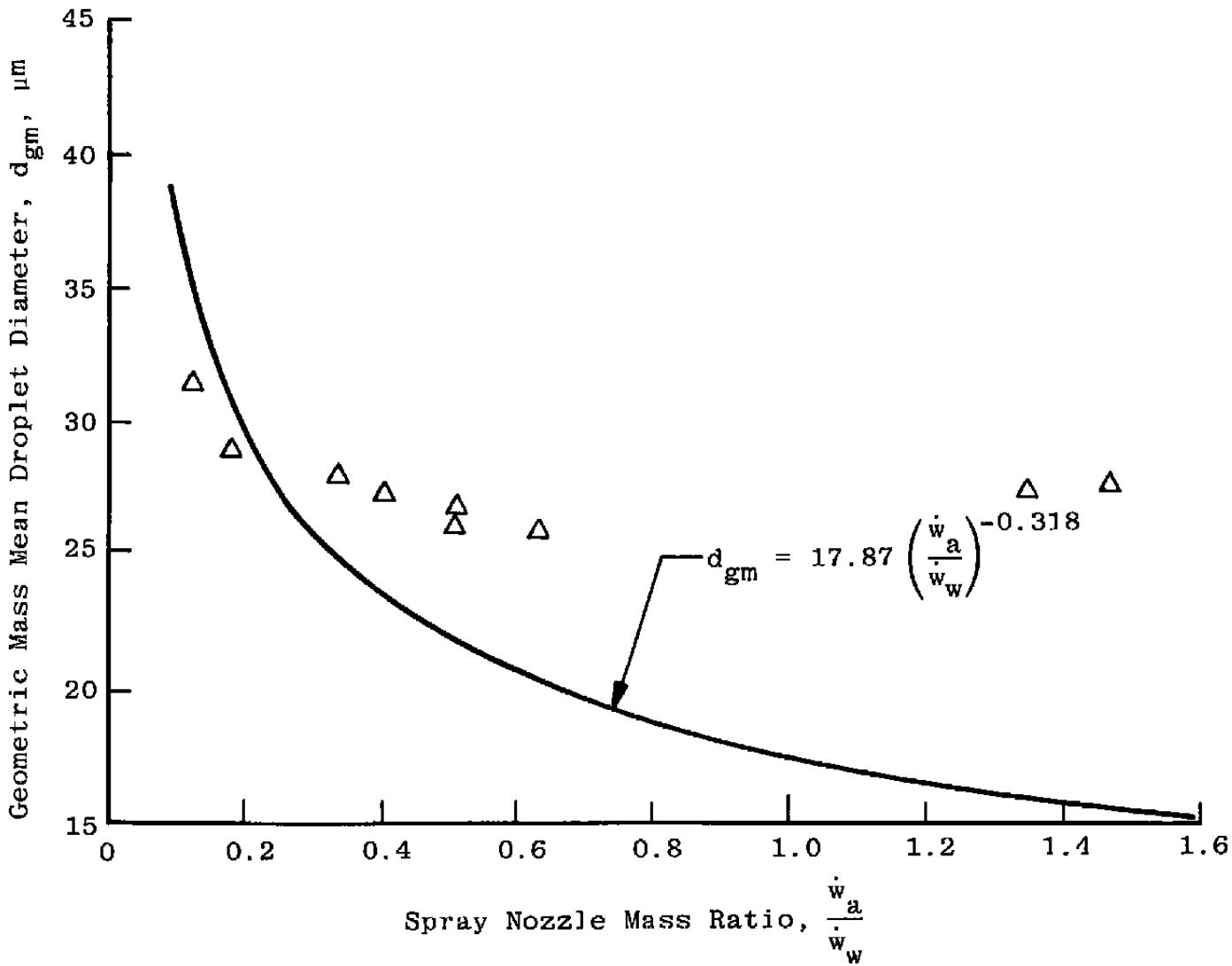
Figure 35.  Comparison of AEDC-PSI data with spray nozzle calibration.

The curve in the figure is labeled:

$$d_{gm} = 17.87 \left( \frac{\dot{w}_a}{\dot{w}_w} \right)^{-0.318}$$

Y-axis: Geometric Mass Mean Droplet Diameter, $d_{gm}$, $\mu m$

X-axis: Spray Nozzle Mass Ratio, $\dfrac{\dot{w}_a}{\dot{w}_w}$
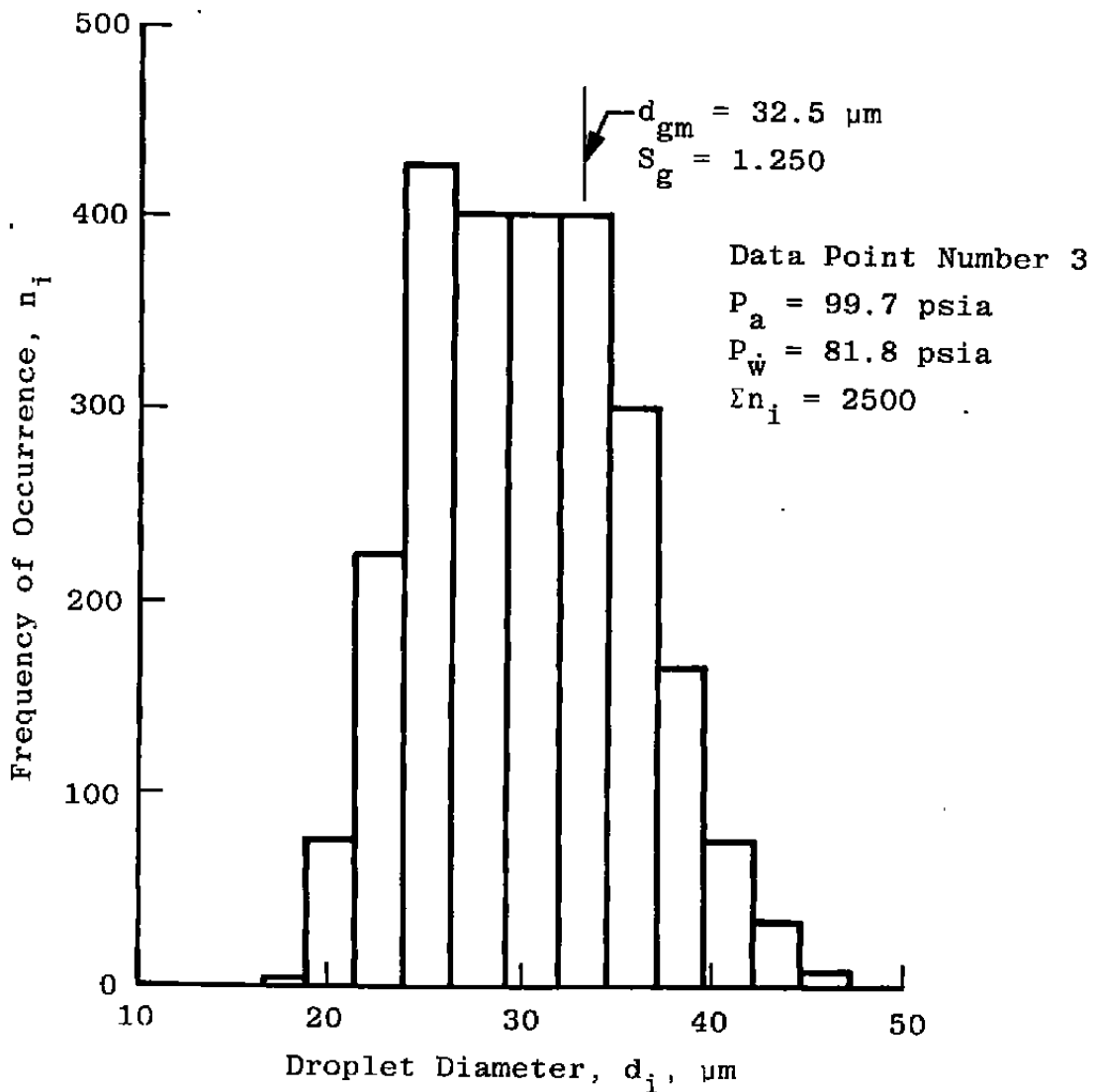
Figure 36. Typical histogram for commercial-PSI.
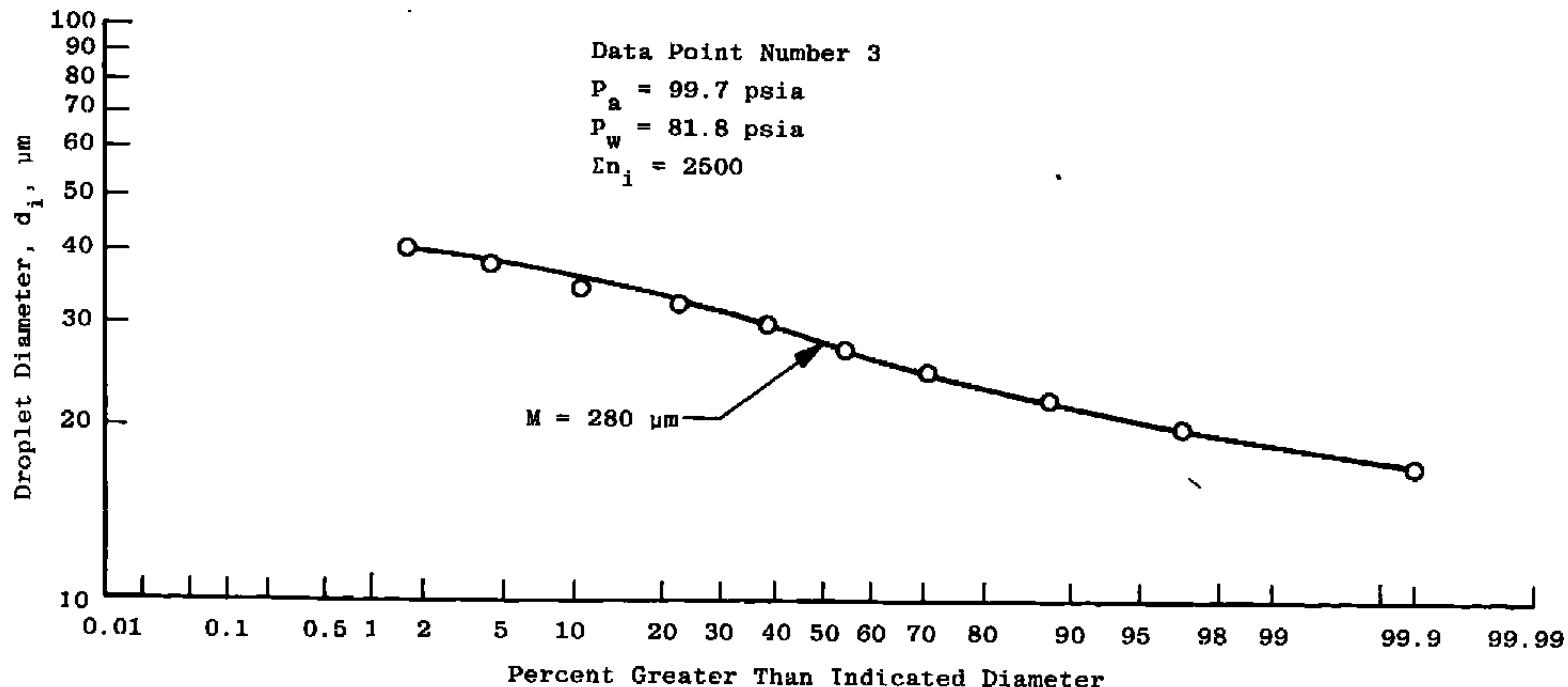
Figure 37.  Typical log-probability plot for commercial-PSI.
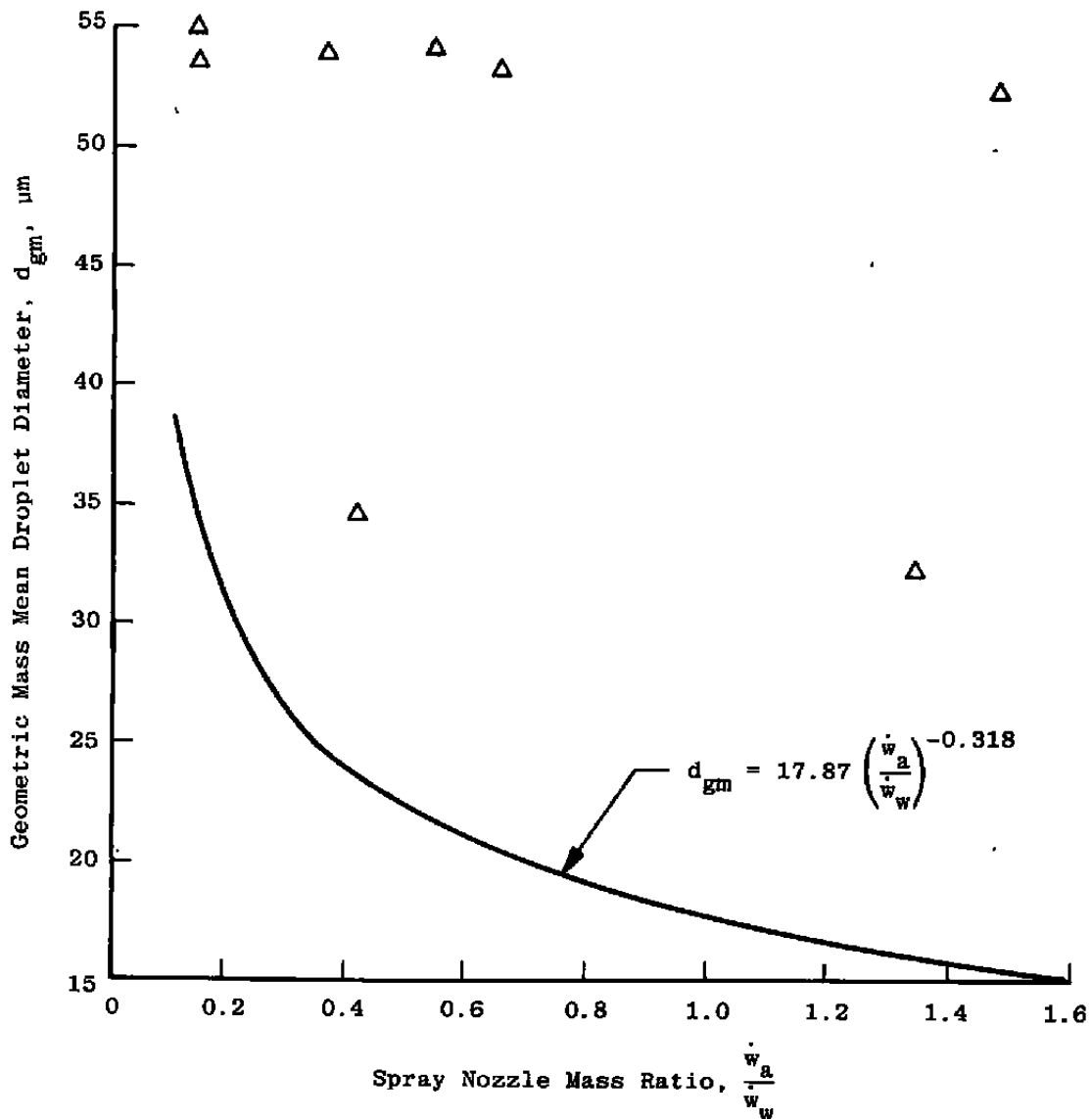
Figure 38. Comparison of commercial-PSI data with spray nozzle calibration.
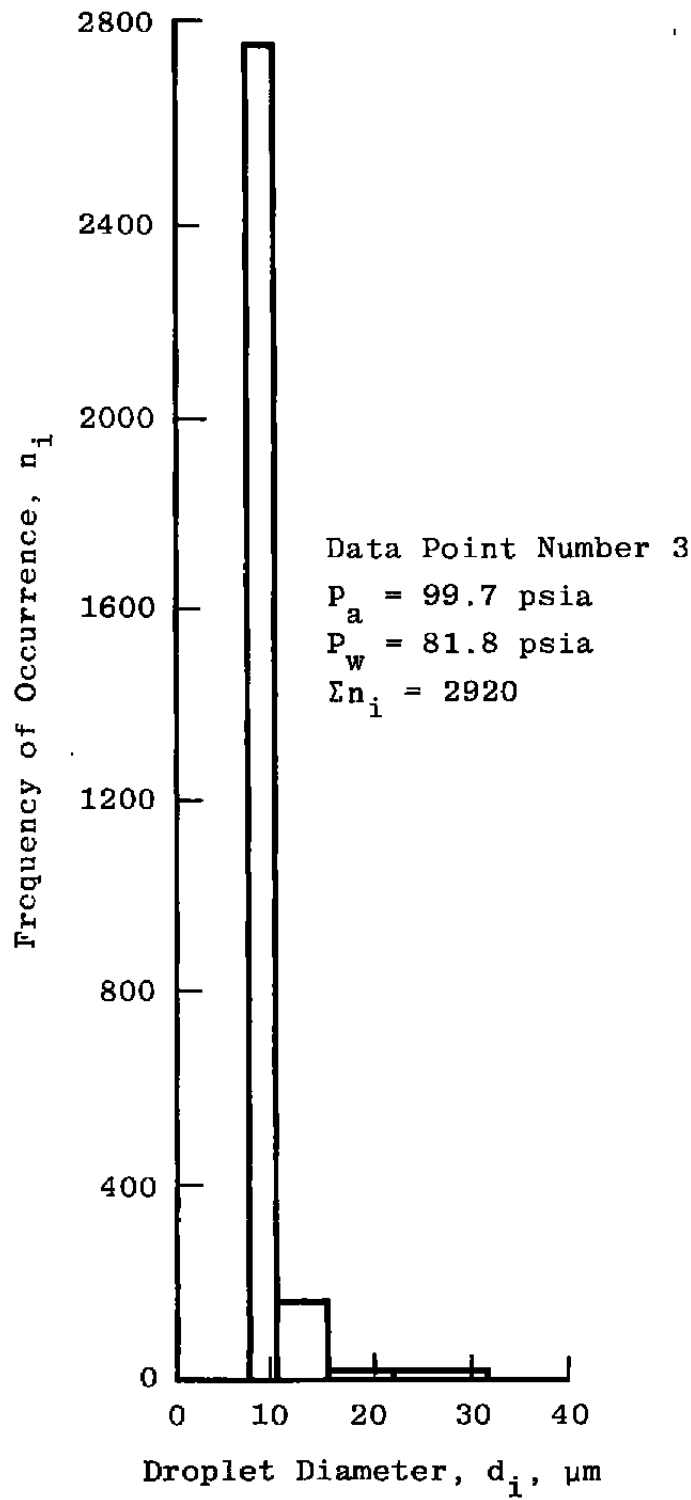
Figure 39. Typical histogram for BPS.
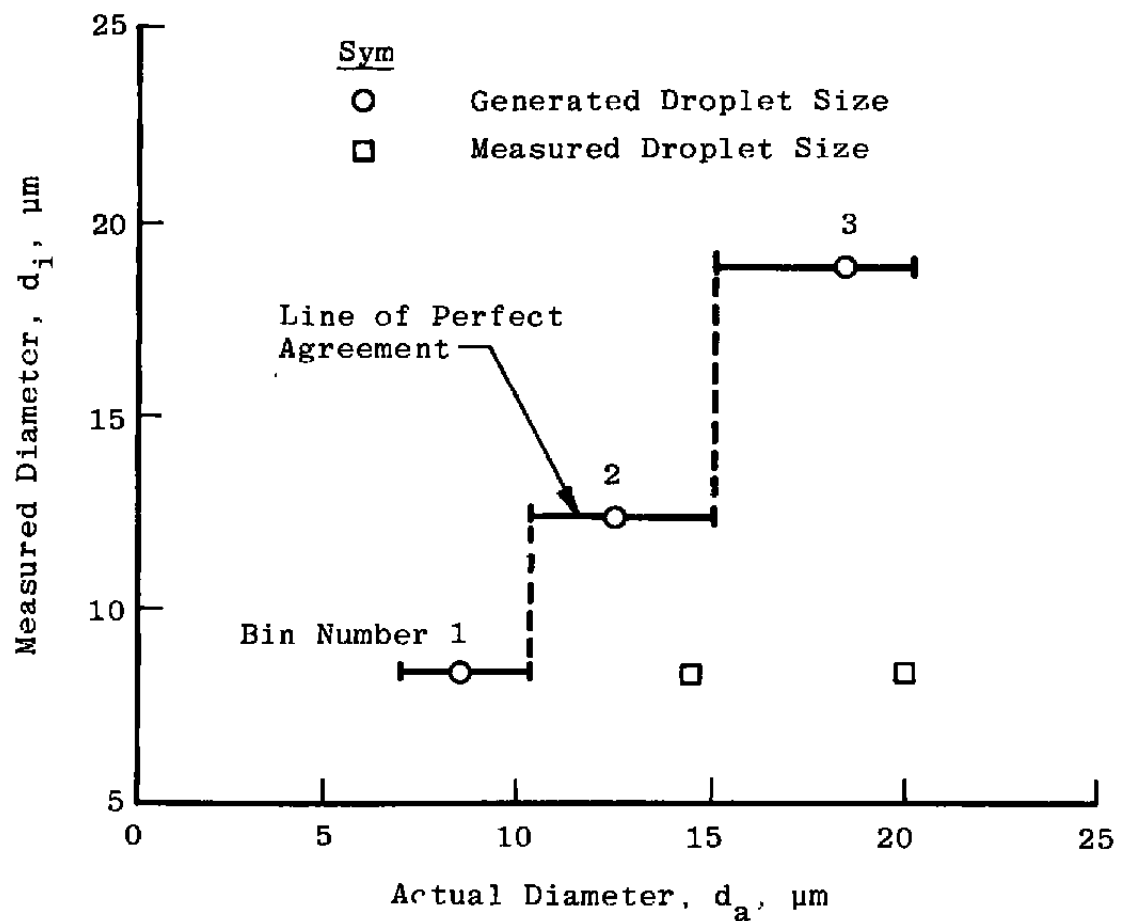
Figure 40. Measured vs actual droplet diameters for BPS.

Table 1. Icing Research Cell Performance Capability

| Conditions | Level | |
|---|---|---|
| | Maximum | Minimum |
| Pressure Altitude | 80,000 ft | Sea Level |
| Inlet Air Pressure | 40 psi | --- |
| Inlet Air Temperature | 185°F | -20°F |
| Cell Mach Number | 0.7 | --- |
| Airflow Rate | 30 lbm/sec | --- |
| Atomizing Air Pressure | 175 psia | Atmospheric |
| Atomizing Air Temperature | 200°F | 70°F |
| Demineralized Water Pressure | 290 psia | Atmospheric |
| Demineralized Water Temperature | 200°F | Atmospheric |
| Demineralized Water Flow Rate | 12 gal/hr | 0 gal/hr |

# Table 2. Test Conditions for Experimental Program

| Data Point Number (1/16/78) | Inlet Air Conditions | | | Spray Nozzle Conditions | | | | | |
|---|---|---|---|---|---|---|---|---|---|
| | Total Temp, °F | Free-Stream Bulk Vel, fps | Alt, ft | Air | | | Water | | |
| | | | | Press., psia | Temp, °F | Flow, cfm | Press., psia | Temp, °F | Flow gal/min |
| 1 | 37 | 330 | 14,500 | 112.46 | 57 | 2.70 | 91.67 | 67 | 0.0462 |
| 2 | 38 | 330 | 14,500 | 100.66 | 60 | 2.30 | 89.80 | 67 | 0.1083 |
| 3 | 38 | 340 | 14,600 | 99.72 | 58 | 2.06 | 81.80 | 67 | 0.0440 |
| 4 | 38 | 343 | 14,600 | 49.90 | 67 | 1.55 | 46.03 | 67 | 0.0652 |
| 5 | 38 | 350 | 14,600 | 25.49 | 69 | 0.75 | 41.64 | 67 | 0.1874 |
| 6 | 39 | 335 | 14,600 | 99.33 | 65 | 0.93 | 105.31 | 67 | 0.1872 |
| 7 | 38 | 335 | 14,600 | 100.03 | 67 | 2.31 | 89.75 | 67 | 0.1070 |
| 8 | 38 | 341 | 14.600 | 125.06 | 60 | 2.31 | 125.89 | 67 | 0.1861 |
| 9 | 38 | 339 | 14,600 | 118.58 | 58 | 2.55 | 103.30 | 67 | 0.1068 |
| 10 | 38 | 340 | 14,500 | 28.62 | 68 | 0.56 | 63.98 | 80 | 0.1897 |
| 11 | 38 | 343 | 14,500 | 28.64 | 68 | 1.00 | 50.63 | 80 | 0.1175 |
| 12 | 38 | 339 | 14,500 | 48.21 | 68 | 1.82 | 89.33 | 72 | 0.1121 |
| 13 | 38 | 340 | 14,500 | 20.36 | 68 | 1.07 | 30.95 | 80 | 0.0977 |
| 14 | 38 | 344 | 14,600 | 20.33 | 68 | 0.72 | 28.18 | 78 | 0.0599 |

73

Table 3. Parameter Measurement Uncertainty

| Parameter | Range | Bias (%), B | Precision Index (%), S | Degrees of Freedom | Uncertainty (%), $\pm(B + t_{95} S)$ |
|---|---|---|---|---|---|
| Airflow | <30 lbm/sec | 0.12 | 0.17 | >30 | 0.45 |
| Total Temperature | 460°R | 0.4 | 0.20 | >30 | 1.40 |
| Total Pressure | 5 to 30 psia | 0.4 | 0.30 | >30 | 1.0 |
| Water Flow | 1-11.5 gal/hr | 0.4 | 0.30 | >30 | 1.0 |

Table 4. Holocamera Results

| Data Point Number | Analytical Evaluation | | | Graphical Evaluation | |
|---|---|---|---|---|---|
| | Eq. (2), M, μm | Eq. (3), $S_g$ | Eq. (4), dgm, μm | M, μm | $S_g$ |
| 1 | 12.6 | 1.325 | 16.0 | 12.5 | 1.360 |
| 2 | 14.9 | 1.387 | 20.5 | 15.0 | 1.410 |
| 3 | 13.3 | 1.354 | 17.5 | 13.2 | 1.325 |
| 4 | 18.1 | 1.530 | 31.3 | 18.0 | 1.525 |
| 5 | 15.5 | 1.471 | 24.2 | 15.7 | 1.490 |
| 6 | 21.1 | 1.513 | 35.4 | 21.0 | 1.520 |
| 7 | 14.2 | 1.439 | 21.1 | 14.0 | 1.421 |
| 8 | 14.3 | 1.531 | 24.6 | 14.2 | 1.501 |
| 9 | 14.5 | 1.403 | 20.5 | 14.5 | 1.462 |
| 10 | 27.5 | 1.465 | 42.6 | 27.3 | 1.400 |
| 11 | 24.3 | 1.381 | 33.2 | 24.0 | 1.362 |
| 12 | 18.1 | 1.448 | 27.3 | 18.0 | 1.450 |
| 13 | 12.9 | 1.801 | 36.4 | 13.0 | 1.855 |
| 14 | 12.7 | 1.761 | 33.1 | 12.5 | 1.801 |

# APPENDIX A
# METHODS OF CALCULATION FOR EXPERIMENTAL DATA

The general methods and equations used to compute the parameters presented in this report are given below. Where applicable, the arithmetic average of the pressure and temperature was used.

## A-1.0 AIRFLOW

### A-1.1 VENTURI AIRFLOW

The primary airflows were calculated from the equation

$$W = 0.5318 \frac{C_f C_t C_v P_s A}{\sqrt{T_t}} \tag{A-1}$$

where $C_t = f(T_T, P_T, P_S)$, $C_f = f(T_T, P_T)$, and $C_v = f(P_S, A)$

### A-1.2 ORIFICE FLOW (SECONDARY FLOW)

$$W = KYA\sqrt{2g_c\rho (P_u - P_d)} \tag{A-2}$$

The discharge coefficient K was defined by the equation

$$K = 0.5602 + 0.2721\beta - 0.7246\beta^2 + 0.8750\beta^3 - \left[0.00743 \, \log D_{PIPE} - 0.002231\right] \left(\frac{\beta - 0.25}{0.35}\right)$$

$$\tag{A-3}$$

The expansion factor Y was defined by the equation for $1 > P_d/P_u \geq 0.63$

$$Y = 0.3245\left(\frac{P_d}{P_u}\right) + 0.6755 + \left[0.033 - 0.055\beta\right]\left[2.703 - \left(1 - \frac{P_d}{P_u}\right)\right] \tag{A-4}$$

for $0.63 > P_d/P_u > 0$

$$Y = 0.394\left(\frac{P_d}{P_u}\right) - 0.623 + \left[0.102 - 0.17\beta\right]\left[1 - 1.053\left(\frac{P_d}{P_u}\right)\right] \tag{A-5}$$

where $\beta$ = $D_{ORIFICE}/D_{PIPE}$.

## A-2.0 ALTITUDE

Altitudes were calculated from the tables of the 1962 *Standard Atmosphere*, with

$$\text{Altitude} = f\ (P_s,\ \text{Type of Day}) \tag{A-6}$$

## A-3.0 VELOCITY AND MACH NUMBER

The flight velocity and Mach number were calculated by using an isentropic relationship with $P_T$, $P_S$, and $T_T$ and with a ram recovery of unity.

$$V = \left\{ 2\,C_p\,T_t \left[ 1 - \left( \frac{P_s}{P_t} \right)^\gamma \right] \right\}^{\frac{1}{2}} \tag{A-7}$$

$$a = \sqrt{\gamma g_c R\,T_s} \tag{A-8}$$

$$M = \frac{V}{a} \tag{A-9}$$

where $T_S$ = $f(T_T, P_T, P_S)$.

## A-4.0 FREEJET VOLUMETRIC AIRFLOW RATE

The freejet volumetric airflow rate was calculated from the relationship

$$Q = A \cdot V \tag{A-10}$$

where V = $f\ (T_T, P_S, P_T)$.

## A-5.0 LIQUID WATER CONTENT

The airstream liquid water content was calculated from the relationship

$$LWC = \frac{W_{H_2O}}{Q \cdot K} \tag{A-11}$$

where Q = $(A, T_T, P_S, P_T)$ and K = $6.241 \times 10^{-5}$.

78

# APPENDIX B
# CURVE-FITTING AND STATISTICAL PARAMETERS

## B-1.0 CURVE FITTING

The method of least squares is used to express one variable in terms of another even though the variables are not necessarily analytical functions of each other. In reporting the data of this report, two types of least-squares linear regressions were used.

### B-1.1 LINEAR FIT

For the data typical of Fig. B-1, a simple linear regression was used; the constants of the correlating equation are determined as
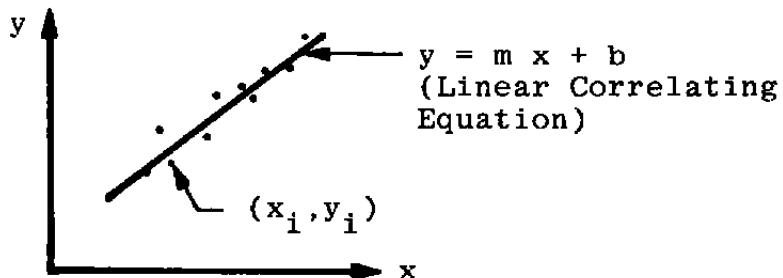


Figure B-1. Typical Linear Regression

$$m = \frac{\sum\limits_{i=1}^{n} x_i y_i - \dfrac{\sum\limits_{i=1}^{n} x_i \sum\limits_{i=1}^{n} y_i}{n}}{\sum\limits_{i=1}^{n} x_i^2 - \dfrac{\left(\sum\limits_{i=1}^{n} x_i\right)^2}{n}} \qquad (B-1)$$

$$b = \left[ \frac{\sum\limits_{i=1}^{n} y_i}{n} - m \frac{\sum\limits_{i=1}^{n} x_i}{n} \right] \qquad (B-2)$$

The coefficient of determination is calculated to determine the quality of the fit achieved by the regression. It is given by

$$r^2 = \frac{\left[\sum\limits_{i=1}^{n} x_i \, y_i - \dfrac{\sum\limits_{i=1}^{n} x_i \sum\limits_{i=1}^{n} y_i}{n}\right]^2}{\left[\sum\limits_{i=1}^{n} x_i^2 - \dfrac{\left(\sum\limits_{i=1}^{n} x_i\right)^2}{n}\right]\left[\sum\limits_{i=1}^{n} y_i - \dfrac{\left(\sum\limits_{i=1}^{n} y_i\right)^2}{n}\right]}$$ (B-3)

Values of $r^2$ close to unity indicate a better fit than values close to zero.

## B-1.2 POWER CURVE FIT
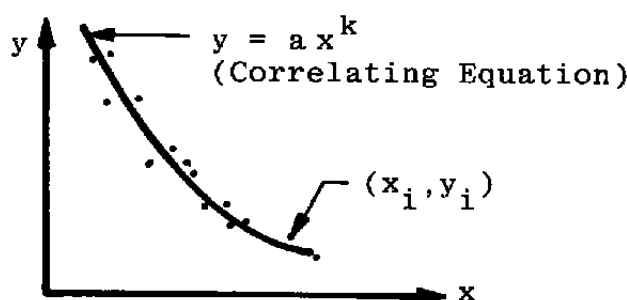


Figure B-2. Power Curve Fit

To use the least-squares method to fit the data of Fig. B-2 to the nonlinear power equation, it was necessary to reduce the problem to a linear one by first taking the logarithms, getting

$$\ell n \; y \; = \; \ell n \; a + k \; \ell n \; x$$ (B-4)

Equation (B-4) is linear in the parameters, $A' = \ell n \; a$ and $K = k$. Hence, a linear regression was applied to determine the regression coefficient of the power curve fit. The coefficients are determined from

$$k = \frac{\sum\limits_{i=1}^{n} (\ell n \; x_i)(\ell n \; y_i) - \dfrac{\sum\limits_{i=1}^{n} (\ell n \; x_i) \sum\limits_{i=1}^{n} (\ell n \; y_i)}{n}}{\sum\limits_{i=1}^{n} (\ell n \; x_i)^2 - \dfrac{\left(\sum\limits_{i=1}^{n} \ell n \; x_i\right)^2}{n}}$$ (B-5)

$$a = \exp \left\{ \sum_{i=1}^{n} \frac{(\ell n \ y_i)}{n} - k \sum_{i=1}^{n} \frac{(\ell n \ x_i)}{n} \right\} \qquad \text{(B-6)}$$

The coefficient of determination is given by

$$r^2 = \frac{\left[ \sum_{i=1}^{n} (\ell n \ x_i)(\ell n \ y_i) - \frac{\left( \sum_{i=1}^{n} \ell n \ x_i \right)\left( \sum_{i=1}^{n} \ell n \ y_i \right)}{n} \right]^2}{\left[ \sum_{i=1}^{n} (\ell n \ x_i)^2 - \frac{\left( \sum_{i=1}^{n} \ell n \ x_i \right)^2}{n} \right]\left[ \sum_{i=1}^{n} (\ell n \ y_i)^2 - \frac{\left( \sum_{i=1}^{n} \ell n \ y_i \right)^2}{n} \right]} \qquad \text{(B-7)}$$

## B-2.0 STATISTICAL PARAMETERS

Let a set of data $(x_i, y_i)$ be represented by the least-squares curve fit equation

$$y = f(x) \qquad \text{(B-8)}$$

Also, let

$$\delta_i = f(x_i) - y_i \qquad \text{(B-9)}$$

be the deviations of the computed values from the observed values. Then the mean deviation, or error, is defined as

$$\bar{\delta} = \frac{\sum_{i=1}^{n} \delta_i}{n} \qquad \text{(B-10)}$$

and the standard deviation of the errors is given by

$$S_\delta = \sqrt{\frac{\sum_{i=1}^{n} \delta_i^2 - \frac{\left( \sum_{i=1}^{n} \delta_i \right)^2}{n}}{n-1}} \qquad \text{(B-11)}$$

81

# APPENDIX C
# CALCULATED DATA RATE FOR BACKSCATTERING
# PARTICULE SIZING SYSTEM

The average liquid water content of an icing cloud is defined as

$$\overline{LWC} = \frac{\pi}{6} \rho \overline{d^3} \cdot N \qquad \text{(C-1)}$$

where $\overline{d}$ is some average droplet size of the icing cloud. If the cloud has a monodisperse droplet distribution as reported for the backscattering particle-sizing system described in Section 3.2.4, then the average LWC becomes the actual LWC. Hence, to determine the droplet number density for a monodisperse distribution,

$$N = LWC \left( \frac{6}{\pi} \frac{1}{\rho \overline{d^3}} \right) \qquad \text{(C-2)}$$

For the histogram of Fig. 39, $d = 8.5 \ \mu m$, input LWC = 0.35 g/m³; hence,

$$N = 0.35 \left( \frac{6}{\pi} \times \frac{10^6}{(8.5)^3} \right) = 1,088 \text{ particles/cc}$$

The probe volume, $V_s$, is 0.5 mm³ and the firing frequency of the laser, q is $10^3$/sec (Section 2.2.4). The data rate of the backscattering particle-sizing system becomes

$$\dot{N} = V_s \, \omega \, N \qquad \text{(C-3)}$$

or for the histogram of Fig. 39

$$\dot{N} = (0.5 \times 10^{-3}) \, (10^3) \, (1,088)$$

$$= 504.4 \text{ particles/sec}$$

*

# NOMENCLATURE

| A | Area, $ft^2$, in.$^2$ |
|---|---|
| a | Constant or sonic velocity, ft/sec |
| B | Bin number for FOS |
| b | Constant |
| $C_d$, $C_v$ | Flow coefficients |
| $C_p$ | Specific heat at constant pressure, $ft^2/sec^2 {}^\circ R$ |
| $C_t$ | Thermal expansion coefficient, in./in. |
| $D_o$ | Orifice diameter, ft, in. |
| $D_p$ | Pipe diameter, ft, in. |
| $\bar{d}$ | Mean effective droplet diameter, $\mu m$ |
| $d_a$ | Actual diameter, $\mu m$ |
| $d_{gm}$ | Mass geometric mean diameter, $\mu m$ |
| $d_i$ | ith droplet diameter, $\mu m$ |
| $d_m$ | Measured diameter, $\mu m$ |
| $f_i$ | Frequency of observation of diameter $d_i$ |
| FOS | Fiber-Optics System |
| $g_c$ | Dimensional constant, lbm-ft/lbf-$sec^2$ |
| K | Discharge coefficient |
| k | Constant or conversion factor |
| LWC | Liquid water content, $gm/m^3$ |
| M | Geometric mean droplet size based on count, $\mu m$, or Mach number |
| m | Constant |
| N | Droplet number density, particles/cc |

| $\overset{\bullet}{N}$ | Data rate, samples/sec |
|---|---|
| n | Sum of all droplets or sum of all data points |
| $n_i$ | Number of droplets contained in the ith line |
| $P_a$ | Atomizing air pressure, psfa |
| $P_d$ | Static pressure downstream of orifice, psfa |
| $P_s$ | Static pressure, psfa |
| $P_t$ | Total pressure, psfa |
| $P_u$ | Static pressure upstream of orifice, psfa |
| $P_w$ | Spray nozzle water pressure, psfa |
| Q | Volumetric flow rate, $ft^3$/sec |
| $r^2$ | Coefficient of determination |
| $S_g$ | Geometric standard deviation |
| $S_\delta$ | Standard deviation of measurement errors |
| $T_t$ | Total temperature, °R |
| V | Air velocity, ft/sec |
| W | Primary-airflow rate, lbm/sec |
| $W_{H_2O}$ | Spray nozzle water flow rate, lbm/sec |
| $\overset{\bullet}{w}_a$ | Mass flow rate of spray nozzle atomizing air, lbm/sec |
| $\overset{\bullet}{w}_w$ | Mass flow rate of spray nozzle water, lbm/sec |
| Y | Expansion factor |
| $\beta$ | $D_o/D_p$ |
| $\gamma$ | Ratio of specific heats |
| $\delta_i$ | ith deviation between the computed and observed values |
| $\varrho$ | Density, $lbm/ft^3$ |